

18 AE

THE PREDICTION OF HYDROFRACTURE PRESSURE AND K_0
DURING DRILLING

A Thesis

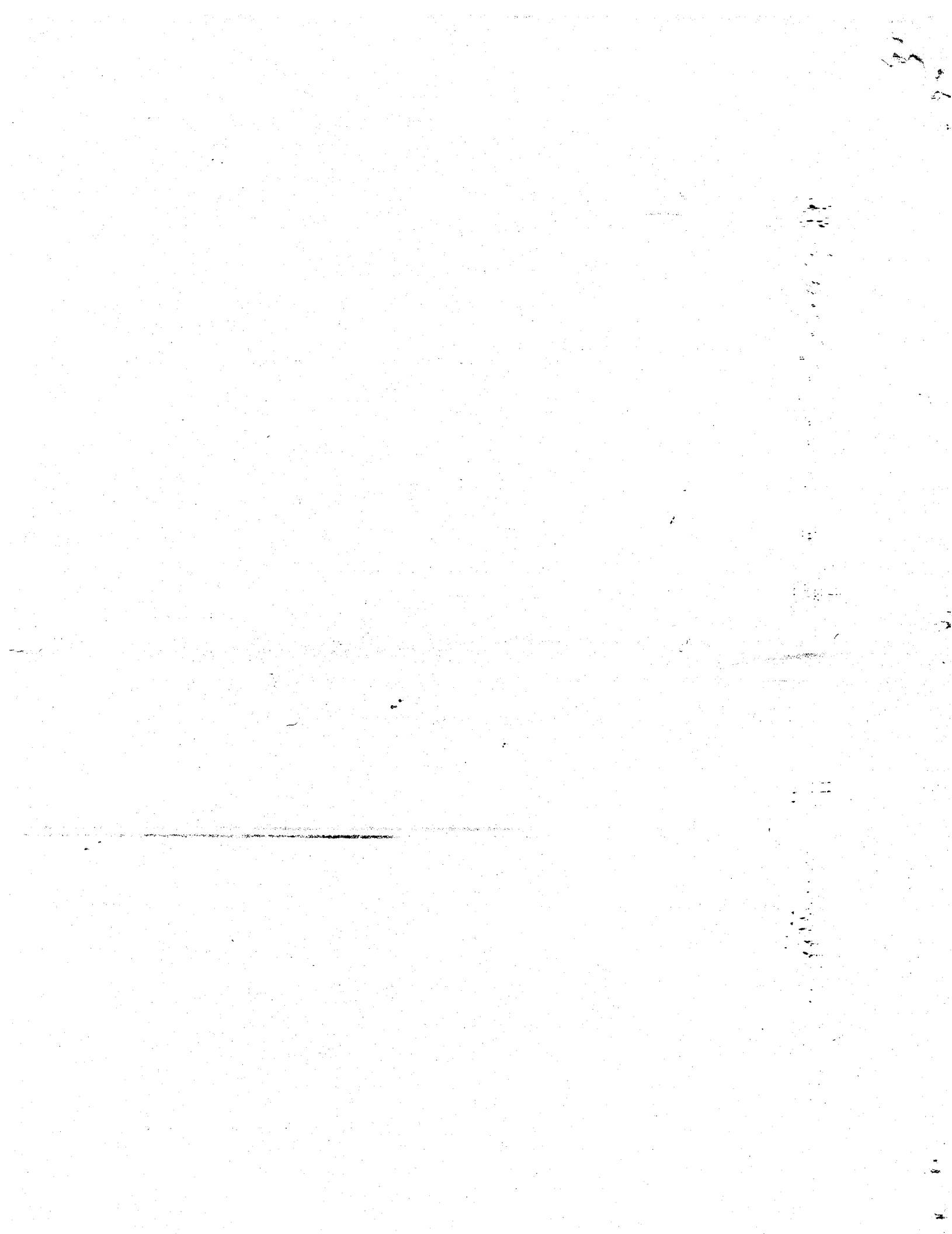
by

MICHAEL JOSEPH CALLANAN

Submitted to the Graduate College of
Texas A&M University
in partial fulfillment of the requirement for the degree of
MASTER OF SCIENCE

August 1980

Major Subject: Civil Engineering



ABSTRACT

The Prediction of Hydrofracture Pressure and K_0
During Drilling (August 1980)

Michael Joseph Callanan, B.S., Texas A&M University

Chairman of Advisory Committee: Dr. L. J. Thompson

Equations are derived describing borehole pressures responsible for the three cases of hydrofracture and the three cases of sloughing failure possible during drilling. Equilibrium and the Mohr-Coulomb failure criterion are used in the derivations. The material is assumed to be homogeneous, isotropic and under geostatic conditions with a nonpenetrating fluid filling the borehole. Hydrofracture pressure predictions using these equations correlate well with average field results.

One of the most influential material parameters which affects these equations is K_0 . No distinct relationships are found between K_0 and other material parameters through laboratory measurements of K_0 for nineteen soil samples. K_0 is highly dependent on material type and stress history. K_0 for loading is constant and ranged from 0.48 to 0.71 for the materials tested. To predict K_0 during drilling, results of previous laboratory measurements of K_0 must be catalogued for the material being drilled. It must also be assumed that the material is normally consolidated which yields a minimum predicted value for hydrofracture pressure.

Two complete sets of measurements of horizontal stresses with induced pore pressures show the effective stress concept to be erroneous for predicting total stresses in a porous medium with high pore pressures. The matrix stress concept which utilizes equilibrium is shown to be more logical and accurate when the area of water, A_w is taken to be 0.71.

ACKNOWLEDGMENTS

Sincere gratitude is expressed to Dr. Louis J. Thompson who served as chairman of the author's Graduate Advisory Committee and director of the research program. His guidance in the preparation of this thesis was greatly appreciated.

Special thanks are extended to Advisory Committee member Drs. Howard L. Furr and Mary E. Gbur for their comments and suggestions during the preparation of the manuscript.

The author also wishes to thank Dr. David Yankelevsky for his assistance and suggestions throughout the research.

Gratitude is expressed to the United States Geological Survey for sponsoring this research under Contract No. 14-08-001-17289; Mr. John B. Gregory, Research Program Manager, Branch of Marine Oil and Gas Operations and Dr. William E. Sweet, Technical Monitor.

Finally, special appreciation is given to Mrs. Joy Taylor for typing the manuscript and to the author's wife, Sherry, for her patience and encouragement throughout the study.

TABLE OF CONTENTS

CHAPTER	PAGE
I. INTRODUCTION	1
Statement of the Problem	1
Objective	3
II. THE SIGNIFICANCE OF THE HYDROFRACTURE PROCESS	4
Applications of Intentional Hydrofracture	4
Dangers of Unintentional Hydrofracture During Drilling	5
III. THEORETICAL CONSIDERATIONS OF HYDROFRACTURE	8
Importance of the Existing Stress Field in the Analysis of Fractures in the Earth	8
Vertical Stress Determination	13
Effective Stress and Matrix Stress in a Porous Medium	14
Literature Review of Hydrofracture Pressure Theories	18
IV. HYDROFRACTURE PRESSURE BASED ON EQUILIBRIUM AND THE MOHR-COULOMB FAILURE CRITERION	28
Method of Analysis	28
Formulation of Equations Describing Failure Around a Borehole	35
Analysis of the Resulting Equations	42
V. LATERAL EARTH PRESSURE COEFFICIENT AT REST, K_0	47
Importance of K_0 in Predicting Hydrofracture Pressure	47

TABLE OF CONTENTS (CONTINUED)

CHAPTER		PAGE
	Devices for Measuring K_0 in the Laboratory . . .	48
	Results of Past Laboratory Measurements of K_0 . . .	53
VI.	EXPERIMENTAL PROGRAM	64
	Scope of the Experimentation	64
	Description of Testing Apparatus	65
	Preparation and Placement of the Samples	74
	Sequence of Testing Procedure to Determine K_0	76
	Procedure for Measuring A_w	77
VII.	PRESENTATION AND DISCUSSION OF RESULTS	79
	Description of Soil Samples Tested	79
	Typical Results	81
	Effects of Friction	90
	Relationships Involving K_0	97
	Results from the Measurement of A_w	104
	Application of Laboratory Derived K_0 Values to Drilling Operations	106
VIII.	CONCLUSIONS AND RECOMMENDATIONS	110
	APPENDIX I. - REFERENCES	113
	APPENDIX II. - NOTATION	119
	APPENDIX III. - CALCULATIONS CORRECTING FOR SIDEWALL FRICTION	124
	APPENDIX IV. - TABLES OF RESULTS FOR K_0 MEASUREMENT TESTS	128

TABLE OF CONTENTS (CONTINUED)

CHAPTER	PAGE
APPENDIX V. - RESULTS FROM TOTAL HORIZONTAL STRESS	
MEASUREMENTS WITH PORE PRESSURES INDUCED	151
VITA - - - - -	156

LIST OF TABLES

TABLE	PAGE
1. Six Cases of Failure Around a Borehole	33
2. Results from Derivations of Equations Describing Six Cases of Failure Around a Borehole	39
3. Expressions for Limiting Borehole Pressures	41
4. Summary of Published K_0 Values Obtained in the Laboratory for Normally Consolidated Soils	55
5. Description of Samples Used in Testing	82
6. Experimental K_0 Values for Loading	86
7. Experimental Results for Sample No. K-1	129
8. Experimental Results for Sample No. K-2	130
9. Experimental Results for Sample No. K-3	131
10. Experimental Results for Sample No. K-4	133
11. Experimental Results for Sample No. K-5	134
12. Experimental Results for Sample No. KS-1	135
13. Experimental Results for Sample No. KS-2	136
14. Experimental Results for Sample No. KS-3	137
15. Experimental Results for Sample No. KS-4	138
16. Experimental Results for Sample No. S-1	139
17. Experimental Results for Sample No. S-2	140
18. Experimental Results for Sample No. I	141
19. Experimental Results for Sample No. B	143
20. Experimental Results for Sample No. OS-1	144
21. Experimental Results for Sample No. OS-2	145
22. Experimental Results for Sample No. OS-3	147

LIST OF TABLES (CONTINUED)

TABLE		PAGE
23.	Experimental Results for Sample No. MC-I-U	148
24.	Experimental Results for Sample No. MC-I-R	149
25.	Experimental Results for Sample No. MC-II-U	150
26.	Horizontal Stress Measurements with Pore Pressures Induced for Sample No. OS-3	152
27.	Horizontal Stress Measurements with Pore Pressures Induced for Samples No. MC-II-U	154

LIST OF FIGURES

FIGURE		PAGE
1.	Orientation of Fractures with Respect to Principal Stress Directions	9
2.	Geostatic Principal Stress Configurations in the Earth with Corresponding Fracture Orientations	11
3.	Non-Geostatic Principal Stress Configurations in the Earth with Corresponding Fracture Orientations	12
4.	Representation of Grain-to-Grain Contact Areas in a Soil Layer	16
5.	Typical Bottom Hole Pressure Curve During a Well Fracturing Operation	21
6.	Failure Zone Surrounding a Borehole	29
7.	Assumed Orientation of the Matrix Principal Stresses Around the Borehole	31
8.	Predicted Hydrofracture Profiles Showing a Change in Failure Modes	43
9.	A Comparison of Predicted Hydrofracture Profiles with Field Results	44
10.	Predicted Hydrofracture Profiles Illustrating the Significance of K_0	46
11.	Schematic of Null-Type Consolidometer Used by Several Investigators to Measure K_0	50
12.	Typical Plot of Horizontal Stress Versus Vertical Stress for Loading and Unloading	54

LIST OF FIGURES (CONTINUED)

FIGURE		PAGE
13.	Previous Data Compared to Relationships Between K_o and ϕ	60
14.	Previous Data Showing No Unique Relationship Between K_o and PI	61
15.	Typical Relationships Between K_o and OCR as Observed by Schmidt (48)	63
16.	Schematic of High Pressure Consolidation System	66
17.	Cross-sectional Schematic View of High Pressure Stainless Steel Consolidometer	67
18.	Low Pressure Calibration Curve for Determining Horizontal Stresses in Soil	70
19.	High Pressure Calibration Curve for Determining Horizontal Stresses in Soil	71
20.	Specialty Designed High Pressure Electrical Connector	73
21.	Gradation of Sands Used in Samples	80
22.	Stresses Measured After Consolidation of Sample K-4	84
23.	Stresses Measured After Consolidation of Sample K-3, Three Loading Cycles	87
24.	Compressibility of Sample K-4	88
25.	Compressibility of Sample K-3	89
26.	Correction of Vertical Effective Stress for Measured Friction, Sample K-4	91

LIST OF FIGURES (CONTINUED)

FIGURE		PAGE
27.	Slip Cones Expected Due to Frictional Stresses Across Top and Bottom Boundaries	93
28.	Slip Cones Observed in Ottawa Sand Sample OS-3	94
29.	Comparison of Boundary Stresses Exerted by Tall and Short Samples	95
30.	Observed Relationship Between K_0 and Initial Sample Height for Kaolinite Samples	96
31.	Experimental Results Showing No Relationships Between K_0 and PI	98
32.	Effects of Percent Fines on K_0 for Kaolinite - Sand Mixtures	99
33.	Relationship Between K_0 and OCR for Sample K-4	100
34.	Relationship Between K_0 and OCR for Sample I	101
35.	Stresses Measured After Consolidation of Undisturbed and Remolded Marine Clay	103
36.	Typical Results of Total Horizontal Stress Measurement Test with Pore Pressures Induced	105
37.	Variation of Water Area with Porosity as Measured for Two Soils	107
38.	Approximation of Vertical Load Throughout a Consolidating Sample in a Floating Ring Consolidometer	126
39.	Approximation of Vertical Load Throughout a Rebounding Sample in a Floating Ring Consolidometer	127

CHAPTER I

INTRODUCTION

Statement of the Problem

When the fluid pressure in a borehole becomes sufficiently high, cracks in the surrounding formation are initiated and propagate away from the well in nearly vertical or horizontal planes. This process is known as hydraulic fracturing or hydrofracturing.

Intrusive dike and sill formations are large scale examples of natural fracturing processes very similar to the man-made process of hydrofracturing (4, 24, 39). It is believed that pressurized magma chambers existing somewhere beneath the surface of the earth act as sources for the intrusions. The fluid pressure of the molten rock in such a chamber increases the stresses normal to the chamber causing the surrounding rock to strain to the point of fracturing. Once the fractures are initiated the overpressured magma infiltrates the cracks causing a wedging effect which helps to further extend the fractures. The magma later cools and solidifies forming a solid intrusive sheet. Similar occurrences also appear in the formation of salt diapirisms and mud volcanoes around the world (18, 26, 40).

In the formation of intrusive structures the resulting fractures represent a releasing of energy from the overpressured source. The maximum pressure which could build up in the source would be the pressure

The style and format of this thesis follows that used by the Journal of the Geotechnical Engineering Division, American Society of Civil Engineers.

necessary to initiate fractures in the surrounding formations. Once the cracks begin to propagate and enough energy has been released, thereby sufficiently reducing the pressure in the source, the crack propagation will cease.

Knowledge of the magnitudes of fluid pressures necessary for hydrofracture is important in operations where such fractures are intentionally induced, such as in oil and gas well stimulation, squeeze cementing, waste disposal, and tectonic stress determination. The hydrofracture pressure is also important during drilling operations for oil and gas exploration. In this instance unintentional hydrofracturing can cause a loss of circulation and a drop in the borehole fluid level resulting in a blowout from a previously encountered layer. Therefore, it is desirable to prevent such a dangerous and economic disaster by maintaining the borehole fluid pressure at a level which prevents fracture of the surrounding material. To do this, the pressure necessary to fracture the formation must be constantly known or predicted for the entire uncased length of the borehole. Although theories concerning hydrofracture pressure are numerous, accurate predictions of hydrofracture pressures during drilling are rare because of a lack of knowledge of the material parameters as well as a lack of recognition of the basic mechanisms involved.

The hydrofracture pressure is a function of the compressibility and strength parameters of the formation, and the initial total stress state in the formation. The total stresses depend upon the formation pore pressure, gravity, and tectonic activity. In the absence of tectonic activity the horizontal stresses in the earth are equal in every

direction, which describes the geostatic condition. For the geostatic condition, the ratio of horizontal to vertical stresses in the soil matrix is the lateral earth pressure coefficient at rest, which is referred to as K_0 .

Perhaps the most influential factor in the mechanics of hydrofracture is this ratio, K_0 , yet very little is known about its magnitude at great depths. Because of the variability of K_0 in the earth, some way of determining this value for the surrounding material during continuous drilling is needed.

Objective

The goals of this research are as follows:

1. A theory for hydrofracture pressure prediction will be derived based on mechanics involved which may not have been considered by previous authors.

2. Laboratory tests will be used to analyze the behavior of K_0 for various materials under conditions which may exist in the earth. This is done in an attempt to find a relationship between K_0 and material parameters which will enable the estimation of K_0 from information obtained from cuttings during the drilling process.

The completion of these two goals will aid in the estimation of the localized stress state under geostatic conditions and facilitate a continuous prediction of the hydrofracture pressure.

CHAPTER II

THE SIGNIFICANCE OF THE HYDROFRACTURE PROCESS

Applications of Intentional Hydrofracture

Intentional hydrofracturing was first applied to squeeze cementing operations prior to the 1940's. Squeeze cementing refers to an operation whereby drill stem casings are rigidly cemented to the wall of the borehole by pumping cement or grout under high pressure through perforations in the casing. This process can hydrofracture the surrounding formation allowing grout to infiltrate the cracks which adds to the rigidity of the casings (58). This same principle is used in prestressed rock and soil anchor installations.

Hydrofracturing is used extensively in stimulation efforts in which the fractures are induced to increase downhole permeability to enhance the flow of petroleum or natural gas. Clark (12) first introduced this concept to the petroleum industry in 1949. Recently, "massive hydraulic fractures" have been accomplished extending as far as 3500 ft (1067 m) radially from the well (43). Presently the success of massive hydraulic fracturing is relatively unpredictable because of a general lack of understanding of the fundamental mechanics involved.

Hydrofracturing is sometimes used to decrease the flow of water through or underneath earth dams. This is accomplished by drilling a series of holes along the dam and then injecting each hole with grout until hydrofracture occurs. The objective is to form a continuous "curtain" of fractures along the dam filled with impermeable grout which intersects the channels of flow through the dam (50).

Low cost, high volume void spaces created by massive hydraulic fracturing have been used as industrial waste disposal reservoirs. This application has gained wide acceptance and has even been considered by the Atomic Energy Commission as a means of disposing of radioactive materials (23, 44).

Hydrofracturing has also been used as a means of determining in situ stresses at great depths (19, 21, 24, 29, 45, 46). It is assumed that the fractured formation is elastic within the range of stresses used. The basic idea, then, is to determine the principal stresses by entering the known pressure necessary to initiate fractures and Poisson's ratio into equations of equilibrium for elastic materials. By reversing this basic idea, the hydrofracture pressure could be predicted if the state of stress of the formation were known or could be predicted (45).

Dangers of Unintentional Hydrofracture During Drilling

An accidental hydrofracture during drilling causes a loss of the drilling fluid to the fracture. Fluid circulation ceases and the height of the column of mud in the hole drops, consequently lowering the downhole pressure. The fluid pressure necessary to propagate one of these cracks is usually much less than the pressure needed to initiate it, and therefore the fracture will continue to extend until the fluid pressure acting at the leading edge of the crack is below the pressure necessary for propagation. The fluid pressure at the leading edge of the crack decreases not only because of the decrease in downhole pressure but also because of friction encountered by the fluid along the sides of the crack (24).

As the cracks propagate, the fluid level continues to lower, and drilling crews continue to pump more and more drilling mud into the hole. In addition, they pump a variety of additives into the hole in an attempt to impede the openings of the cracks. Such an occurrence of hydrofracture is often unsignalled and may catch a drilling crew by total surprise.

If no zones of abnormal pore pressures (i.e. pressures in excess of hydrostatic pressure) have been encountered in the well prior to hydrofracture, the fluid level in the hole would eventually approach the natural water level after circulation loss. However, it is obvious that if abnormally pressured zones were penetrated, the decrease in fluid pressure in the well would allow a releasing of energy from the overpressured formation possibly resulting in a catastrophic blowout.

Not so obvious is the fact that a blowout could still occur in the absence of any abnormal pore pressures. This could happen if a porous sand layer containing pore water saturated with gas in solution was previously intersected by the well. When hydrofracture occurs and the fluid pressure in the well drops, the gas may be allowed to pop out of solution in the form of gas bubbles. The gas bubbles may be so abundant as to decrease the unit weight of the fluid in the well enough that it cannot even accommodate hydrostatic pressure. An ensuing blowout is then highly possible. According to Dave Powley of Amoco Research Laboratories (42), this is a relatively common occurrence in offshore drilling operations. In most cases, however, closure of blowout preventers keeps the well under control until a special crew can be mobilized and enough heavy mud is mixed to circulate into the well and

again establish the proper pressure gradient.

In order to decrease the possibilities of unintentional hydrofracture, the pressure needed to hydrofracture the well must be accurately predicted during drilling. If it is predicted that a particular segment of the well is weak and highly susceptible to hydrofracture, then casings can be set and drilling can proceed safely.

CHAPTER III

THEORETICAL CONSIDERATIONS OF HYDROFRACTURE

Importance of the Existing Stress Field in the Analysis of Fractures
in the Earth

It is the existing stress field in a formation which most affects the behavior of soil or rock during natural fracturing and hydrofracturing processes. Assuming the formation to be homogeneous and isotropic, the orientation of fractures is dependent upon the direction and relative magnitudes of the three principal stresses in the earth's crust.

Hydrofractures are usually considered to be extension fractures (24) which are the result of extension strain. Such fractures are oriented in planes perpendicular to the least principal stress. Because extension fractures are directly dependent upon strains, a constitutive relationship describing the stress-strain characteristics of the material is needed to predict borehole pressures responsible for the development of these fractures. Unfortunately stress-strain relationships are not available for soil and rock during drilling.

Hydrofractures may also be the result of shear failure. In this case the fractures are oriented as shown in Fig. 1 with respect to the principal stresses. Shear failure can be described by using a failure criterion written only in terms of stresses, thereby avoiding the need for stress-strain relationships.

The relative magnitudes and directions of the principal stresses in the earth's crust depend not only upon the material but also on the

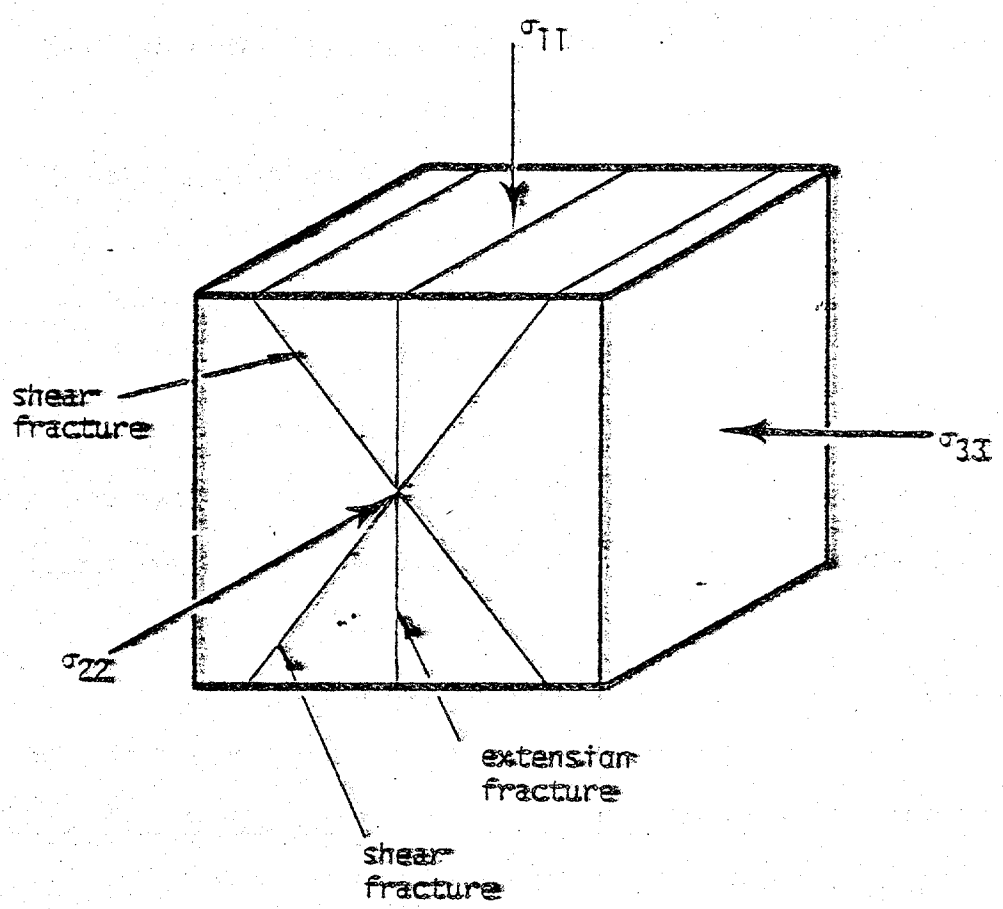


Fig. I - Orientation of Fractures with Respect to Principal Stress Directions

prevailing geologic conditions. Tectonic activity can be responsible for altering these stresses, as can erosion and deposition. Nevertheless, the three principal stresses in the earth's crust are usually assumed to occur in horizontal and vertical directions. Assuming horizontal and vertical orientation, eight different combinations of the relative magnitudes and directions of the principal stresses exist. Three of these combinations, shown in Fig. 2, apply to geostatic conditions where both horizontal principal stresses are equal. In the other five combinations, shown in Fig. 3, the two horizontal principal stresses are not equal, due to tectonic activities. Note that the major principal stress, σ_{11} , can be either horizontal or vertical. Also shown in Figs. 2 and 3 are the corresponding orientations of extension and shear fractures which would develop under failure conditions.

In each case there must be extension strain in the direction of the minor principal stress and contraction strains in the direction of the major principal stress sufficient to cause failure. Failure can be defined in many ways. Often failure is assumed to occur when strains continue without an increase in stresses. Others assume failure occurs with a complete loss of cohesion. The failure criterion does not consider whether extension cracks or shear planes develop first.

In order to predict formation behavior during drilling or during hydrofracturing processes, the existing or predrilled stress field must be known or predicted. Several field methods have been tried for measuring in situ stresses in the earth, yet most of these methods measure only single components of the stress field, or a stress ratio (25). Because of the time involved and difficulty with which these

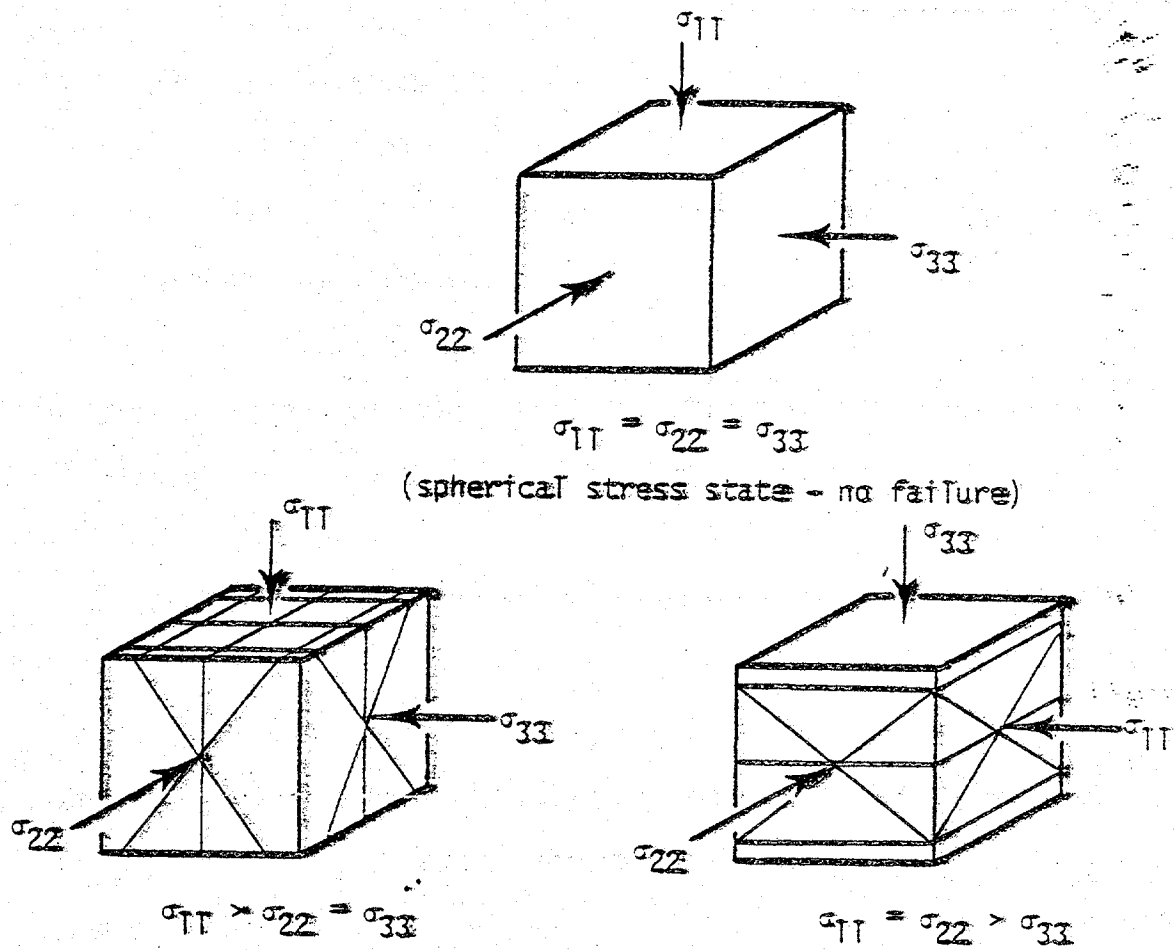


Fig. 2 - Geostatic Principal Stress Configurations in the Earth with Corresponding Fracture Orientations

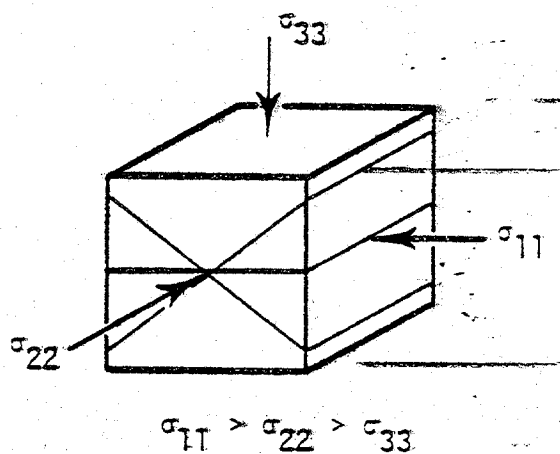
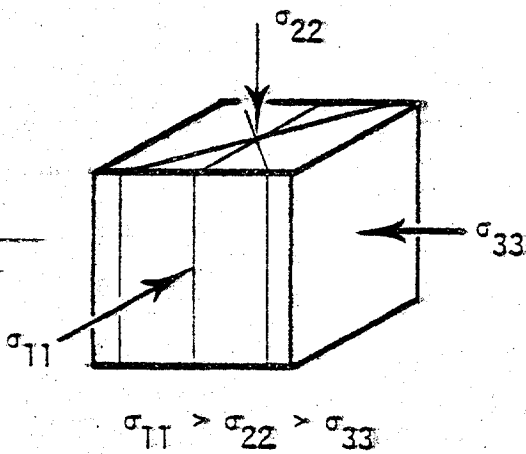
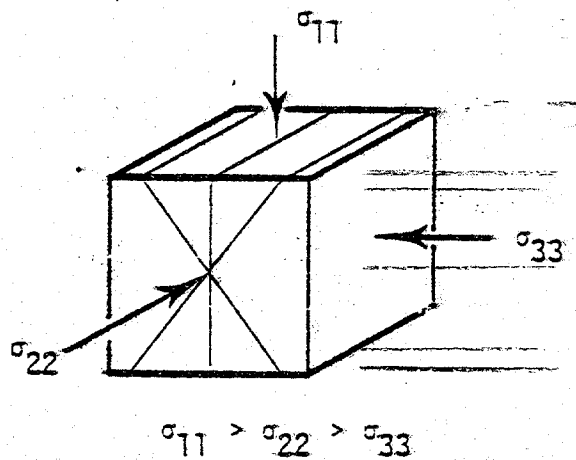
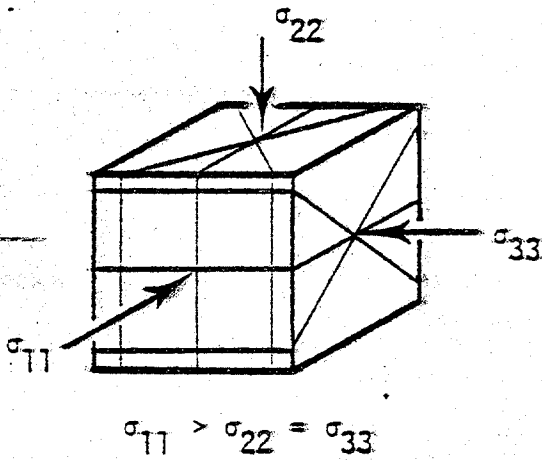
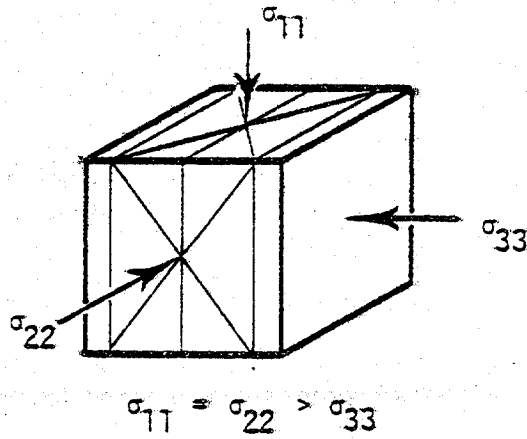


Fig. 3 - Non-Geostatic Principal Stress Configurations in the Earth with Corresponding Fracture Orientations

measurements are made, direct methods could not be useful in predicting hydrofracture pressures during drilling. In order to maintain continuous drilling with a minimum threat of unintentional hydrofracture, an indirect method of constantly predicting the localized stress field is needed.

Vertical Stress Determination

If the state of stress is geostatic, the total vertical stress on a material in the earth is equal to the pressure induced by the weight of the column of overburden above the material. Therefore, the vertical stress can be calculated by integrating the unit weight of the material with respect to depth as follows:

$$\sigma_v = \int_0^z \gamma_T dz \quad \text{----- (1)}$$

where: σ_v = total vertical stress (overburden stress)
 γ_T = total unit weight of material
 z = depth, vertical coordinate

This calculation is routinely performed during drilling using material unit weights obtained from density logs. Density log data is gathered using formation density tools designed to measure formation densities in situ (60).

The overburden stress gradient is usually about 1 psi/ft (22.6 kN/m²/m) of depth, and many times in approximating the overburden stress a gradient of 1 psi/ft (22.6 kN/m²/m) is assumed constant, which corresponds to a constant material unit weight. This assumption, however, can result

in significant error, because in many cases the overburden stress gradient is found to be substantially variable with depth. Eaton (15) cites gradients around 0.8 psi/ft (18.1 kN/m²/m) near the mudline and increasing to slightly more than 1.0 psi/ft (22.6 kN/m²/m) at depths approaching 10,000 ft (3048 m).

Effective Stress and Matrix Stress in a Porous Medium

Soils and rocks at great depth are two phase materials consisting of solid particles and fluid which fills the pore spaces between the solids. Because of this the total stress in any direction is a combination of the stress transmitted by the solid particles and the stress due to pore pressure. In describing soil and rock stresses in the earth the "effective stress" concept has become the most widely used. Effective stress was defined by Terzaghi (55) as the total stress minus the pore pressure, and is written as:

$$\sigma = \bar{\sigma} + u \quad \dots \dots \dots (2)$$

where $\bar{\sigma}$ = effective stress

σ = total stress

u = pore pressure

Gersevanov called this effective stress the "fictitious stress" and expressed the above equation in tensor notation as reported by Scheidegger (47).

Because the effective stress concept does not consider the areas over which the individual stresses act, this concept does not satisfy

equilibrium. For this reason Skempton (52) and later Thompson (56) used equilibrium to relate stresses in a porous medium which yields the following expression:

$$\sigma A_T = \sigma_S A_S + u A_W \quad \dots \dots \dots (3)$$

where σ_S = stress acting across grain-to-grain contacts (intergranular stress)

A_T = total area of any surface through soil

A_S = grain-to-grain contact area

A_W = area on which pore pressure acts = $A_T - A_S$

This equation can also be written as:

$$\sigma = \frac{A_S}{A_T} \sigma_S + \frac{A_W}{A_T} u \quad \dots \dots \dots (4)$$

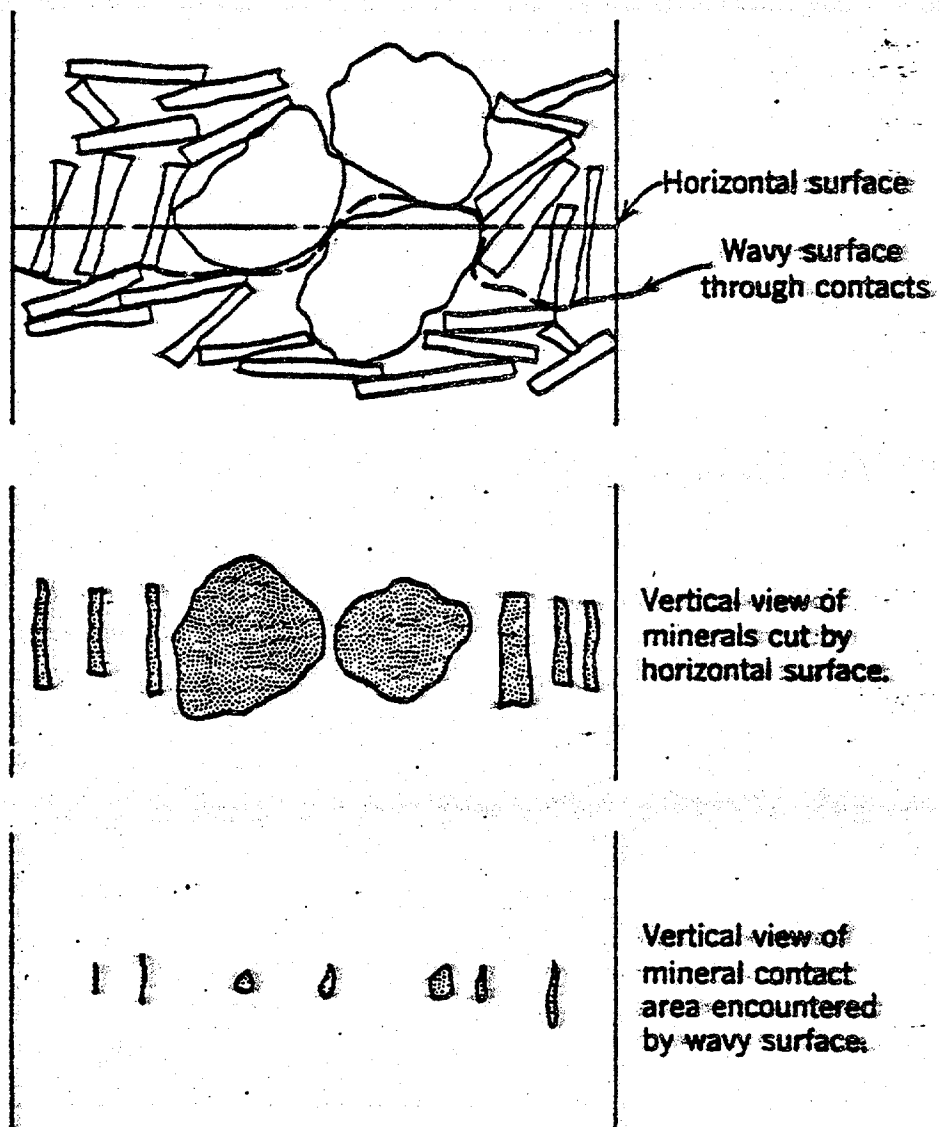
By letting $A_T = 1$, A_W becomes a dimensionless ratio for water area per unit area of soil (water and mineral)

and $\sigma^t = A_S \sigma_S$ = matrix stress = force transmitted by the soil matrix per unit area of soil

yields $\sigma = \sigma^t + A_W u \quad \dots \dots \dots (5)$

Note that if $A_W = 1$ then the matrix stress in Eq. 5 is identical to the effective stress in Eq. 2.

It is generally accepted that some finite area across grain-to-grain contacts exists as shown in Fig. 4 (31). Laboratory measurements have shown this area to range from zero to 1.3 (7, 32, 52, 54). Because of the difficulties and uncertainties involved in making these measurements, there is disagreement as to the magnitude and importance of the



Taken from Lambe and Whitman (31)

Fig. 4 - Representation of Grain-to-Grain Contact Areas in a Soil Layer

contact areas.

In considering total horizontal stresses, the effective stress concept implies that:

$$\sigma_{Hr} = \bar{\sigma}_{Hr} + u \quad \dots \dots \dots (6)$$

where σ_{Hr} = total horizontal stress
 $\bar{\sigma}_{Hr}$ = effective horizontal stress

If the pore pressure is changed and the effective horizontal stress held constant then

$$\Delta\sigma_{Hr} = \Delta u \quad \dots \dots \dots (7)$$

However, according to the matrix stress concept derived from equilibrium:

$$\sigma_{Hr} = \sigma_{Hr}^m + A_w u \quad \dots \dots \dots (8)$$

where σ_{Hr}^m = matrix horizontal stress

Changing the pore pressure while holding σ_{Hr}^m constant should yield:

$$\Delta\sigma_{Hr} = A_w (\Delta u) \quad \dots \dots \dots (9)$$

Eq. 7 would match Eq. 9 only if $A_w = 1$ implying that $A_s = 0$. A relatively simple procedure of changing the pore pressure and measuring the change in total stress gives one way in which the water area can be determined. This procedure was performed in the experimental portion of

this research and will be discussed in Chs. VI and VII.

Literature Review of Hydrofracture Pressure Theories

In scaled down laboratory fracturing tests Haimson (21) illustrated the complexity of the hydrofracture process by showing that the crack initiation pressure is influenced by the combined effects of pressurization rate, hole geometry, depth of penetration of the fracturing fluid, tensile strength of the formation, and most importantly the state of stress surrounding the hole.

In 1957 Hubbert and Willis (24) used elasticity theory to describe the state of stress around a borehole prior to hydraulic fracturing. They then ignore this analysis to formulate a simple equation for predicting fracture propagation pressure using a nonpenetrating fracture fluid. They point out that since rocks are usually intersected by one or more systems of joints and bedding laminations, the tensile strength of a formation is essentially zero. In the formulation, effective stresses are used and it is assumed that the major principal effective stress is in the vertical direction. The least effective stress is horizontal and is said to be proportional to the vertical effective stress. Therefore,

$$\bar{\sigma}_h = K_0 \bar{\sigma}_v \quad \dots \dots \dots (10)$$

where K_0 = ratio of horizontal to vertical effective stress
 $\bar{\sigma}_v$ = effective vertical stress

Hubbert and Willis (24) make the gross assumption that for normally consolidated formations the value of K_0 ranges from one-third to one-half.

As a failure criterion it is assumed that fracture extension occurs when the injection pressure exceeds the formation pore pressure plus the least principal effective stress. Therefore,

$$P_p = u + \bar{\sigma}_H = u + K_\alpha (\sigma_{V_1} - u) \quad \dots \dots \dots (11)$$

where P_p = borehole pressure necessary to propagate fracture.

In 1967 Matthews and Kelly (34) attempted to improve the estimation of K_α by replacing it with an empirically derived term referred to as the matrix stress coefficient, k_f . This coefficient is generated from values of fracture initiation pressure already obtained for a particular geographic region. They found that k_f decreases with depth for the Texas and Louisiana Gulf Coast areas. A substantial amount of fracture data from an area must already exist in order to determine the relationship of k_f with depth.

In 1969 Eaton (14) replaced K_α of the formation with the veteran expression from elastic theory relating K_α to Poisson's ratio, ν , assuming zero strain in the horizontal direction. This expression is

$$K_\alpha = \frac{\nu}{1-\nu} \quad \dots \dots \dots (12)$$

This introduces the assumption that the fractured formation acts as an elastic material which, for large strains, could prove to be inaccurate.

Schrefdeger (46), in 1962, used a two-dimensional approach in an attempt to determine the stress state in the earth's crust from hydraulic fracturing data. He used elasticity theory to describe the stress

state existing at the borehole wall for the fracture condition. The following equations result for penetrating and non-penetrating fluids:

(i) Penetrating fluid

$$P_i \geq 1/2 (3\sigma_{33} - \sigma_{22}) \dots \dots \dots (13)$$

(ii) Non-penetrating fluid

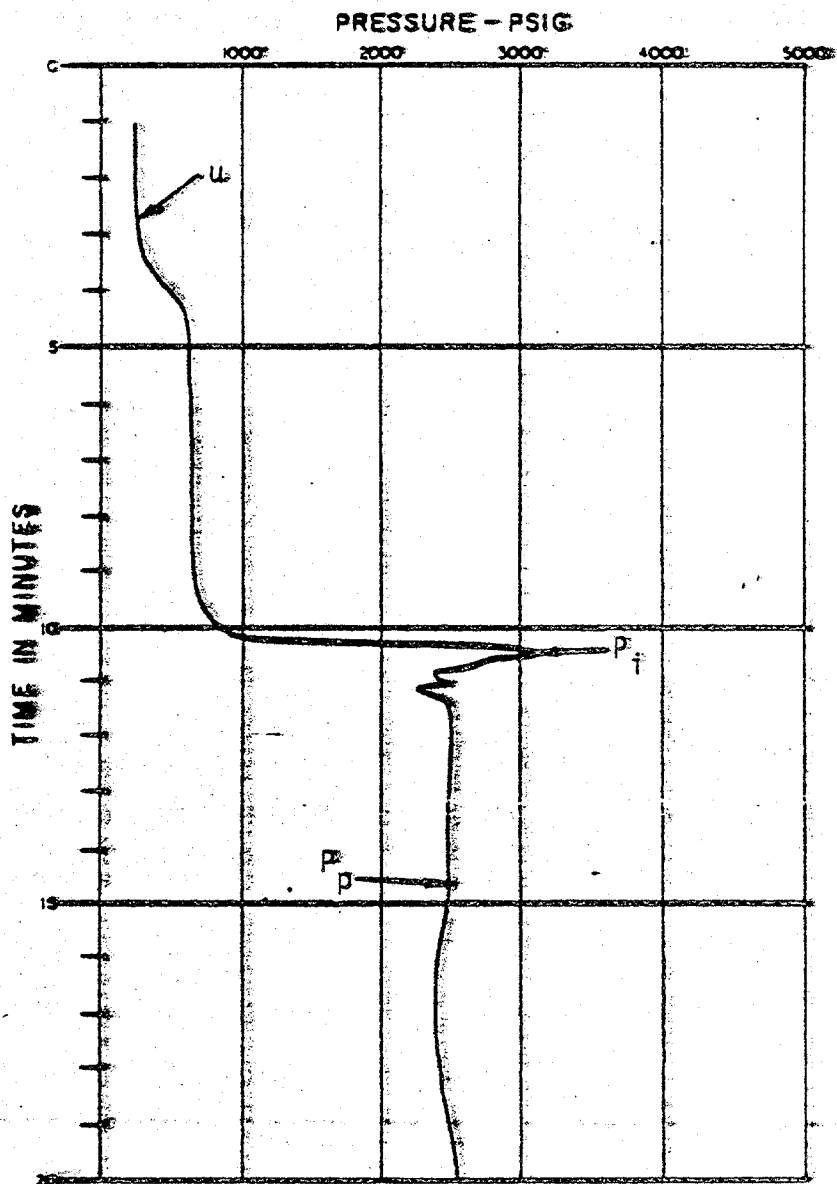
$$P_i \geq 3\sigma_{33} - \sigma_{22} - u \dots \dots \dots (14)$$

where P_i = injection pressure necessary to initiate fracture
 σ_{22} = intermediate total principal stress
 σ_{33} = minor total principal stress

In both cases, σ_{22} and σ_{33} are assumed to be in the horizontal direction. The inequality signs are used here to take into account possible tensile strength of the formation.

Typically the crack propagation pressure is less than the crack initiation pressure. A typical bottom-hole pressure curve illustrating the difference between the propagation pressure and initiation pressure is shown in Fig. 5 (46). If it is assumed that the propagation pressure is equal to the least principal stress, then from Eq. 14 it can be shown that the crack initiation pressure is greater than the propagation pressure if,

$$\sigma_{33} > \frac{\sigma_{22} + u}{2} \dots \dots \dots (15)$$



u = Formation pore pressure

P_f = Crack initiation pressure

P_p = Crack propagation pressure

Taken from Scheidegger (46)

Fig. 5 - Typical Bottom Hole Pressure Curve During a Well Fracturing Operation

During the same year Morgenstern (37) published a paper in which he postulates that the hydrofracture process is, in general, a shear failure. He uses the Mohr-Coulomb failure criterion and the effective stress principle but ignores equilibrium in deriving an equation for fracture initiation pressure. Assuming that the major principal stress is in the vertical direction, he expressed the Mohr-Coulomb failure criterion in terms of effective stresses in the usual following manner for active failure where the horizontal strains must be extension and the vertical strains must be contraction:

$$\frac{\bar{\sigma}_v + \bar{\sigma}_h}{2} \sin \phi = \frac{\bar{\sigma}_v - \bar{\sigma}_h}{2} - c \cos \phi \quad \dots \dots \dots (16)$$

where ϕ = angle of internal friction

c = cohesion

Taking the usual definition of K_0 for the earth stresses at rest, Morgenstern (37) assumed the horizontal effective stress to be:

$$\bar{\sigma}_h = K_0 \bar{\sigma}_v = K_0 (\sigma_v - u) \quad \dots \dots \dots (17)$$

which requires the horizontal strains to be zero. This is inconsistent with the assumed strain conditions of failure.

For the fracture condition the principal effective stresses in terms of the fracture initiation pressure, P_i , are:

$$\bar{\sigma}_{vf} = \bar{\sigma}_v - P_i + u \quad \dots \dots \dots (18)$$

$$\bar{\sigma}_{hf} = \bar{\sigma}_h - P_i + u \dots \dots \dots (19)$$

where $\bar{\sigma}_{vf}$ and $\bar{\sigma}_{hf}$ = vertical and horizontal effective stresses at failure

Substituting Eqs. 18 and 19 into Eq. 16 yields the following equation for fracture initiation pressure:

$$P_i = \bar{\sigma}_v \left(\frac{1+K_0}{2} \right) - \frac{\bar{\sigma}_v (1-K_0)}{2 \sin \phi} + c \cot \phi + u \dots \dots \dots (20)$$

In 1967 Haimson and Fairhurst (20) considered hydrofracture as a two-dimensional problem and assumed the formation to be elastic, porous, isotropic and homogeneous. Haimson and Fairhurst used one set of equations to describe two horizontal principal stresses before the borehole is introduced. They then used elasticity to derive another set defining stresses induced by drilling the borehole. Since fluid flow through porous media is analogous to heat conduction through solids, the authors made use of the theory of thermoelasticity to derive a third set of equations defining the changes in stress due to a penetrating fluid. Using the principle of superposition these three sets of equations were combined to yield the following expressions for the stresses at the wall of the borehole:

$$\sigma_r = -P_w \dots \dots \dots (21)$$

$$\sigma_\theta = \bar{\sigma}_{33} + \bar{\sigma}_{22} - 2(\bar{\sigma}_{33} - \bar{\sigma}_{22}) \cos 2\theta - u + (P_w - u) -$$

$$- \alpha (P_w - u) \frac{1-2\nu}{1-\nu} \dots \dots \dots (22)$$

$$\tau_{r\theta} = 0 \dots \dots \dots (23)$$

where

σ_r = total radial stress

σ_θ = total tangential stress

$\tau_{r\theta}$ = total shear stress

P_w = borehole pressure

$\bar{\sigma}_{22}$ = intermediate (major horizontal) effective principal stress

$\bar{\sigma}_{33}$ = minor (horizontal) effective principal stress

θ = polar coordinate around borehole

$\alpha = (1 - C_r/C_b)$

C_r = rock matrix compressibility

C_b = rock bulk compressibility

Eq. 22 is the only one considered, since it is only in this equation that the effective stress can become tensile. Hence, to maximize σ_θ , for $\theta = 0, \pi$:

$$\sigma_\theta = 3\bar{\sigma}_{33} - \bar{\sigma}_{22} - u + (P_w - u) - \alpha (P_w - u) \frac{1-2\nu}{1-\nu} \dots \dots \dots (24)$$

or, in terms of the effective tangential stress:

$$\bar{\sigma}_\theta = 3\bar{\sigma}_{33} - \bar{\sigma}_{22} + (P_w - u)(2 - \alpha \frac{1-2\nu}{1-\nu}) \dots \dots \dots (25)$$

Fracture is induced if $\bar{\sigma}_\theta$ equals or exceeds the tensile strength of the formation, σ_t , therefore:

$$P_i = \frac{\sigma_t - 3\bar{\sigma}_{33} + \bar{\sigma}_{22}}{2 - \frac{1-2\nu}{1-\nu}} + u \dots \dots \dots (26)$$

A similar analysis of the stresses around a borehole using the theory of thermoelasticity was made by Geertsma (17). He points out that linear elasticity is assumed because of a lack of knowledge of the rheological properties of sedimentary rocks. He identifies a need to replace simple elastic constants in the formulation with more realistic parameters.

In 1972 Bjerrum et al. (9) analyzed the problem of hydrofracture during in situ permeability testing. In the tests a piezometer is forced into the soil which induces additional stresses in the surrounding soil. Bjerrum accounts for this by introducing two factors, β_1 and β_2 , which depend primarily on the soil compressibility. The horizontal effective stresses around the piezometer are given as:

$$\bar{\sigma}_r = (1 + \beta_1) K_{\alpha} \bar{\sigma}_v \dots \dots \dots (27)$$

$$\bar{\sigma}_\theta = (1 - \beta_2) K_{\alpha} \bar{\sigma}_v \dots \dots \dots (28)$$

where $\bar{\sigma}_r$ = effective radial stress
 $\bar{\sigma}_\theta$ = effective tangential stress

If the fluid pressure is too great during an in situ permeability test, the soil may either fracture or be pushed away from around the piezometer (this is termed "blow-off") and then fracture. The author uses elasticity relationships to formulate equations defining the fluid pressures needed for two separate conditions of fracturing. The first

equation describing the conditions for vertical fracturing prior to blow-off is:

$$P_i = \left(\frac{1}{v} - 1\right) \{\sigma_t + (1 - \beta_2) K_0 \bar{\sigma}_v\} + u \quad \dots \dots \dots (29)$$

The second equation for vertical fracturing after blow-off occurs is:

$$P_i = (1-v) \{\sigma_t + (2 - \beta_2 + \beta_1) K_0 \bar{\sigma}_v\} + u \quad \dots \dots \dots (30)$$

Later in 1972 MacPherson and Berry (33) made a qualitative study of hydrofracture pressure gradients and empirically determined that fracture pressure appears to be related to the sand-shale ratio of the formation. They found that for decreasing percentages of sand in the formation the fracture pressures increase. It was also found that the fracture gradients in abnormally pressured formations differ very little from those in normally pressured formations.

Anderson, Ingram and Zanier (5) continued with an analysis of the effects of shaliness on fracture pressure in a paper published in 1973. These authors derived an expression for fracture initiation pressure very similar to that of Haimson et al. (20) involving Poisson's ratio and porosity of the formation. They concluded that fracture pressure is sensitive to shaliness because Poisson's ratio is sensitive to shaliness.

In 1977, Althaus (3) made an empirical analysis of several sets of hydrofracture data and concluded that the fracture gradient is independent of the formation pore pressure gradient and dependent only

upon the earth's stress field. He also wrote that the fracture pressure is the highest pore pressure which a formation may possess. When the pore pressure exceeds the fracture pressure, the earth fractures and energy is released to permeable beds.

CHAPTER IV

HYDROFRACTURE PRESSURE BASED ON EQUILIBRIUM
AND THE MOHR-COULOMB FAILURE CRITERIONMethod of Analysis

Failure occurs if the fluid pressure in the borehole allows the stresses in the formation surrounding the hole to meet a failure criterion. If the pressure in the borehole is too high then a loading mode of failure, or passive failure, corresponding to hydrofracture occurs. If the pressure in the borehole is too low then an unloading mode of failure, or active failure, occurs which is referred to as a spalling or sloughing failure. There is a range of borehole pressures between these two modes of failure for which borehole stability is maintained. If the borehole pressure during drilling were first decreased enough to allow a sloughing failure to occur, and then increased again, hydrofracture would likely occur at a much lower pressure than before. This is because a fractured zone would develop around the borehole during the sloughing failure. Therefore it is important to know the borehole pressures responsible for both modes of failure.

For either mode there is a failure zone or plastic zone, of radius b , developed around the borehole as illustrated in Fig. 6. Beyond the plastic zone is an elastic zone in which the radial and tangential stresses approach the predrilled stresses when the radius, r , approaches infinity.

Jumikis (28) used equilibrium and the Mohr-Coulomb failure

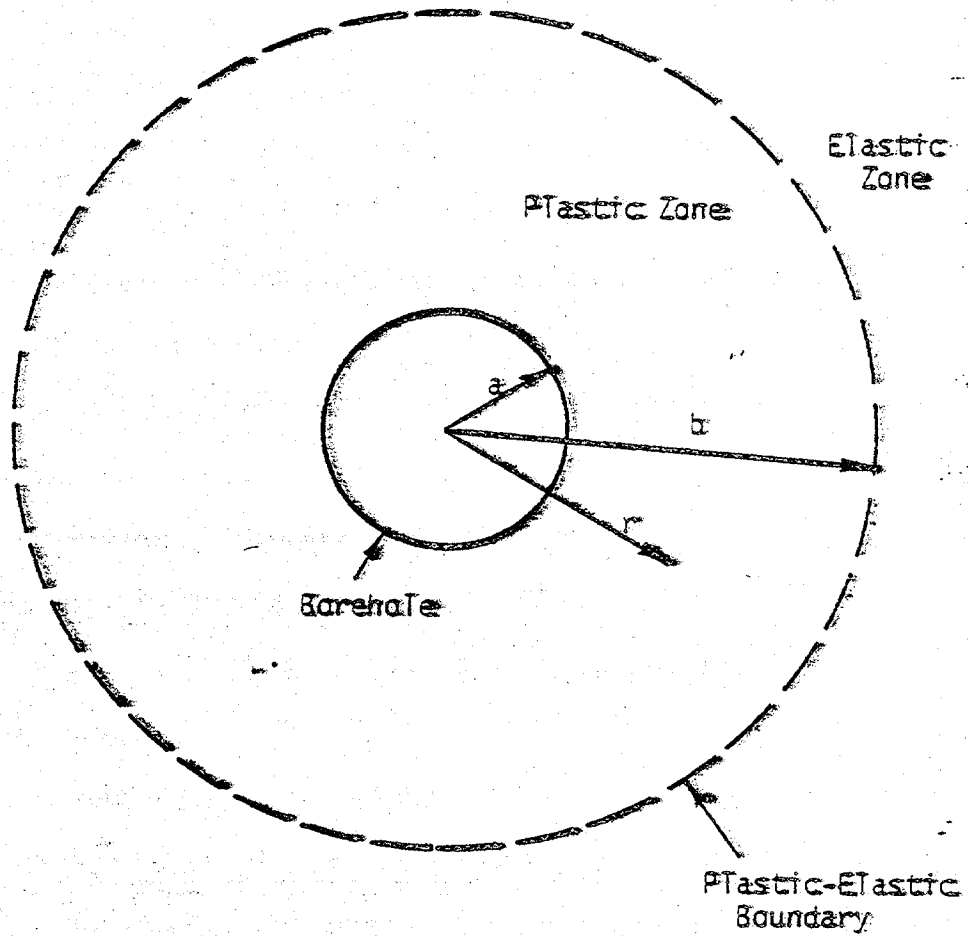


Fig. 6 - Failure Zone Surrounding a Borehole

criterion to describe stresses in the plastic and elastic zones around a circular shaft in rock. Westergaard (61) used the same approach to study instability around a borehole in an attempt to determine what conditions are necessary to keep an open borehole stable due to arching of the surrounding material. Both authors assumed a spherical predrilled stress state (i.e. $K_0 = 1$).

The same basic approach can also be used to analyze both the problem of the loading mode of failure (hydrofracture) and the unloading mode of failure (sloughing) during drilling.

To simplify this analysis, the formation is considered to be homogeneous and isotropic and the fluid in the borehole is assumed to be nonpenetrating. The analysis employs an axisymmetric approach in which the borehole is the axis of symmetry. All equations involving stress are written in terms of matrix stress, σ' , as defined in Ch. III. The matrix principal stresses are assumed to occur in the vertical, radial and tangential directions around the borehole as shown in Fig. 7. The vertical matrix stress, σ'_z , is assumed to be constant for a given depth and computed as follows:

$$\sigma'_z = \gamma_T Z - A_W u \dots \dots \dots (31)$$

Geostatic conditions are assumed which implies that the predrilled horizontal matrix stresses are equal in every direction to $K_0 \sigma'_z$. By definition of principal stresses, no shear stresses exist on planes perpendicular to the directions of σ'_r , σ'_θ and σ'_z . Given these directions for the matrix principal stresses, six combinations of the major,

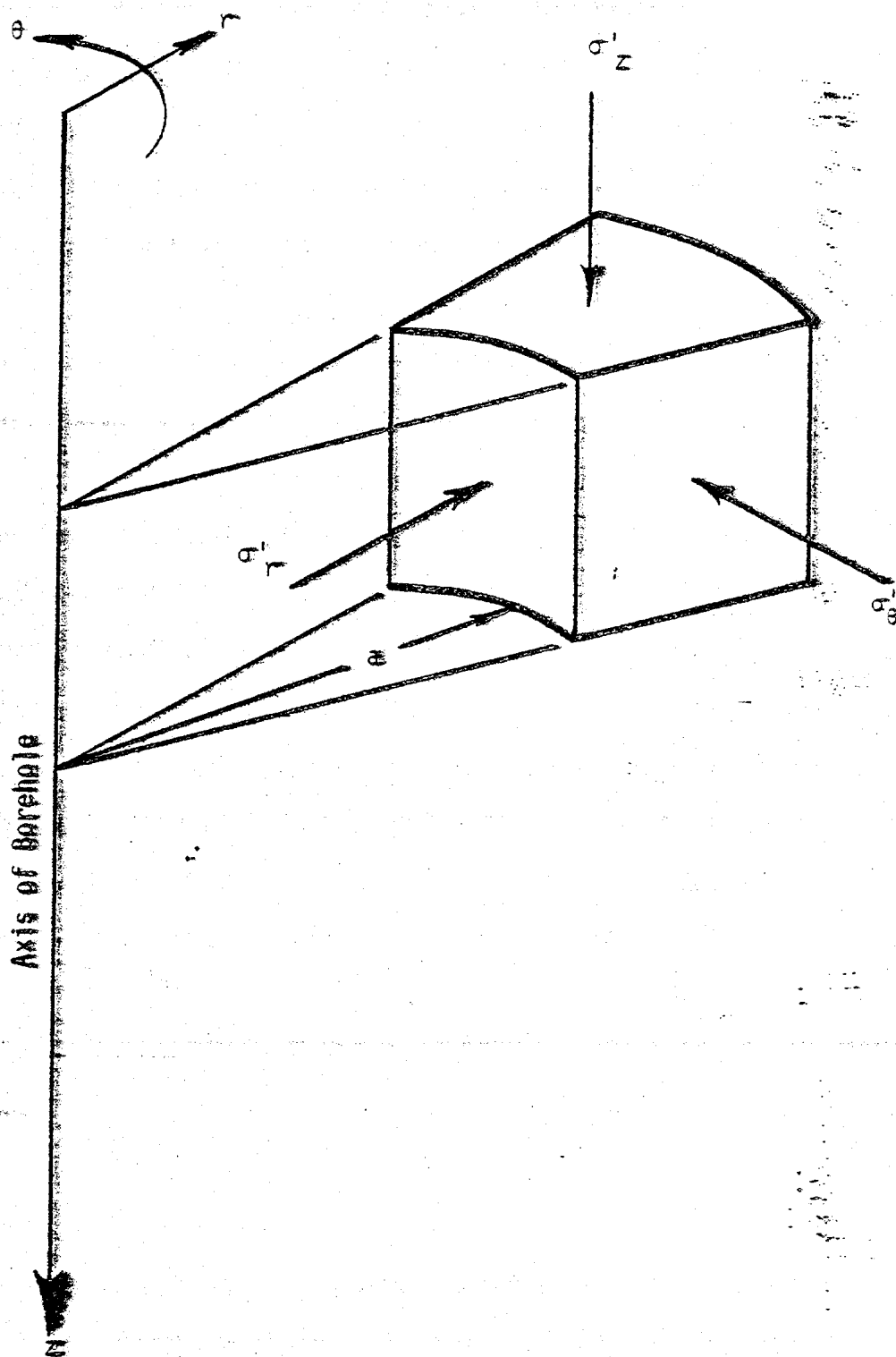


Fig. 7 - Assumed Orientation of the Matrix Principal Stresses Around the Borehole

intermediate and minor matrix principal stresses are possible as listed in Table 1. The magnitude of the borehole pressure determines which of these stress states exist around the borehole. For cases II and V the vertical stress is always the major principal stress, which implies that K_0 must be less than unity. Similarly, in cases III and VI the vertical stress is always the minor principal stress, which implies that K_0 must be greater than unity.

Depending upon the stress state, different forms of the failure criterion must be considered in conjunction with equilibrium. As shown by Tschebotarioff (59), the general form of the Mohr-Coulomb failure criterion can be written as:

$$\sigma_{11} - \lambda \sigma_{33} = \beta \quad \dots \dots \dots (32)$$

or in terms of matrix stresses,

$$\sigma'_{11} - \lambda \sigma'_{33} = \beta \quad \dots \dots \dots (33)$$

where σ'_{11} = major matrix principal stress

σ'_{33} = minor matrix principal stress

$$\lambda = \frac{1 + \sin \phi}{1 - \sin \phi} = \tan^2 \left(45 + \frac{\phi}{2} \right)$$

$$\beta = \frac{2c \cos \phi}{1 - \sin \phi} = 2c \tan \left(45 + \frac{\phi}{2} \right)$$

The failure criterion which applies to each of the six possible stress states around the borehole is listed in Table 1. Failure under these stress conditions results in hydrofracture for the first

TABLE 1 - Six Cases of Failure Around a Borehole

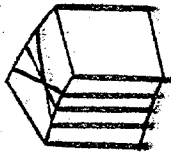
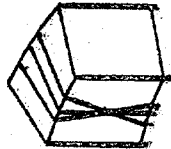
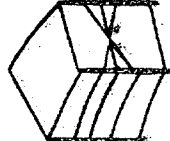
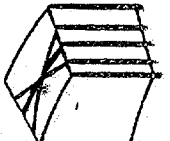
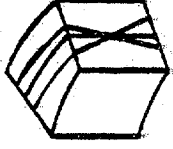
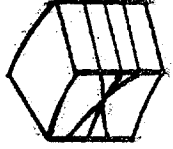
Case	σ_1	σ_2	σ_3	σ_1'	σ_2'	Failure Criterion	Type of Failure	Orientation of Failure Planes
I	σ_1	σ_2	σ_3	σ_1	σ_2	$\sigma_1 - \sigma_2 > \sigma_3$	hydrofracture	
II	σ_1	σ_2	σ_3	σ_1	σ_2	$\sigma_1 - \sigma_2 > \sigma_3$	hydrofracture, $K_0 < 1$	
III	σ_1	σ_2	σ_3	σ_1	σ_2	$\sigma_1 - \sigma_2 < \sigma_3$	hydrofracture, $K_0 > 1$	
IV	σ_1	σ_2	σ_3	σ_1	σ_2	$\sigma_1 - \sigma_2 > \sigma_3$	sloughing	

TABLE 1 - (Continued)

Case	σ'_r	σ'_θ	σ'_z	Failure Criterion	Type of Failure	Orientation of Failure Planes
V	σ'_{33}	σ'_{22}	σ'_{11}	$\sigma'_z - \lambda\sigma'_r \geq \beta$	sloughing, $K_0 < 1$	
VI	σ'_{22}	σ'_{11}	σ'_{33}	$\sigma'_\theta - \lambda\sigma'_z \geq \beta$	sloughing, $K_0 > 1$	

three cases and sloughing for the last three. The resulting orientations of the failure planes are also shown in Table 1. Horizontal fractures, as described by cases III and VI, only occur near the surface (24).

Formulation of Equations Describing Failure Around a Borehole

The equation of static equilibrium for the two-dimensional axisymmetric case, in terms of matrix stresses, is:

$$\frac{\partial \sigma_r^i}{\partial r} + \frac{\sigma_r^i - \sigma_\theta^i}{r} = 0 \quad \text{--- (34)}$$

where compression is positive. The following general solutions for radial and tangential stresses in the elastic zone, satisfying Eq. 34, is given by Timoshenko and Goodier (57) and is attributed to Lamé:

$$\sigma_{re}^i = B - \frac{D}{r^2} \quad \text{--- (35)}$$

$$\sigma_{\theta e}^i = B + \frac{D}{r^2} \quad \text{--- (36)}$$

where B and D are constants to be determined from boundary conditions.

The constant B is evaluated from the condition that σ_{re}^i and $\sigma_{\theta e}^i$ approach the predrilled horizontal matrix stress, $K \sigma_z^i$, as the radius, r , approaches infinity so that Eqs. 35 and 36 can be written as:

$$\sigma_{re}^i = K \sigma_z^i - \frac{D}{r^2} \quad \text{--- (37)}$$

$$\sigma'_{\theta e} = K_0 \sigma'_z + \frac{D}{r^2} \dots \dots \dots (38)$$

Since the failure criterion is not involved in Eqs. 37 and 38, these relationships are identical for all cases. However, the constant D will differ for each case.

For case I the matrix principal stress configuration dictates that the failure criterion be written as:

$$\sigma'_r - \lambda \sigma'_\theta = \beta \dots \dots \dots (39)$$

where $\sigma'_r = \sigma'_{11}$

$$\sigma'_\theta = \sigma'_{33}$$

For the plastic zone Eqs. 34 and 39 are combined yielding the following first order differential equation:

$$\frac{\partial \sigma'_r}{\partial r} + \frac{(\lambda-1)\sigma'_r}{\lambda r} = \frac{-\beta}{\lambda r} \dots \dots \dots (40)$$

This differential equation and its solution differ for each case, because the failure criteria differ for each case. The solution to Eq. 40 results in the following equations for the radial and tangential stresses in the plastic zone:

$$\sigma'_{rp} = Ar^{\left(\frac{1}{\lambda} - 1\right)} + \frac{\beta}{1-\lambda} \dots \dots \dots (41)$$

$$\sigma'_{\theta p} = \frac{\Gamma}{\lambda} A r^{\left(\frac{\Gamma}{\lambda} - 1\right)} + \frac{\beta}{\Gamma - \lambda} \quad \dots \dots \dots (42)$$

where A is a constant to be determined from boundary conditions.

The constants A and D are evaluated by equating plastic and elastic stresses at the plastic-elastic boundary in the following manner:

at $r=b$

$$\sigma'_{rp} = \sigma'_{re} \quad \dots \dots \dots (43)$$

$$\text{and} \quad \sigma'_{\theta p} = \sigma'_{\theta e} \quad \dots \dots \dots (44)$$

which results in two equations with two unknowns, A and D. For case I, the resulting expressions for A and D, in terms of b , are as follows:

$$A = 2 \left[\frac{K_0 \sigma'_z + \frac{\beta}{\lambda - \Gamma}}{\left(\Gamma + \frac{\Gamma}{\lambda}\right) b^{\left(\frac{\Gamma}{\lambda} - 1\right)}} \right] \quad \dots \dots \dots (45)$$

$$D = \left[\frac{\left(\frac{\Gamma}{\lambda} - 1\right) K_0 \sigma'_z - \frac{\beta}{\lambda}}{\Gamma + \frac{\Gamma}{\lambda}} \right] b^2 \quad \dots \dots \dots (46)$$

If the pressure in the borehole, P_{wb} , follows the matrix stress concept as follows:

$$P_{wb} = p + A_{wb} u \quad \dots \dots \dots (47)$$

where p = the portion of borehole pressure transmitted to the soil

matrix

then the radius of the plastic zone, b , is found by letting $\sigma'_{rp} = p$, for $r = a$, and then solving for b , yielding:

$$b = a \left[\frac{2 \left(\frac{K_0 \sigma'_z + \frac{\beta}{\lambda-1}}{1 + \frac{1}{\lambda}} \right)^{\frac{\beta}{1-\lambda}}}{p + \frac{\beta}{\lambda-1}} \right] \dots \dots \dots (48)$$

The limiting matrix failure pressure, p_f , for which failure begins at the wall of the borehole, is determined by letting $b = a$ in Eq. 48 and then solving for p . This yields:

$$p = p_f = \frac{2\lambda K_0 \sigma'_z + \beta}{1 + \lambda} \dots \dots \dots (49)$$

The same expression can be obtained by letting $p_f = \sigma'_{re}$ when σ'_{re} and $\sigma'_{\theta e}$ satisfy the failure criterion for $r = a$. The limiting borehole pressure, P_i , for which failure or fractures are initiated, is written as:

$$P_i = p_f + A_w u \dots \dots \dots (50)$$

This same derivation is made for each of the six cases listed in Table 1 (p. 33). The resulting expressions for σ'_{rp} , $\sigma'_{\theta p}$, A , D and b are summarized for all six cases in Table 2. The expressions for P_i are tabulated in Table 3 for all six cases.

TABLE 2 - Results from Derivations of Equations Describing Six Cases of Failure Around a Borehole

Case	σ'_{rp}	$\sigma'_{\theta p}$	A	B	b
I	$A r \left(\frac{\lambda}{\lambda-1} \right) + \frac{\beta}{\lambda-1}$	$\frac{1}{\lambda} A r \left(\frac{\lambda}{\lambda-1} \right) + \frac{\beta}{\lambda-1}$	$\left[\frac{K_0 \sigma'_z + \frac{\beta}{\lambda-1}}{\left(1 + \frac{\lambda}{\lambda-1} \right) b} \right] \left(\frac{\lambda}{\lambda-1} \right)$	$\left[\frac{\left(\frac{\lambda}{\lambda-1} \right) K_0 \sigma'_z + \frac{\beta}{\lambda-1}}{1 + \frac{\lambda}{\lambda-1}} \right] b^2$	$\frac{\left[\frac{K_0 \sigma'_z + \frac{\beta}{\lambda-1}}{1 + \frac{\lambda}{\lambda-1}} \right] \left(\frac{\lambda}{\lambda-1} \right)}{b + \frac{\beta}{\lambda-1}}$
II	$A r + \frac{\lambda}{\lambda} (\sigma'_z = \beta)$	$\frac{1}{\lambda} (\sigma'_z = \beta)$	$\left[\frac{\lambda K_0 (\sigma'_z + \beta)}{\lambda b} \right]$	$\left[\frac{\lambda}{(1 - \lambda K_0) \sigma'_z - \beta} \right] b^2$	$\frac{\left[\frac{\lambda K_0 (\sigma'_z + \beta)}{\lambda} \right] \left(\sigma'_z = \beta \right)}{b - \frac{\lambda}{\lambda} (\sigma'_z = \beta)}$
III	$\beta + \lambda \sigma'_z$	$\beta + \lambda \sigma'_z$	\times	θ	\times
IV	$A r (\lambda-1) - \frac{\beta}{\lambda-1}$	$\lambda A r (\lambda-1) - \frac{\beta}{\lambda-1}$	$\left[\frac{K_0 \sigma'_z + \frac{\beta}{\lambda-1}}{(1 + \lambda) b (\lambda-1)} \right]$	$\left[\frac{(\lambda-1) K_0 \sigma'_z + \beta}{1 + \lambda} \right] b^2$	$\frac{\left[\frac{K_0 \sigma'_z + \frac{\beta}{\lambda-1}}{1 + \lambda} \right] \left(\frac{\lambda-1}{\lambda-1} \right)}{b + \frac{\beta}{\lambda-1}}$

TABLE 2 - (Continued)

Case	σ_{rp}^i	$\sigma_{\theta p}^i$	A	D	b
V	$\frac{1}{\lambda} (\sigma_z^i - \beta)$	$\frac{1}{\lambda} (\sigma_z^i - \beta)$	X	0	X
VI	$A r + \beta + \lambda \sigma_z^i$	$\beta + \lambda \sigma_z^i$	$2 \left[\frac{(K_0 - \lambda) \sigma_z^i - \beta}{b} \right]$	$[\beta + (\lambda - K_0) \sigma_z^i] b^2$	$\frac{2a [(K_0 - \lambda) \sigma_z^i - \beta]}{(p - \beta - \lambda \sigma_z^i)}$

TABLE 3 - Expressions for Limiting Borehole Pressures

Case	Limiting Borehole Pressure, P_i
I	$\frac{2\lambda K_o \sigma'_Z + \beta}{1 + \lambda} + A_w u$
II	$\frac{(2\lambda K_o - 1)\sigma'_Z + \beta}{\lambda} + A_w u$
III	$K_o \sigma'_Z + A_w u$ if and only if: $\lambda \sigma'_Z + \beta = K_o \sigma'_Z$
IV	$\frac{2K_o \sigma'_Z - \beta}{1 + \lambda} + A_w u$
V	$K_o \sigma'_Z + A_w u$ if and only if: $\sigma'_Z - \beta = \lambda K_o \sigma'_Z$
VI	$(2K_o - \lambda)\sigma'_Z - \beta + A_w u$

Analysis of the Resulting Equations

The expressions for P_i are perhaps the most important expressions obtained from these derivations. This is because P_i dictates the borehole pressure which must be maintained during drilling to prevent an unintentional failure around the borehole. The material parameters K_0 , ϕ , c and γ_T determine P_i for each of the six cases. To prevent hydrofracture, the borehole pressure must be kept below the lowest value of P_i as computed from cases I, II and III. To prevent sloughing, the borehole pressure must remain above the highest value of P_i as computed from cases IV, V and VI.

Even if the material parameters are constant with depth, different failure modes may occur first at different depths. This is illustrated in Fig. 8 where a profile of P_i for hydrofracture is drawn. Note that P_i is least for case I to a depth of 240 ft (73.2 m) indicating that the mode of failure described by case I occurs first to a depth of 240 ft (73.2 m). However, P_i is least for case II below 240 ft (73.2 m), indicating that the mode of failure described by case II occurs first below a depth of 240 ft (73.2 m). Case III is not applicable here since K_0 is less than unity. Different sloughing failure modes are also possible at different depths.

Actual field fracturing data taken from several sources shows the average hydrofracture gradient to be about 0.82 psi/ft (18.1 kN/m²/m) as shown in Fig. 9 (5, 16, 53). Also shown in this figure are two hydrofracture profiles computed using the equations in Table 3. These profiles show the variation of P_i with depth assuming typical material parameters which are constant with depth.

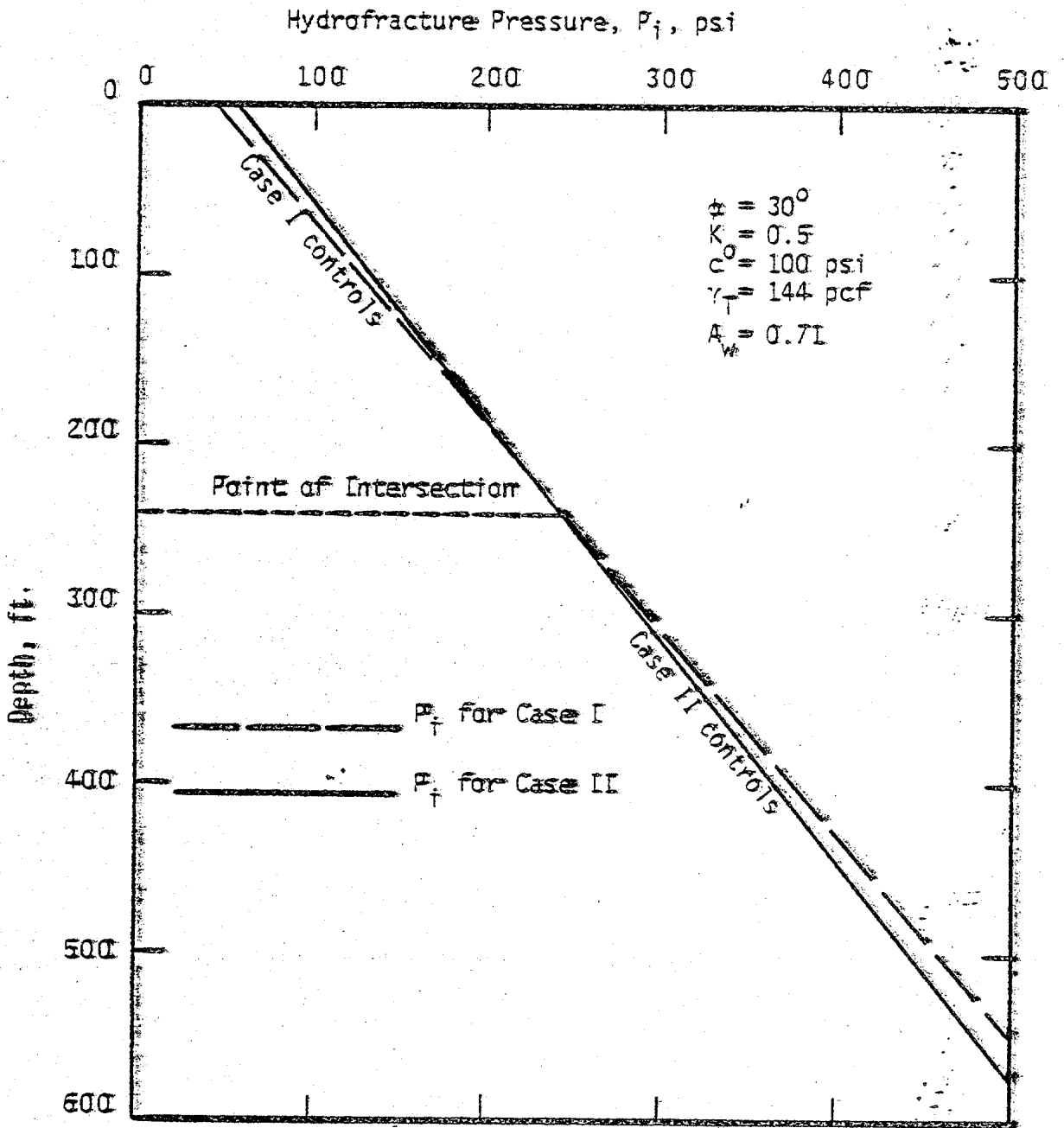


Fig. 8 - Predicted Hydrofracture Profiles Showing a Change in Failure Modes

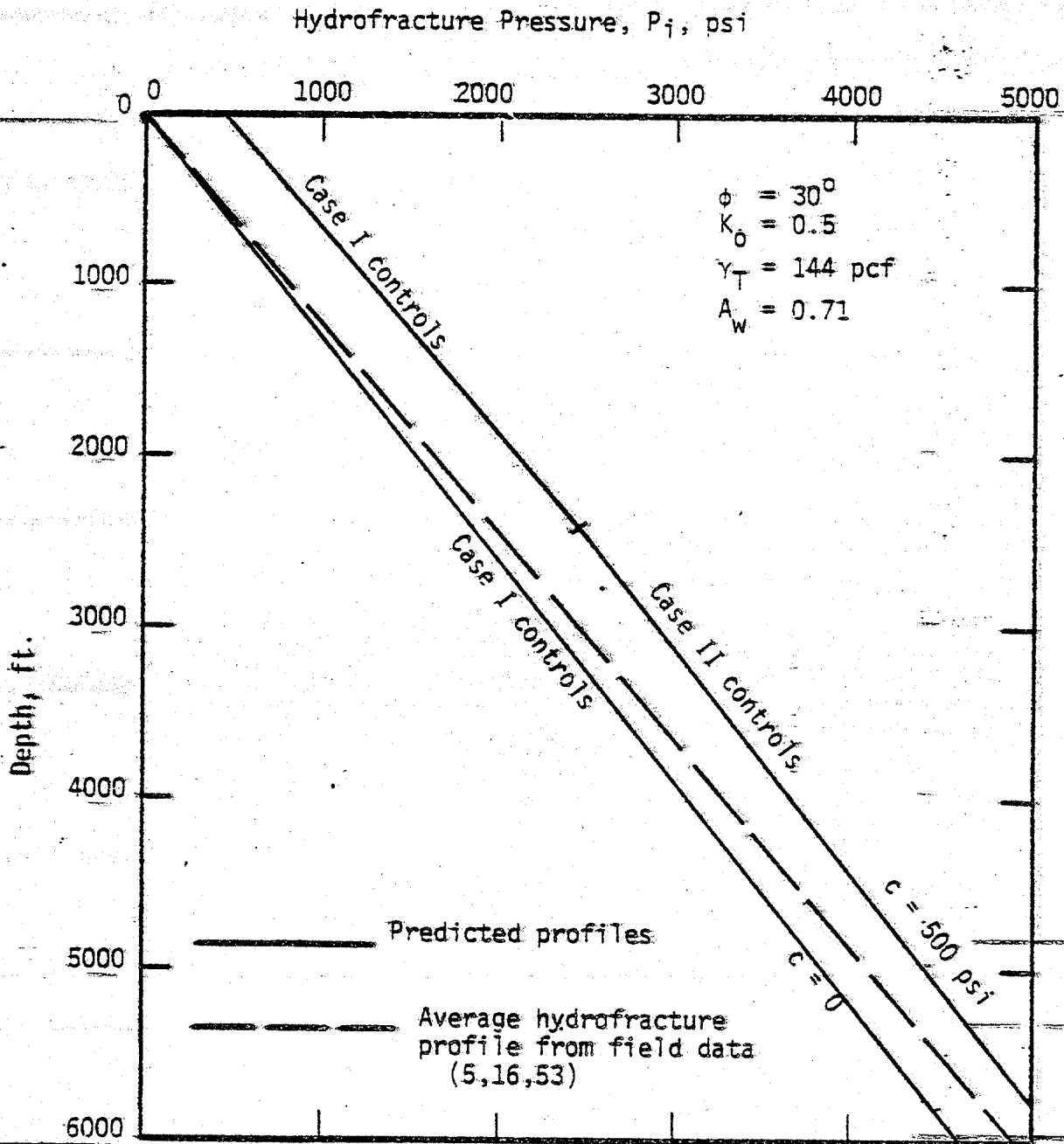


Fig. 9 - A Comparison of Predicted Hydrofracture Profiles with Field Results

One profile is for a material with no cohesion and the other is for a material with a relatively large cohesion. It can be seen that these two profiles form a tight envelope around the field data, indicating that the theoretically derived equations predicting hydrofracture pressure fit actual field results very well.

A variation in the material parameters K_0 , ϕ , c and γ_T can change the predicted hydrofracture and sloughing profiles significantly. Two sets of hydrofracture profiles are shown in Fig. 10 for K_0 values of 0.5 and 0.7 with all other parameters constant. The large difference in the two sets of profiles illustrates the dramatic influence of K_0 , emphasizing the need for accurate predictions of K_0 during drilling. Similar differences also result for a change in ϕ . Changes in c and γ_T are much less substantial.

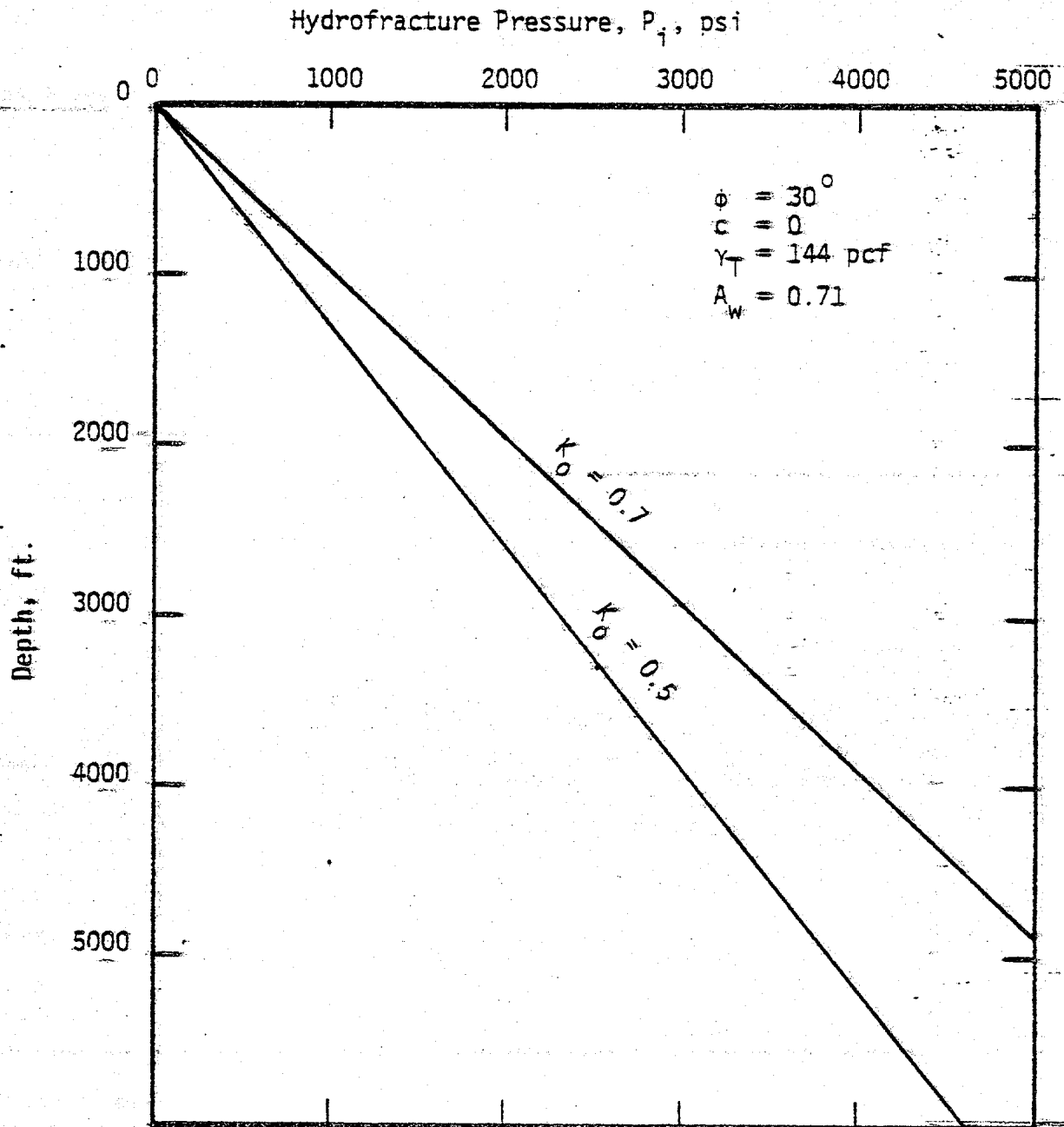


Fig. 10 - Predicted Hydrofracture Profiles
 Illustrating the Significance of K_0

CHAPTER V

LATERAL EARTH PRESSURE COEFFICIENT AT REST, K_0 Importance of K_0 in Predicting Hydrofracture Pressure

Most natural sediments are deposited in almost horizontal layers of large lateral extent. The consolidation which takes place due to the weight of the additional sedimentation occurs under conditions of essentially zero lateral yield. Under these conditions, the ratio of horizontal to vertical stresses in the soil, transmitted through the solid matrix, is termed the lateral earth pressure coefficient at rest denoted by the symbol K_0 . In terms of effective stresses, K_0 is written as:

$$K_0 = \frac{\sigma_{H'}'}{\sigma_{V'}'} = \frac{\sigma_H' - u_h}{\sigma_V' - u_v} \quad \text{--- (51)}$$

In terms of matrix stresses, K_0 is written as:

$$K_0 = \frac{\sigma_H'}{\sigma_V'} = \frac{\sigma_H' - A_w u_w}{\sigma_V' - A_w u_w} \quad \text{--- (52)}$$

assuming A_w is the same in the horizontal and vertical direction. Note that for $u_w = 0$, the two definitions of K_0 are essentially identical.

The term K_0 is only applicable to geostatic conditions where horizontal stresses are equal in all directions, as illustrated in Fig. 2 (p. 11). In addition, these stresses are assumed to be principal stresses, implying that no shear stresses act in the horizontal and

vertical planes (6).

The influence of K_0 on hydrofracture pressures was illustrated in Fig. 10 (p. 46). The magnitude of K_0 can range from less than 0.5 to greater than 2.0 depending upon the material type and stress history. This further illustrates the need for accurate knowledge of the magnitude of K_0 for hydrofracture pressure predictions during drilling. Direct measurement of stress in situ involves disturbance of the material and of the stress state. Therefore, it is doubtful that reliable K_0 determinations can be obtained through direct measurements in the field. For this reason laboratory tests have been the main source of information on the state of stress corresponding to the at rest geostatic condition. To obtain accurate values of K_0 during continuous drilling, a way is needed to indirectly predict K_0 from material properties determined from cuttings and knowledge of the overburden stress. Relationships involving K_0 and material properties which will enable such indirect predictions must be obtained from laboratory experiments.

Devices for Measuring K_0 in the Laboratory

Measurement of K_0 in the laboratory requires a device in which the material can be compressed vertically while being fully restrained in the horizontal direction by boundaries which do not set up vertical shear stresses. Various devices have been used for this purpose over the years. A summary of pioneer attempts to measure K_0 in the laboratory prior to 1950 is given by Tschebotarioff (59). In later years the devices for measuring K_0 became much more sophisticated.

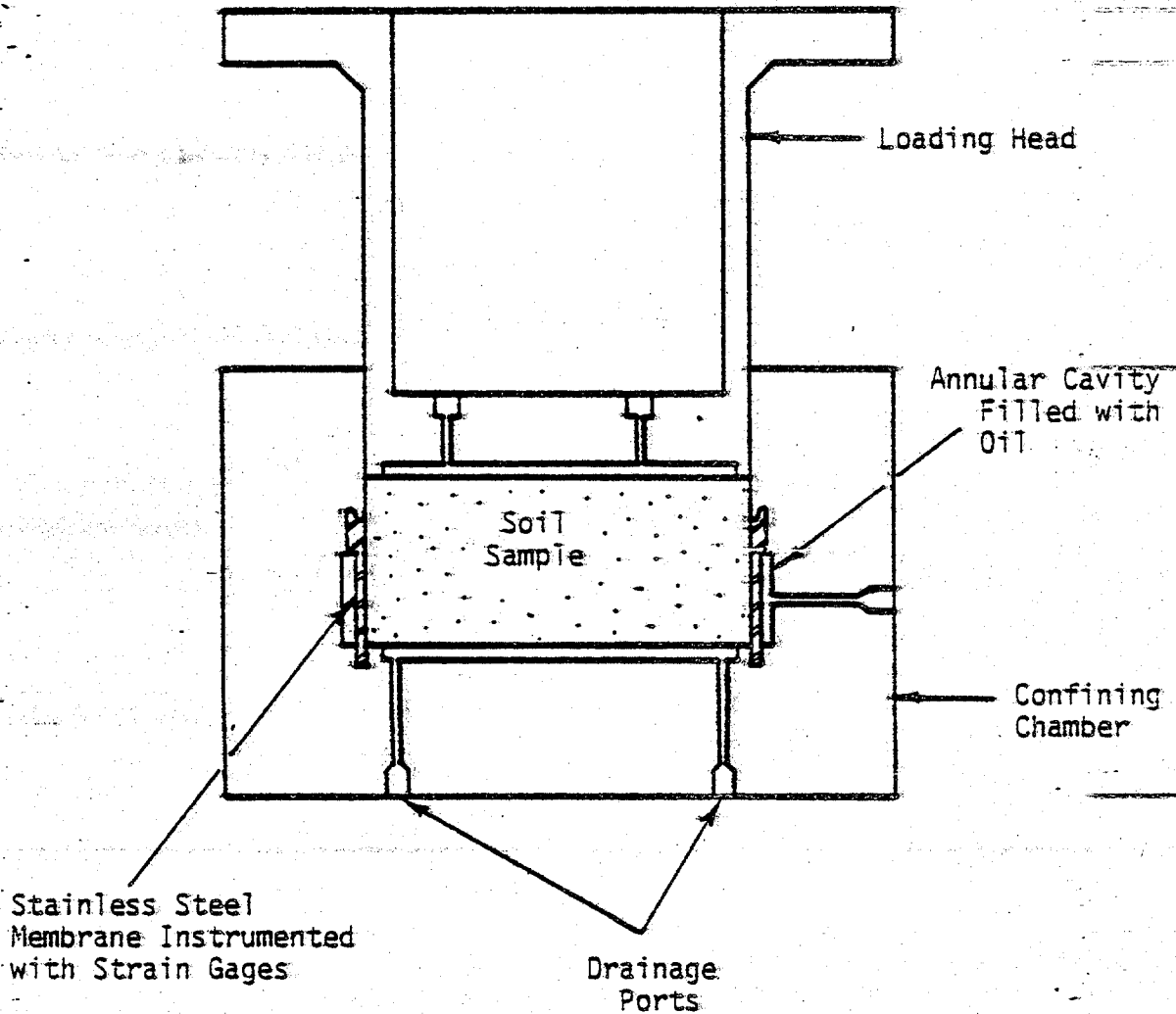
In 1962, Bishop and Henkel (8) used a triaxial cell to measure K_0 for sands and clays. In these tests lateral strains were monitored by a specially designed mechanical lateral strain indicator. The change in height of a column of mercury in this device signals lateral strains. In order to maintain a condition of zero lateral strain the confining pressure in the cell was adjusted and recorded for various levels of consolidation stress.

In 1971, Moore (36) performed similar tests on sands and silts. In these tests he used strain gages mounted on a band of foil surrounding the specimen to monitor strains. This "lateral deformation sensor", as it was called, was much more sensitive than the lateral strain indicator used by Bishop and Henkel (8).

The advantage of these triaxial tests is that vertical shear stresses on the boundary of the sample are essentially nonexistent. However, measurements of K_0 in the triaxial device have only been made for relatively low levels of stress. The maximum vertical stress applied in the triaxial tests by Moore (36) and Bishop et al. (8) was only about 100 psf (690 kN/m²).

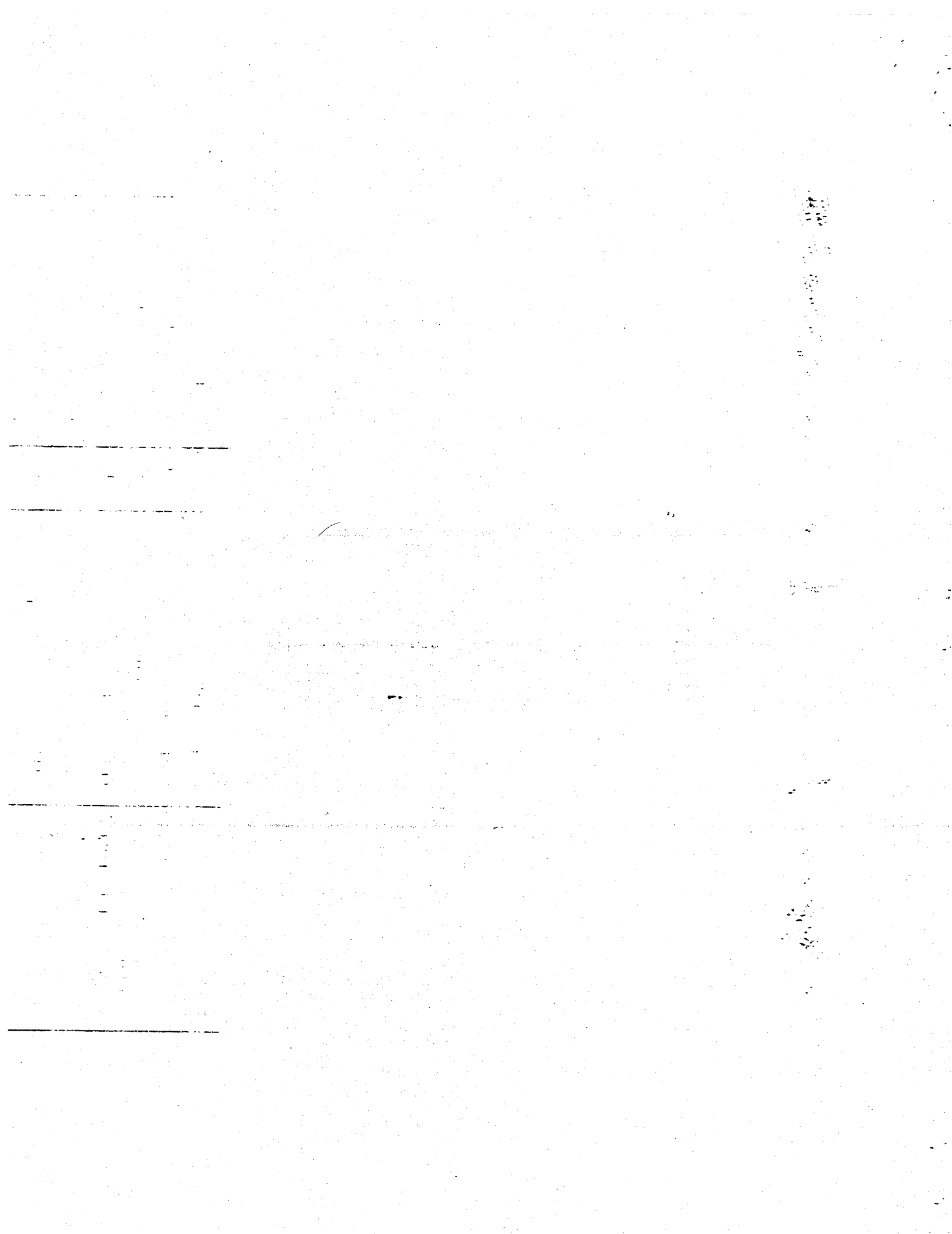
One type of device which has been used to measure K_0 by several investigators is a specially designed consolidometer with a null-type confining ring as shown in Fig. 11 (10). On the stainless steel confining ring are mounted strain gages to monitor lateral strains. Oil pressure outside the confining ring is adjusted to maintain the condition of zero lateral strain.

The advantages of such a device are that very large axial strains in the sample can be tolerated and high levels of overburden stress



Taken from Brooker and Ireland (10)

Fig. 11 - Schematic of Null-Type Consolidometer
Used by Several Investigators to Measure K_o



can be used. In 1963 Hendron (22) used this device for several sands with a maximum axial stress of about 3600 psi (24,840 kN/m²). During the same year Davisson (13) used it for undisturbed samples of playa silt carried to axial stresses of about 5300 psi (36,570 kN/m²). The same device was used two years later by Brooker and Ireland (10) for remolded clays under axial stresses up to about 2200 psi (15,180 kN/m²).

The main disadvantage of an apparatus such as this is that shear stresses develop due to friction along the boundaries during consolidation which implies that the condition simulated in the device is not the K_0 condition. Just how much this condition differs from the true K_0 condition and to what extent this affects the results has been a topic of considerable concern (30,36). The larger the magnitude of the friction which exists on the boundaries of the sample, the more effect this will have on changing the stress field during the test.

In 1969 Obricjan (38) designed a special K_0 measuring device in which ring friction during consolidation can be measured. This device has a split confining ring across which strain gages are mounted to monitor lateral deformation. The condition of zero lateral strain is maintained by adjusting screws with calibration proving rings attached to measure the null force. The friction force is measured by a split ring dynamometer. Obricjan (38) subtracted a portion of this measured frictional force from the applied overburden to account for sidewall frictional losses throughout the sample. Using this device, Obricjan tested sand samples to axial loads of only about 140 psi (966 kN/m²). He concluded that although the measured ratio of horizontal to vertical stresses is theoretically not an exact value of K_0 , the measured frictional resistance is low enough that it may not have significant

effects.

An important contribution to the question of frictional stress magnitudes at high levels of consolidating stresses was made by Akagi (2) in 1960. He reported measurements of ring friction during consolidation of clays to axial stresses exceeding 20,000 psi (138,000 kN/m²). In these tests he determined that the ring friction amounted to a maximum of about 7 percent of the applied overburden. However the significance of boundary friction in K_{α} measurements at high levels of overburden stress has not been analyzed.

In 1973 Sheriff and Strazer (49) used a device very similar to that of Obrcian to conduct tests on sands and clays in a study of the effects of stress history on K_{α} . This device is called the University of Washington Stress-Meter. The only major difference in this device and the one used by Obrcian (38) is that ring friction cannot be determined using the University of Washington Stress-Meter. The maximum overburden stress used in these tests was on the order of only a few hundred pounds per square inch.

Determinations of K_{α} for remolded Bearpaw Shale were made in 1973 by Singh, Henkel, and Sangrey (51) using a standard oedometer with a modification allowing measurement of lateral stresses in the sample during consolidation. This was done by using a small annular chamber machined into the confining ring and separated from the sample by a flexible teflon membrane. Using fluid pressure and a null indicator the condition of zero lateral strain was maintained. The maximum overburden stress was only about 100 psi (690 kN/m²).

A similar apparatus was used by Abdelhamed and Krizek (1) in

1976 to determine K_0 for kaolinite up to overburden stresses of about 250 psi. Instead of an annular chamber this device employs pressure transducers mounted in the wall of the apparatus to measure lateral stresses.

Results of Past Laboratory Measurements of K_0

The general procedure followed in determining K_0 for a material has been to load a sample in steps allowing the excess pore pressure to totally dissipate for each step. At the end of each loading increment the total horizontal stress is recorded at which time the next increment of consolidation is initiated. This same incremental procedure is followed for unloading.

It has been shown by numerous laboratory investigations that K_0 is constant for increasing incremental loading and that it increases for unloading as shown in the typical plot of horizontal stress versus vertical stress in Fig. 12 (10). For any point along the loading and unloading path K_0 is simply the horizontal stress divided by the vertical stress. The linearity of the data for loading is an indication of the consistency of K_0 for loading. In general K_0 for loading is reported as the average slope of this loading path. A summary of published K_0 values obtained in the laboratory for normally consolidated materials is found in Table 4.

Over the years various attempts have been made to relate K_0 for loading to some property of the material. Jaky (27) proposed the following equation for relating K_0 for a normally consolidated soil to the drained angle of internal friction, ϕ :

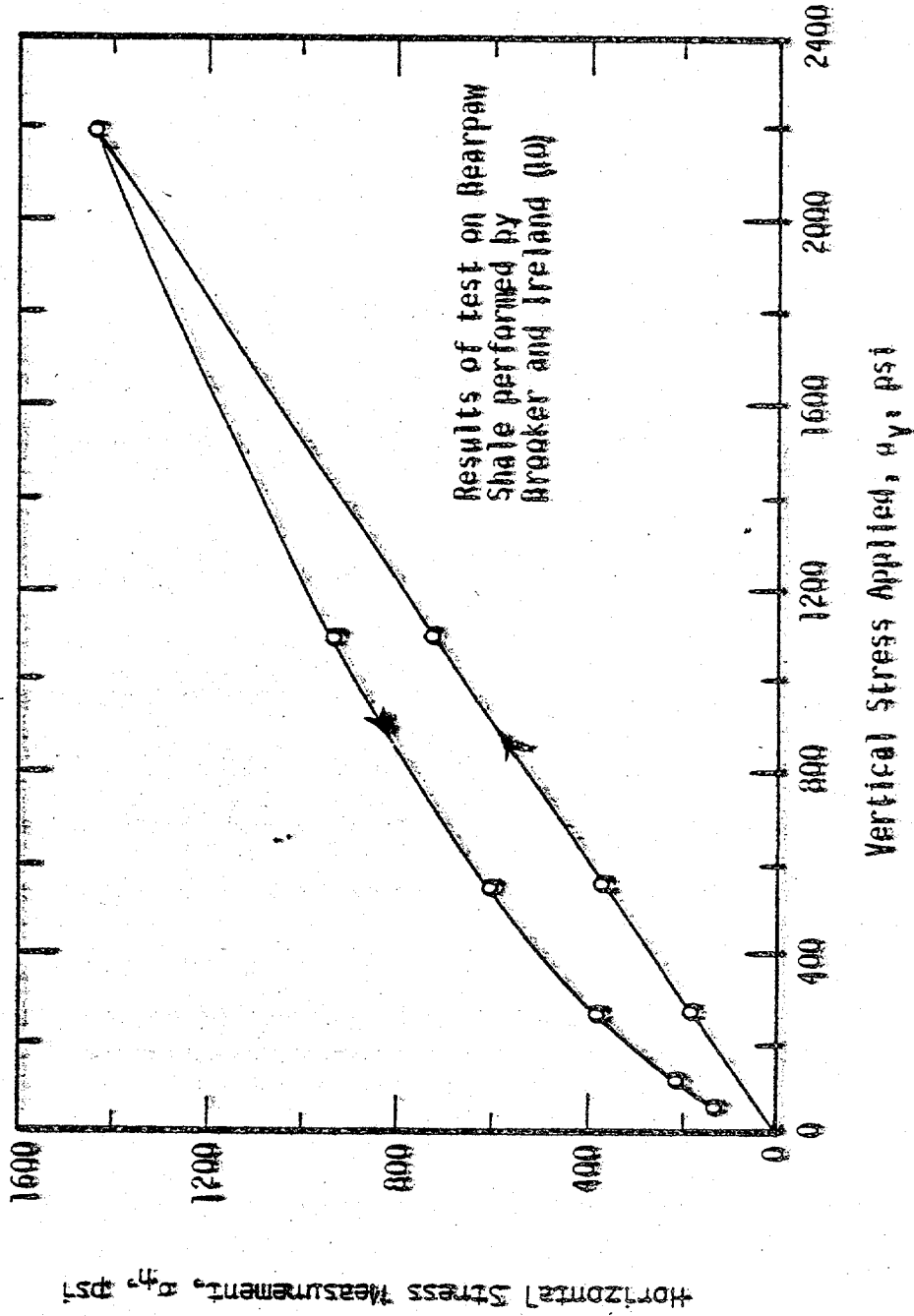


Fig. 12 - Typical Plot of Horizontal Stress Versus Vertical Stress for Loading and Unloading

TABLE 4 - Summary of Published K_o Values Obtained in the Laboratory for Normally Consolidated Soils

Investigator	Material	K_o	Other Parameters
Bishop & Henkel (8)	Moraine, compacted	.36	% clay = 1
	Boulder clay, compacted	.43	% clay = 10
	Residual clay, compacted	.42	% clay = 21
	Boulder clay, compacted	.56	% clay = 19
	Residual clay, compacted	.66	% clay = 20
	Sandy clay, undisturbed	.43	% clay = 15
	Clay, remolded	.70	% clay = 40
	Raw sugar, dry	.50	
Bishop (6)	Loose lead shot, dry	.44	
	Loose sand, saturated	.46	$\phi = 34^\circ$
	Dense sand, saturated	.36	$\phi = 39^\circ$
	Yarmouth organic silty clay, undisturbed	.57	$\phi = 27.5^\circ, PI = 45.4$
	Kaolth, remolded	.64-.70	$\phi = 20.2^\circ, PI = 23.0$
	Chew Stoke sand/ clay, undisturbed	.43	$\phi = 33^\circ, PI = 10$
Weald clay, remolded	.71	$\phi = 22^\circ, PI = 25$	

TABLE 4 (continued)

Investigator	Material	K_D	Other Parameters
Obriclan (38)	Loose fine sand	.34	
	Dense fine sand	.31	
	Loose coarse sand	.37	
	Dense coarse sand	.34	
	Loose coarse to fine sand, trace silt	.41	
	Dense coarse to fine sand, trace silt	.34	
Gebertowicz & Medzinski (11)	Corn	.46	$\phi = 24.7^{\circ}$
	Steel spheres, 1/16 in. dia.	.68	$\phi = 16.9^{\circ}$
	Siliceous sand	.40	$\phi = 32.7^{\circ}$
	Calcareous sand	.29	$\phi = 35.8^{\circ}$
	Silt	.28	$\phi = 31.4^{\circ}$
	Silt	.28	$\phi = 32.9^{\circ}$
	Silt	.28	$\phi = 33.2^{\circ}$
	Alpestre clay	.45	$\phi = 26.3^{\circ}$
Brooker and Ireland (10)	Chicago clay	.42	$\phi = 26.3^{\circ}$, $PI = 10.3$
	Goose Lake Flour	.47	$\phi = 27.5^{\circ}$, $PI = 15.6$
	Wald clay	.51	$\phi = 22^{\circ}$, $PI = 20.6$
	London clay	.63	$\phi = 17.5^{\circ}$, $PI = 38.4$

TABLE 4 (continued)

Investigator	Material	K_0	Other Parameters
Brooker & Ireland (10) (continued)	Bearpaw clay	.65	$\phi = 15.5^\circ$, PI = 78
Abdelhamid and Krizek (1)	Kaolinite	.68-.69 .66-.75	$\phi = 16.9^\circ$, PI = 28 $\phi = 17.8^\circ$, PI = 28
Singh, Henkel and Sangrey (51)	Bearpaw shale	.65	$\phi = 21^\circ$, PI = 64
Hendron (22)	Wabash River sand	.38 .40 .42 .43 .45	$\phi = 41.8$ $\phi = 40.0$ $\phi = 38.0$ $\phi = 36.5$ $\phi = 33.9$
	Pennsylvania sand	.43 .45 .48 .51 .52	$\phi = 38.1$ $\phi = 36.6$ $\phi = 33.9$ $\phi = 32.2$ $\phi = 31.0$
	Sangamon River sand	.40 .41 .42	$\phi = 39.0$ $\phi = 37.2$ $\phi = 36.0$

TABLE 4 (CONTINUED)

Investigator	Material	K_0	Other Parameters
Hendron (22) (CONTINUED)	Saugamon River sand Minnesota sand	.43	$\phi = 34.6$
		.44	$\phi = 32.5$
		.33	$\phi = 35.5$
		.35	$\phi = 34.0$
		.38	$\phi = 31.0$
		.39	$\phi = 28.5$
Davisson (13)	Playa silt	.56	PI = 7.2
		.48	PI = 7.4
		.47	Non-plastic
		.55	PI = 6.9
		.56	PI = 6.5
		.51	PI = 5.9
		.49	PI = 10.2

$$K_0 = 1 - \sin \phi \dots \dots \dots (53)$$

Hendron (22) showed that this relationship fit his test results on sand very well. Brooker and Ireland (10) showed that the following relationship is perhaps more applicable to clays:

$$K_0 = 0.95 - \sin \phi \dots \dots \dots (54)$$

Fig. 13 graphically shows how these relationships fit various sets of K_0 test results for normally consolidated soils plotted against ϕ . Considerable scatter of the data exists in this plot indicating that ϕ is not a unique parameter for the value K_0 . Furthermore, it is interesting to note that since the value of ϕ decreases with increasing stress then according to these relationships, K_0 should increase with stress (31, 48). This trend is not observed in past K_0 determinations.

Other attempts have been made to relate K_0 to the plasticity index of the material. The work of Brooker and Ireland (10) shows a very good correlation between K_0 and the plasticity index, PI. However, Bishop (6) reported a similar set of data which showed no such unique relationship. Both sets of data are shown in Fig. 14.

Since K_0 does not remain constant for unloading or, more specifically a rebounding soil, some investigators have tried to somehow relate K_0 to the stress history of the material. This has been done by observing the change in K_0 with the overconsolidation ratio, OCR, where the OCR is the maximum stress the soil has ever been exposed to,

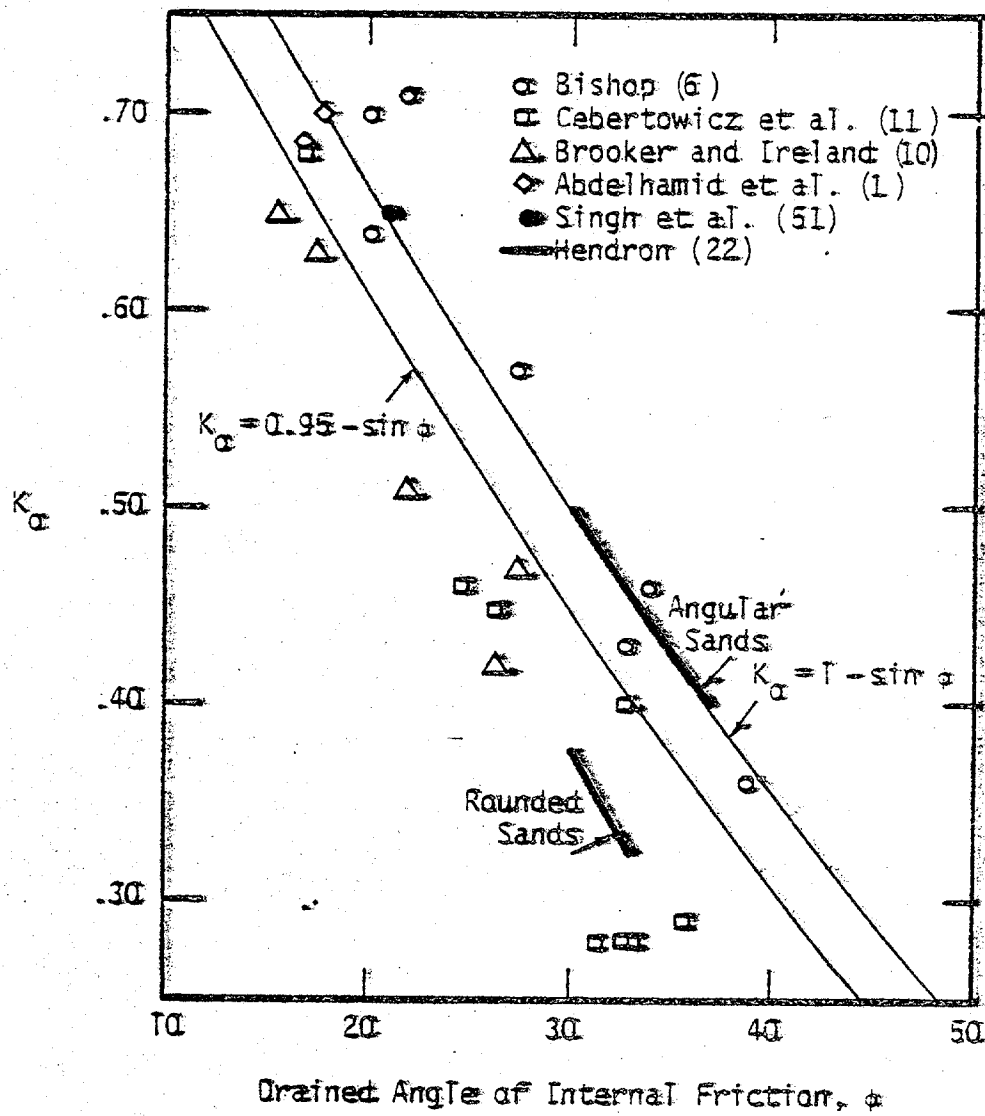


Fig. 13 - Previous Data Compared to Relationships Between K_a and ϕ

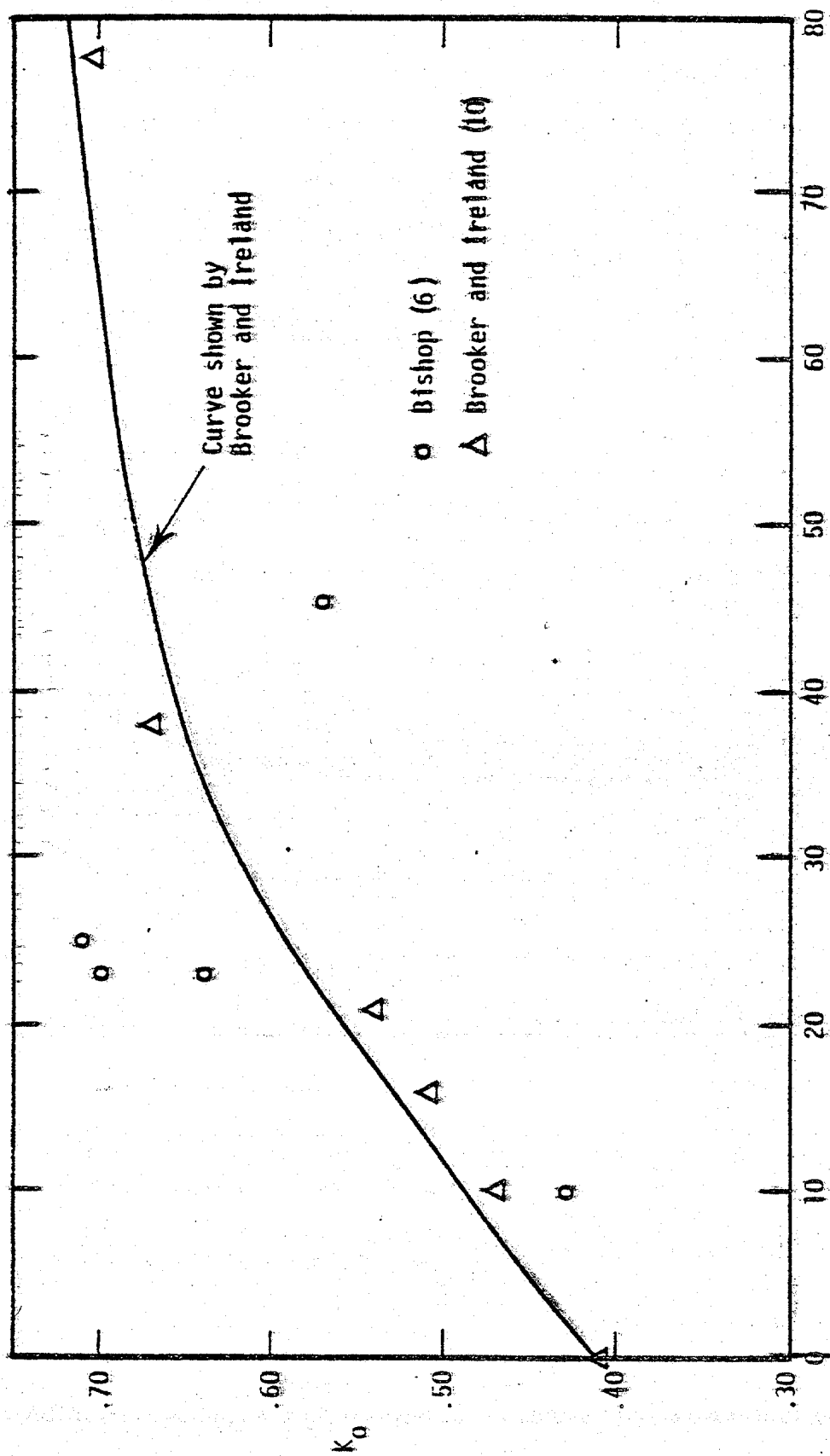


Fig. 14 - Previous Data Showing No Unique Relationship Between K_0 and PI

divided by the present stress on the soil. Brooker and Ireland (10) show that K_0 increases with the OCR asymptotically approaching the value of the passive lateral earth pressure coefficient, K_p . The value K_p is obtained from the cohesion and drained angle of internal friction of the material.

Schmidt (48) later used several sets of unloading K_0 data to study the effects of the OCR. By plotting K_0 versus the OCR on a log-log scale he showed that a straight line could be obtained in most cases. This is shown by the two sets of data in Fig. 15(48). He fits a straight line through the data using the following power law function:

$$K_{\sigma_{rb}} = K_{\sigma_{nc}} (\text{OCR})^x \quad \text{--- (55)}$$

where $K_{\sigma_{rb}} = K_{\sigma}$ for rebound

$K_{\sigma_{nc}} = K_{\sigma}$ for normal consolidation

$x =$ factor depending upon soil type

Schmidt (48) noted that this relationship may not be accurate for high values of the OCR which is demonstrated by the curved path which Bishop's data follows in Fig. 15. Very few measurements of K_0 have been made for samples that have been reloaded after rebounding. Therefore, the behavior of K_0 for reloading has not been examined adequately (48).

Description of Testing Apparatus

In most marine environments the elevation of the mudline is constantly being altered due to the combined processes of sedimentation, erosion and consolidation. Therefore the overburden stress on a particular sediment is continually changing - usually increasing. In order to study the behavior of a sediment in the laboratory, an elaborate high pressure consolidation system was developed which simulates this process of progressive burial and continual consolidation. Fig. 16 is a schematic representation of this experimental system.

Two basic differences exist between the experimental simulation system and the actual process of progressive burial. The first is the period of time involved. The experimental process takes only a matter of days to simulate a geologic process which may occur over thousands of years. The second basic difference is the temperature at which these processes occur. In the earth a thermal gradient exists of around $1.1^{\circ}\text{F}/100\text{ ft}$ ($2^{\circ}\text{C}/100\text{ m}$) of depth on the average (35). However all of the laboratory experimentation in this research was conducted at room temperature.

The major constituent of the experimental system consists of a high pressure consolidometer similar to the one used by Hendron (22).

A schematic drawing of the consolidometer is shown in Fig. 17. The consolidometer is constructed of stainless steel to prevent corrosion due to the salinity of the pore fluid. It is designed to handle soft samples 2.5 in. (6.4 cm) in diameter and up to 3.0 in. (7.6 cm) in height. Conditions of double-drainage are imposed during consolidation by means of carborundum porous stones positioned above

CHAPTER VI

EXPERIMENTAL PROGRAM

Scope of the Experimentation

The experimental portion of this research is designed to study the lateral stress behavior of various soils under conditions simulating those expected in the earth at depths of up to 10,000 ft (3048 m). Information on the following items of concern is to be gained from the experimental results:

1. The behavior of K_0 at stresses higher than have previously been accomplished during K_0 testing.
2. The effects of boundary friction on K_0 determinations at high levels of stress.
3. The correlation of these results with past proposed relationships involving K_0 , material type, and stress history.
4. The correlation of these results with any other relationships not already proposed.
5. The behavior of K_0 during reloading.
6. The magnitude of A_w as used in the matrix stress concept.

This is done in an attempt to find a way of predicting the magnitude of K_0 during continuous drilling which will aid in the prediction of borehole pressures for which failure is induced in the material surrounding the borehole.

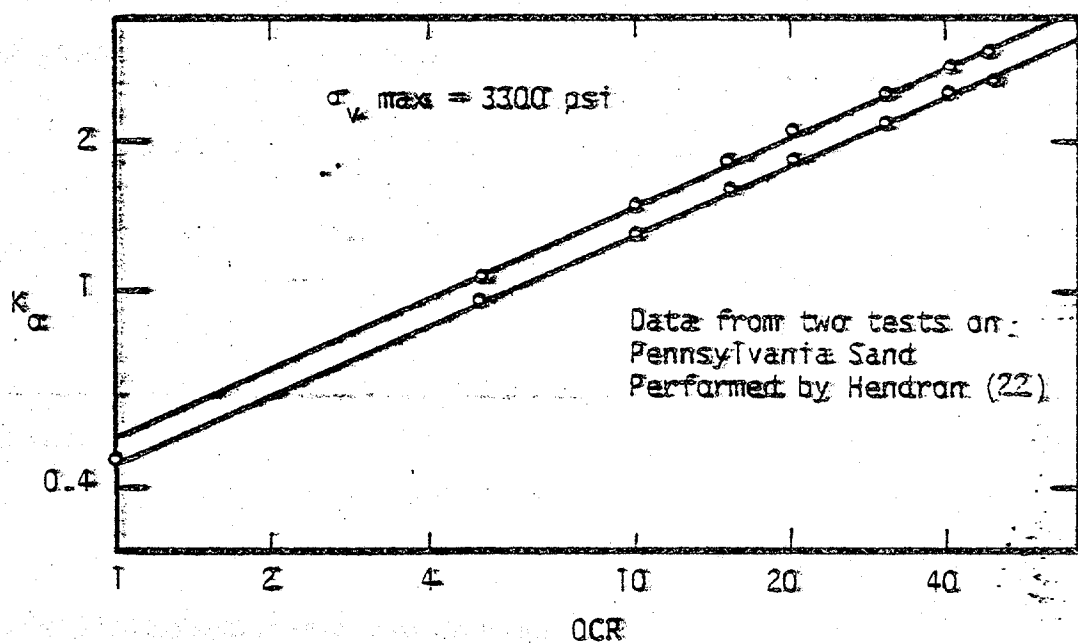
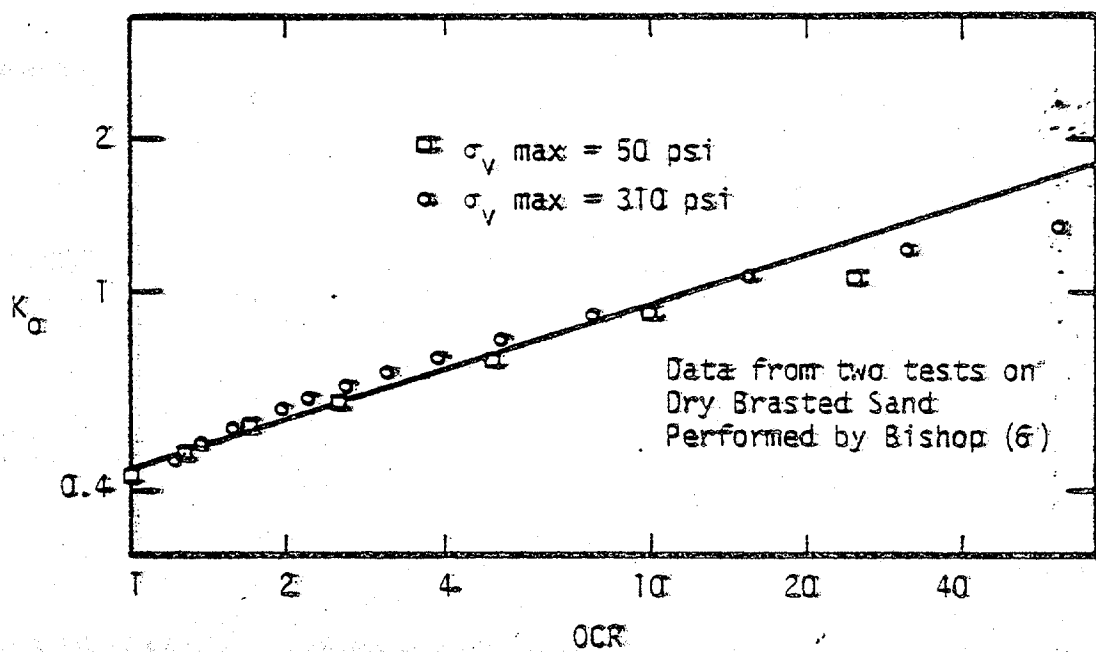


Fig. 15 - Typical Relationships Between K_α and OCR as Observed by Schmidt (48)

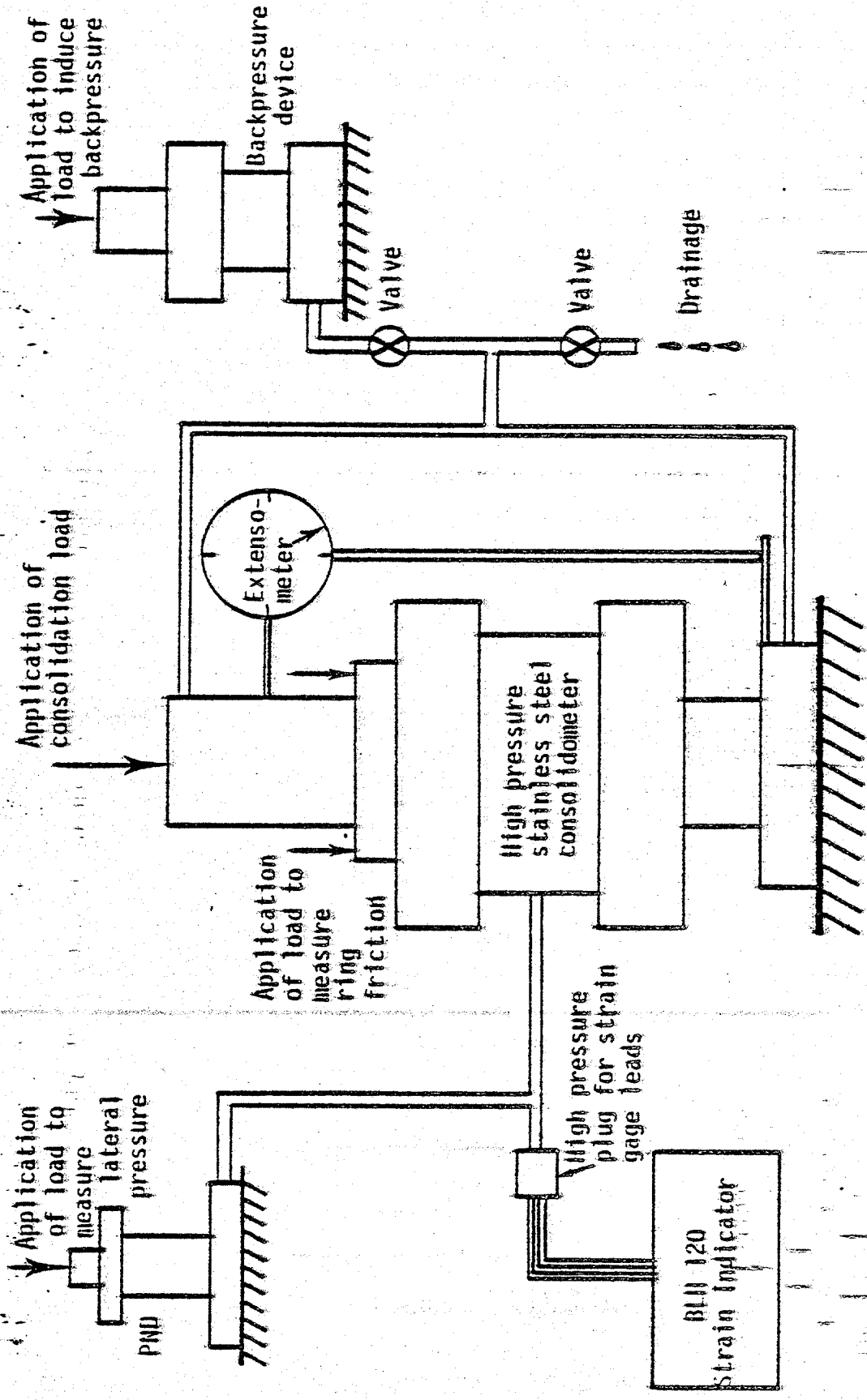


Fig. 16 - Schematic of High Pressure Consolidation System

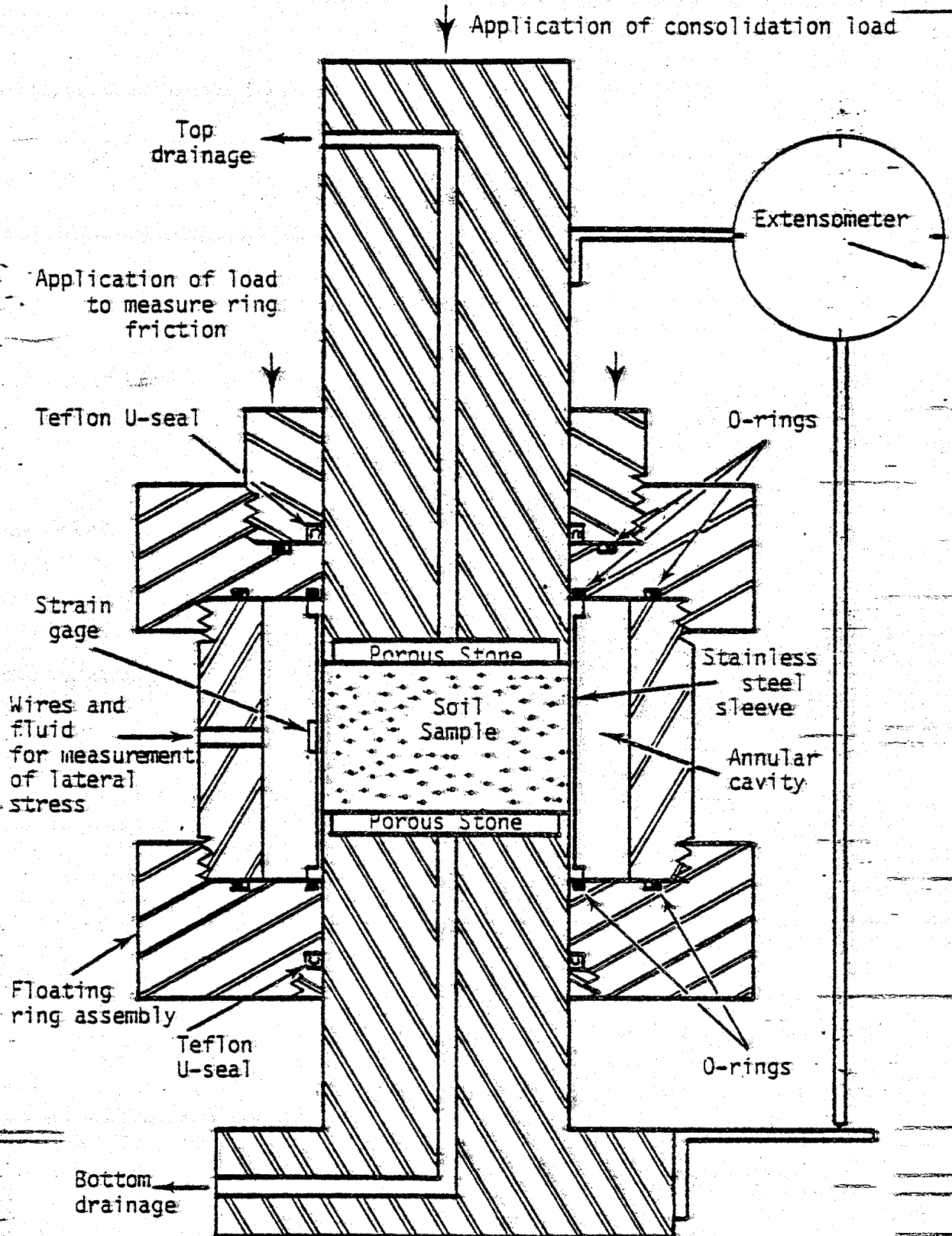


Fig. 17 - Cross-sectional Schematic View of High Pressure Stainless Steel Consolidometer

and below the sample. Changes in sample height can be determined at any time during a test by monitoring an extensometer attached to the upper and lower pistons.

One of the unique capabilities of the device is to measure lateral stresses exerted by the sample under conditions of virtually no lateral strain. These stresses are measured by controlling strains in a thin stainless steel sleeve surrounding the soil chamber. The wall thickness of the sleeve is only 0.040 in. (0.102 cm). A tiny electrical strain gage is mounted at midheight on the outer surface of the sleeve. The orientation of the strain gage is such that minute radial motions can be detected at the gage point in the sleeve. A temperature compensating gage is mounted on a cantilever attached to the sleeve to eliminate possible effects of small changes in temperature. The strains are monitored on a separate strain indicator unit mounted on the loading frame.

An annular cavity surrounds the sleeve enclosed by rigid boundaries. The cavity is filled with automatic transmission fluid which has a low viscosity and is a poor conductor of electricity, eliminating the possibility of electrical shorts in the strain gages. By altering the fluid pressure in the annular cavity, a condition of no lateral strain can be maintained. The fluid pressure can be changed by increasing the load on a separate piston-cylinder device called the PND (Pressure Nullification Device) shown in Fig. 16 (p. 66). Stainless steel tubing links the annular cavity with the PND.

By knowing the magnitude of strain in the sleeve, or the fluid pressure necessary for a nullified condition of strain, it is possible to

determine the horizontal stress exerted by the soil sample. This is done by referring to one of two calibration curves. The low pressure calibration curve in Fig. 18 shows the magnitude of circumferential strain, ϵ_c , expected in the sleeve for a given horizontal stress from within the soil chamber. For the low pressure determinations no fluid pressure exists in the annular cavity. This allows the sleeve to expand freely. In order to prevent plastic deformation of the sleeve the circumferential strains are kept below 400 microstrains which corresponds to a horizontal pressure of about 400 psi (2760 kN/m²). For pressures exceeding 400 psi (2760 kN/m²) the pressure in the annular cavity is increased to nullify all strain in the sleeve. The high pressure calibration curve in Fig. 19 shows the magnitude of a fluid pressure, p_n , necessary in the annular cavity to nullify the effects of a particular horizontal stress inside the soil chamber. Both of these relationships were obtained by inducing a known hydrostatic pressure in water within the soil chamber and recording either the resulting strain or the pressure in the annular cavity necessary to nullify the strain. Both relationships are linear with outstanding correlation with the calibration data.

Another separate component similar to the strain null device is used as a backpressure device to induce a known pore pressure within the soil chamber for a particular phase of the experimentation. During this phase the backpressure device is linked to the top and bottom drainage outlets with stainless steel tubing as shown in the schematic drawing in Fig. 16 (p. 66).

Another unusual characteristic of the consolidometer is that it is a floating ring, type which means that the entire confining ring assembly

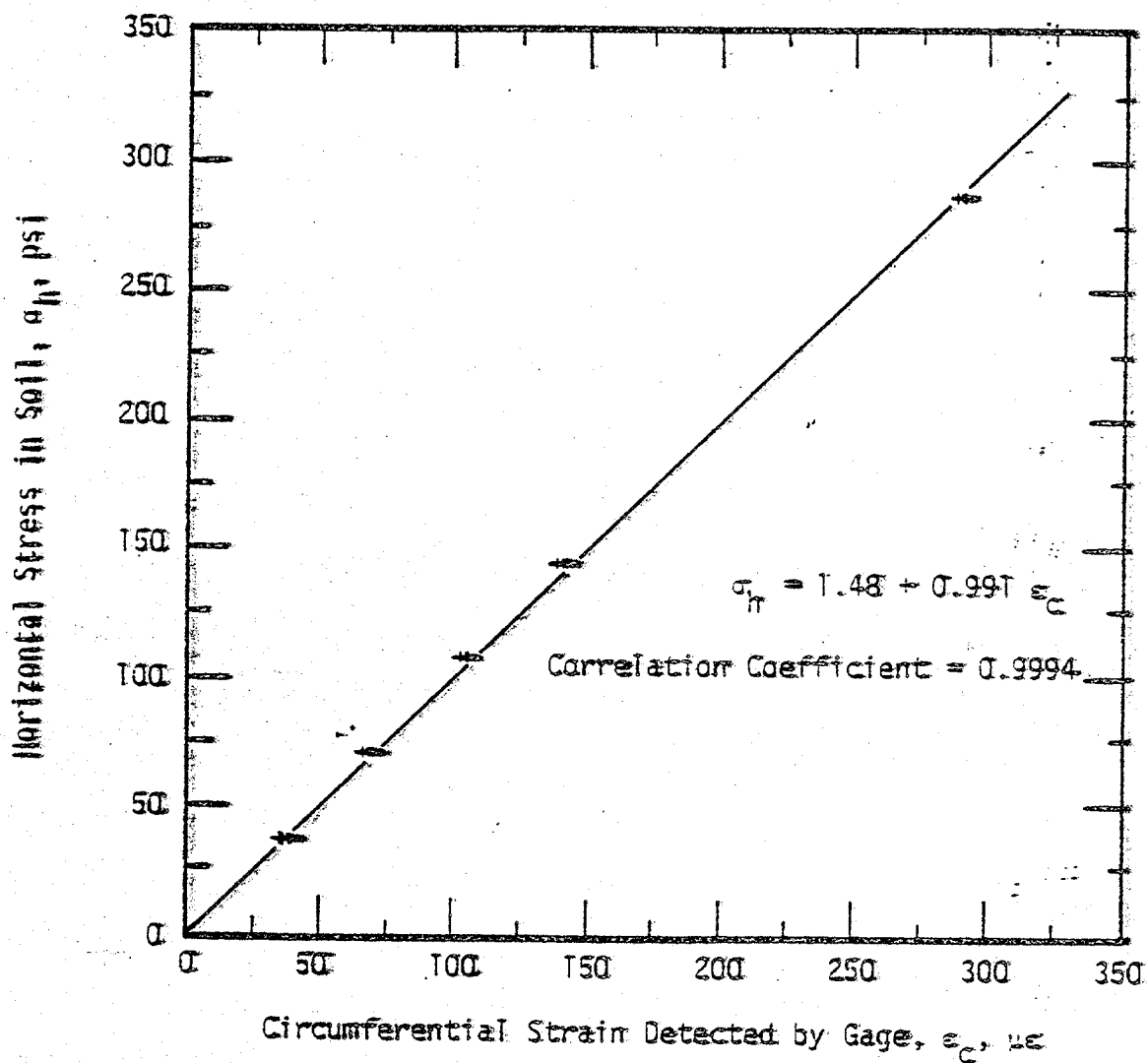


Fig. 18 - Low Pressure Calibration Curve for Determining Horizontal Stresses in Soil

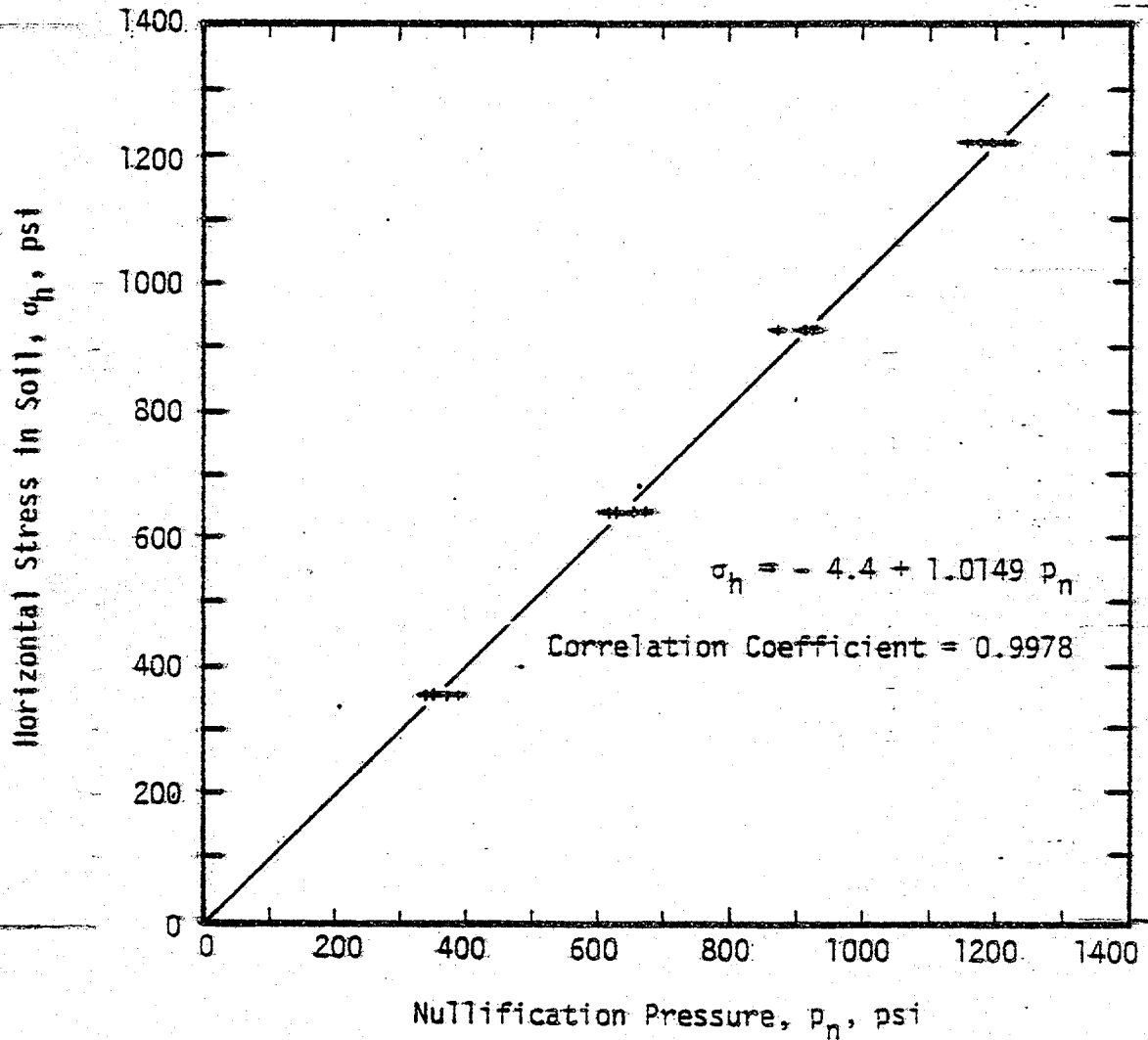


Fig. 19 - High Pressure Calibration Curve for
Determining Horizontal Stresses in Soil

can be moved vertically with respect to the soil sample and the pistons. This enables positioning of the sleeve such that the point of strain measurement is always aligned with the center of the sample. Another advantage of the floating ring is that the magnitude of the ring friction can be determined. This is done by applying a vertical load to the floating ring assembly by means of a single removable lever arm. This vertical load is increased until vertical motion of the ring begins. The force resisting vertical motion of the ring assembly is equal to the force due to friction between the pistons and the sleeve, and the soil and the sleeve. A portion of the frictional force is then added to or subtracted from the overburden load as shown in detail in Appendix III.

A major setback in developing the experimental system was in finding seals and fittings which could withstand fluid pressures from zero to 10,000 psi ($69,000 \text{ kN/m}^2$) and still be adaptable to the testing apparatus. All of the valves, fittings and tubing used are manufactured by the High Pressure Equipment Company in Erie, Pennsylvania. Each of these items is designed to withstand fluid pressures in excess of 10,000 psi ($69,000 \text{ kN/m}^2$). The seals used around the pistons in each of the devices described are teflon coated U-seals manufactured by Fluorocarbon in Los Alamitos, California. These seals were found to be virtually frictionless even at high pressures. A special plug was designed to transfer the four electrical strain gage leads from an environment of extremely high fluid pressure to atmospheric pressure. This special fitting is shown in Fig. 20.

To induce pressures, three separate loading mechanisms are

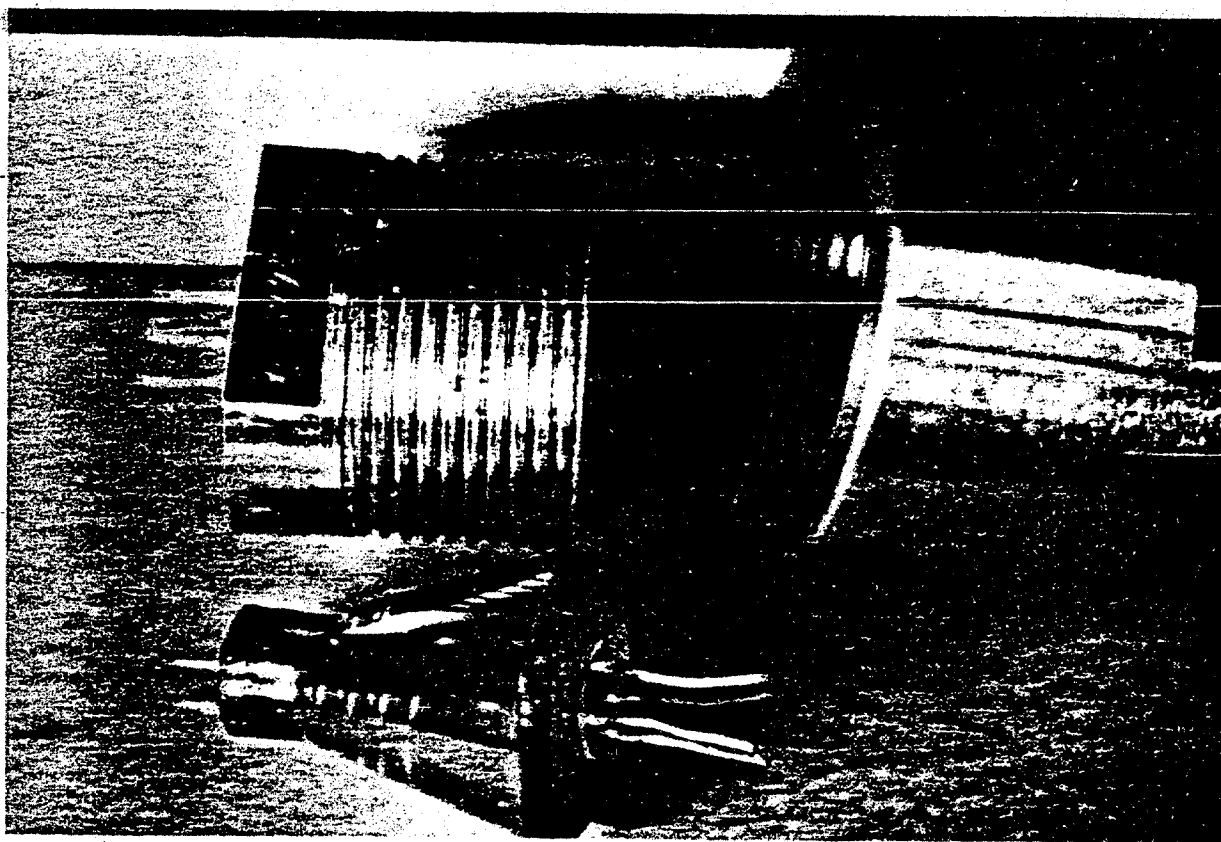
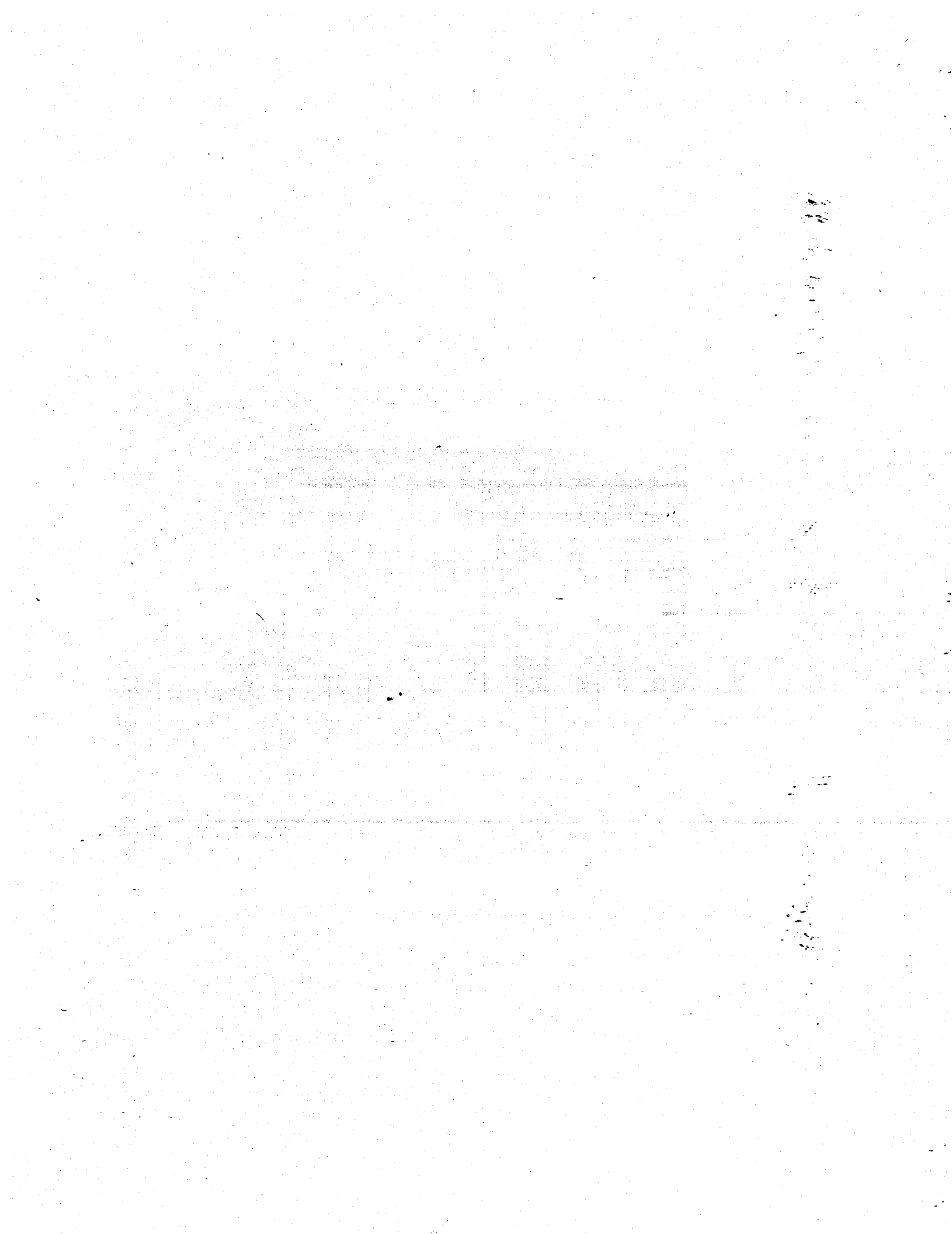


Fig. 20 - Specially Designed High Pressure Electrical Connector



replaced and pushed downward until slight contact is made with the soil grains.

All of the samples used in the experimentation contain seawater as a pore fluid. Three different preparation techniques are used depending upon the type of soil.

One type of samples tested was clean sand. These samples require little preparation. The soil chamber is filled with a seawater solution and the clean, dry sand is then slowly poured into the chamber displacing the excess seawater until the desired sample height is reached. The sample height is recorded and later used to calculate the initial porosity. This method of preparation results in a high initial porosity of the sample with little to no entrapped air.

A second type of samples tested was undisturbed clay cores. Again little preparation is required. These samples are initially extruded from Lucite coring tubes. One end of the extruded sample is trimmed flat and the sides of the core are trimmed to the same diameter as the soil chamber. The core is cut off flat at a desired length and then pushed into the soil chamber until it contacts the bottom piston. It is assumed that the degree of saturation in the undisturbed samples is very high and no attempt is made to insure 100 percent saturation. The moisture content is determined from an adjacent portion of the core which is used to calculate initial porosity.

The third type of samples tested was remolded clays and clay-sand mixtures. These samples are thoroughly mixed with a seawater solution until a slurry is obtained. Since this process entraps a considerable amount of air in the soil pores, a vacuum is applied while the sample

incorporated within the experimental system. Each loading mechanism consists of a deadweight compound lever system. A deadweight lever system was chosen over a hydraulic loading system because no calibration is needed to find the applied force. Only the distances between the fulcrums and the points of load application are needed to determine the lever arm ratio. No hydraulic regulators or pressure gages are needed which makes a lever system much less expensive.

One of the lever systems is used for application of a vertical load to the consolidometer. Its lever arm ratio is 80 to 1 and it is capable of applying an overburden stress in excess of 10,000 psi (69,000 kN/m²) to the sample.

Another of the lever systems is used to apply a load to the PND. Its lever arm ratio is 47 to 1 and it is capable of producing a nullification pressure up to 10,000 psi (69,000 kN/m²).

The third lever system is used to apply a load to the backpressure device. Its lever arm ratio is 100 to 1 and it is capable of producing a pore pressure within the sample up to 10,000 psi (69,000 kN/m²).

Preparation and Placement of the Samples

In placing a sample in the soil chamber of the consolidometer the top piston is removed and the confining ring assembly is held up by tiny screw jacks. The walls of the confining ring are coated with castor oil to reduce ring friction. Two layers of filter paper are placed between the sample and the porous stones to prevent washout of the sample through the top and bottom drainage outlets during consolidation. After placing the sample into the soil chamber the piston is

Weight is added to the removable lever positioned on the floating ring assembly until downward motion of the assembly commences. This weight is recorded and is used to alter the applied overburden load as shown in Appendix III. An additional consolidation pressure is then applied and the entire cycle is repeated.

This incremental loading procedure is continued to a maximum consolidation pressure of around 10,000 psi (69,000 kN/m²). The sample is then incrementally unloaded and allowed to rebound. The same measurements of height change, lateral stress and friction are made for unloading. Some of the samples were subjected to several of these loading and unloading cycles before completely unloading and removing them from the consolidometer.

Upon removal of a sample the total weight of the sample is recorded and a portion of the sample is oven-dried to determine the final moisture content. This data is used in combination with the dial readings and specific gravity determinations to calculate sample porosity throughout the test.

Procedure for Measuring A_w

The purpose of this phase of the experimentation is to determine the magnitude of the water area, A_w , for two different materials with a range in porosities.

For these tests the backpressure device is linked to the top and bottom drainage outlets. The procedure is exactly the same as for K_o determinations except that one additional set of measurements is made for each loading increment. This additional set of measurements is the

is agitated for several hours to remove the air. The slurry is then slowly poured into the soil chamber until the desired sample height is reached. The moisture content of the slurry is determined so that the initial porosity may be computed.

Sequence of Testing Procedure to Determine K_0

After the sample is placed in the soil chamber and the top piston is replaced, the consolidometer is positioned under the loading mechanism. The linkage to the PND is connected and the leads from the strain indicator are soldered to the terminals on the high pressure plug. An initial strain gage reading is recorded which will remain the nullification reading throughout the experiment. The extensometer is also attached and an initial dial reading is recorded.

The first consolidating pressure is applied and drainage of pore fluid is allowed. As drainage continues, the sample reduces in height corresponding to a change in porosity. During this process dial readings are recorded so that the change in sample height and therefore the porosity can be monitored. When secondary consolidation is reached, the pore pressure within the sample has reduced to zero, and virtually no further change in sample height will occur. Therefore, a final dial reading is recorded. This process may take as little as a few seconds for the sand samples and as much as 48 hours for the high plasticity clay samples. The strain in the sleeve is also recorded, or, for strains near or above 400 microstrains, the nullification pressure is recorded. This allows the computation of lateral stress exerted by the soil and therefore K_0 . Finally a ring friction measurement is made.

CHAPTER VII

PRESENTATION AND DISCUSSION OF RESULTS

Description of Soil Samples Tested

Seven different soils were used in the experimental portion of the research. Two of the soils were clean uniformly graded sands. Two of them were marine clays obtained from offshore soil borings. The other three were commercial clay minerals. Each of these soils is described in more detail below.

Kaolinite - - - commercial clay material supplied in a dried powder form; mineralogy - 95% kaolinite, 4% illite, 1% illite-chlorite mixed-layer, trace amount of quartz.

Illite - - - - commercial clay material supplied in a dried powder form; mineralogy - 85% illite, 10% kaolinite, 5% montmorillonite.

Bentonite - - - commercial drilling mud supplied in a dried powder form; mineralogy - 100% montmorillonite, trace amount of quartz.

Sand I - - - - uniform graded clean sand; gradation shown in Fig. 21.

Sand II - - - - Ottawa sand, uniform graded, rounded grain, clean sand; gradation shown in Fig. 21.

Marine Clay I - obtained from core taken in Angola Basin off the West Coast of Africa; depth of water = 15,000 ft (4572 m); depth below mudline = 700 ft (213 m); mineralogy - 37% illite, 36% kaolinite, 22% montmorillonite, 5% chlorite.

Marine Clay II - obtained from core taken in Angola Basin off the West

change in total lateral stress due to known increases in pore pressure throughout the sample. After the lateral stress exhibited by the soil with zero pore pressure is measured, a known increase in pore pressure is induced by the backpressure device. This increase in pore pressure causes an increase in the total lateral stress against the sleeve thereby requiring an increase in the nullification pressure. During this process no vertical motion of the pistons is allowed and it is assumed that no change in the volume of solids occurs. Therefore, the stress state in the soil grains is assumed to remain constant. After the pore pressure has been allowed to equilibrate throughout the sample, the new nullification pressure is recorded. An additional increase in the pore pressure is then induced and the corresponding nullification pressure is recorded. The pore pressure is incrementally increased in this manner several times and then allowed to dissipate back to zero. At this time the ring friction is measured and an additional consolidation pressure is added to continue the progressive burial simulation process.

Coast of Africa; depth of water = 15,000 ft (4572 m);
 depth below mudline = 700 ft (213 m); mineralogy -
 not available.

A total of nineteen separate tests were performed on samples made up of one or more of these seven soils. The soil constituents of each of the nineteen samples are listed in Table 5 along with the identification numbers assigned to each test. Also contained in Table 5 are the specific gravities, Atterberg Limits, initial sample heights, and initial porosities, for each sample.

Typical Results

The following results represent measurements for which $u = 0$; therefore,

$$\sigma = \bar{\sigma} = \sigma^h \text{ ----- (56)}$$

Furthermore, since $u = 0$, both the effective stress and matrix stress definitions of K_{σ} are identical.

Fig. 22 is a plot of horizontal total stress versus vertical total stress obtained for a single cycle of loading for kaolinite sample K-4. As indicated by the linearity of the loading path in the curve, K_{σ} is constant for loading even at the high levels of stress, which agrees with results of previous investigations for lower levels of stress. This was found to be a typical trend for all of the nineteen samples tested. The loading value of K_{σ} is taken as the slope of a line passing through the origin and through the loading data points.

Table 5 (Cont'd.)

Sample I.B. No.	% By Weight of Soil Constituents	Specific Gravity	Atterberg Limits*			Initial Sample Height In.	Initial Porosity %
			LL	PL	PI		
OS-2	100% sand II	2.65	-	-	NP	2.000	39.6
OS-3	100% sand II	2.65	-	-	NP	2.416	39.2
MC-I-U	100% marine clay I, undisturbed	2.83	72.0	25.8	46.2	1.381	51.4
MC-I-R	100% marine clay I, remolded***	2.83	72.0	25.8	46.2	1.461	71.9
MC-II-U	100% marine clay II, undisturbed	2.76	127.5	73.7	53.8	2.307	74.2

* Distilled water was used for the admixture after the samples were saturated and consolidated with seawater

** Non-plastic

*** The sample from test No. MC-I-U was removed and completely remolded to a slurry state for use in test No. MC-I-R

Table 5 - Description of Samples Used in Testing

Sample I.D. No.	% By Weight of Soil Constituents	Specific Gravity	Atterberg Limits*			Initial Sample Height In.	Initial Porosity %
			LL	PL	PI		
K-1	100% kaolinite	2.64	55.0	34.8	20.2	0.653	74.0
K-2	100% kaolinite	2.64	55.0	34.8	20.2	0.987	73.2
K-3	100% kaolinite	2.64	55.0	34.8	20.2	1.703	74.2
K-4	100% kaolinite	2.64	55.0	34.8	20.2	1.942	75.1
K-5	100% kaolinite	2.64	55.0	34.8	20.2	2.314	74.5
KS-1	75% kaolinite, 25% sand I	2.66	41.0	24.2	16.8	2.292	57.5
KS-2	50% kaolinite, 50% sand I	2.68	27.1	16.4	10.7	1.715	62.5
KS-3	25% kaolinite, 75% sand I	2.69	-	-	NP**	2.110	49.5
KS-4	25% kaolinite, 75% sand I	2.69	-	-	NP	1.782	49.9
S-1	100% sand I	2.71	-	-	NP	1.810	38.2
S-2	100% sand I	2.71	-	-	NP	1.647	38.6
I	100% illite	2.79	45.6	23.5	22.1	1.906	64.0
B	100% bentonite	2.75	388.0	32.5	355.5	1.479	82.2
OS-1	100% sand II	2.65	-	-	NP	0.750	40.3

using a least squares criterion. Table 6 contains the K_0 value for loading and the corresponding correlation coefficients for each of the samples.

During unloading the horizontal stress typically decreases slower than the vertical stress causing K_0 to increase with the OCR. This trend was also noted by previous investigators. Abdelhamid et al. (1) called this the concept of "preconsolidation". Obrciar (38) referred to it as the "prestressing" concept where a residual or locked-in stress system exists. This locked-in stress is illustrated by the cross-hatched area of the curve also shown in Fig. 22 (p. 84).

A few of the samples tested were subjected to more than one cycle of loading and unloading. Fig. 23 shows the plot of horizontal total stress versus vertical total stress for kaolinite sample K-3 which was subjected to three continuous cycles of loading and unloading. This curve illustrates how quickly the reloading path becomes parallel with the initial loading path for the second and third cycles. This general trend is typical for all samples subjected to reloading.

It must be emphasized that the porosity is different for each loading increment for a particular sample. This is illustrated by the log-log plots of vertical total stress versus porosity for kaolinite samples K-4 and K-3 in Figs. 24 and 25. Since the porosity changes considerably while K_0 remains constant for loading, this indicates that K_0 cannot be related to the porosity of the material.

Tables 7 through 25 in Appendix IV contain the experimental results for each sample.

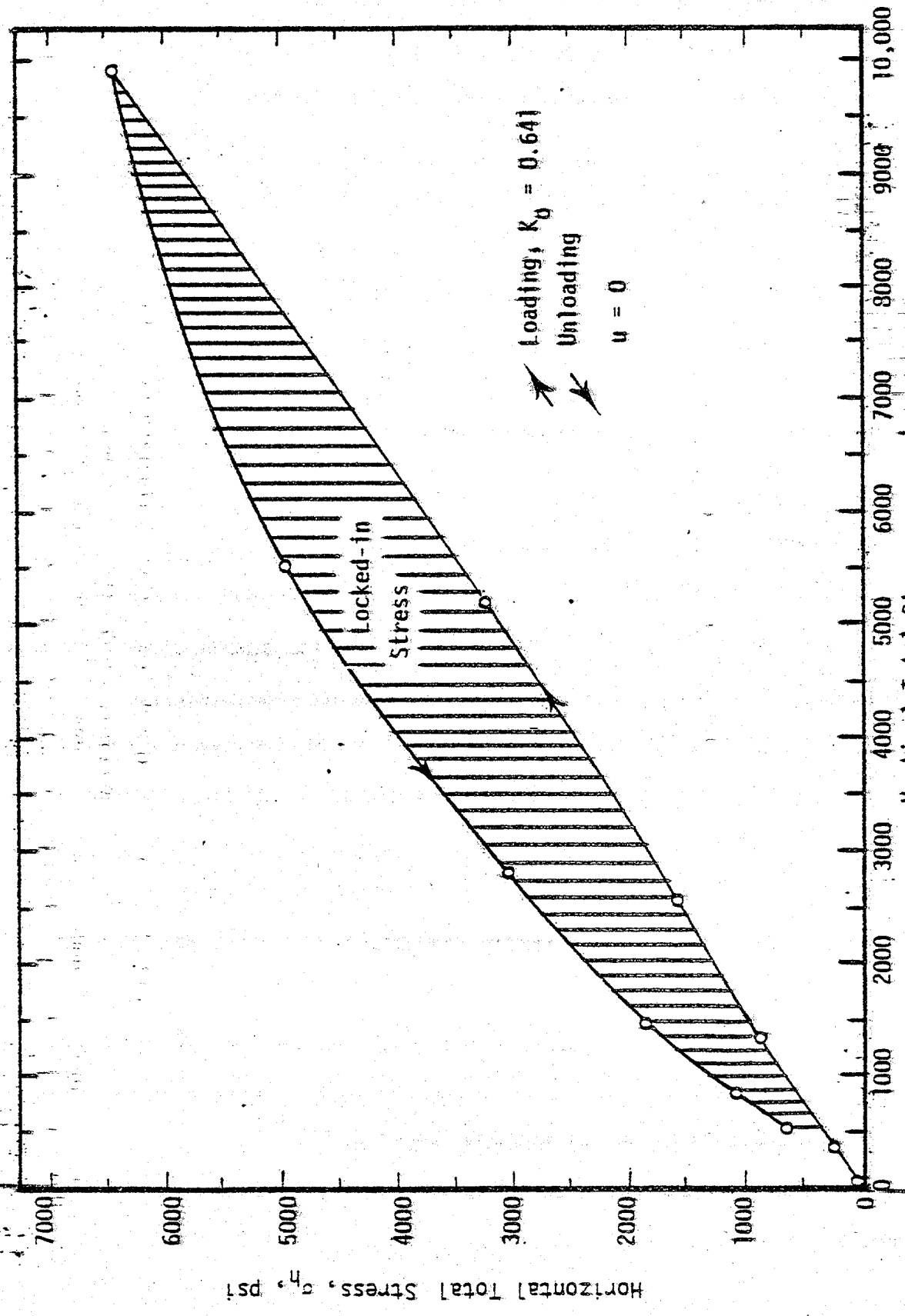


Fig. 22 - Stresses Measured After Consolidation of Sample K-4

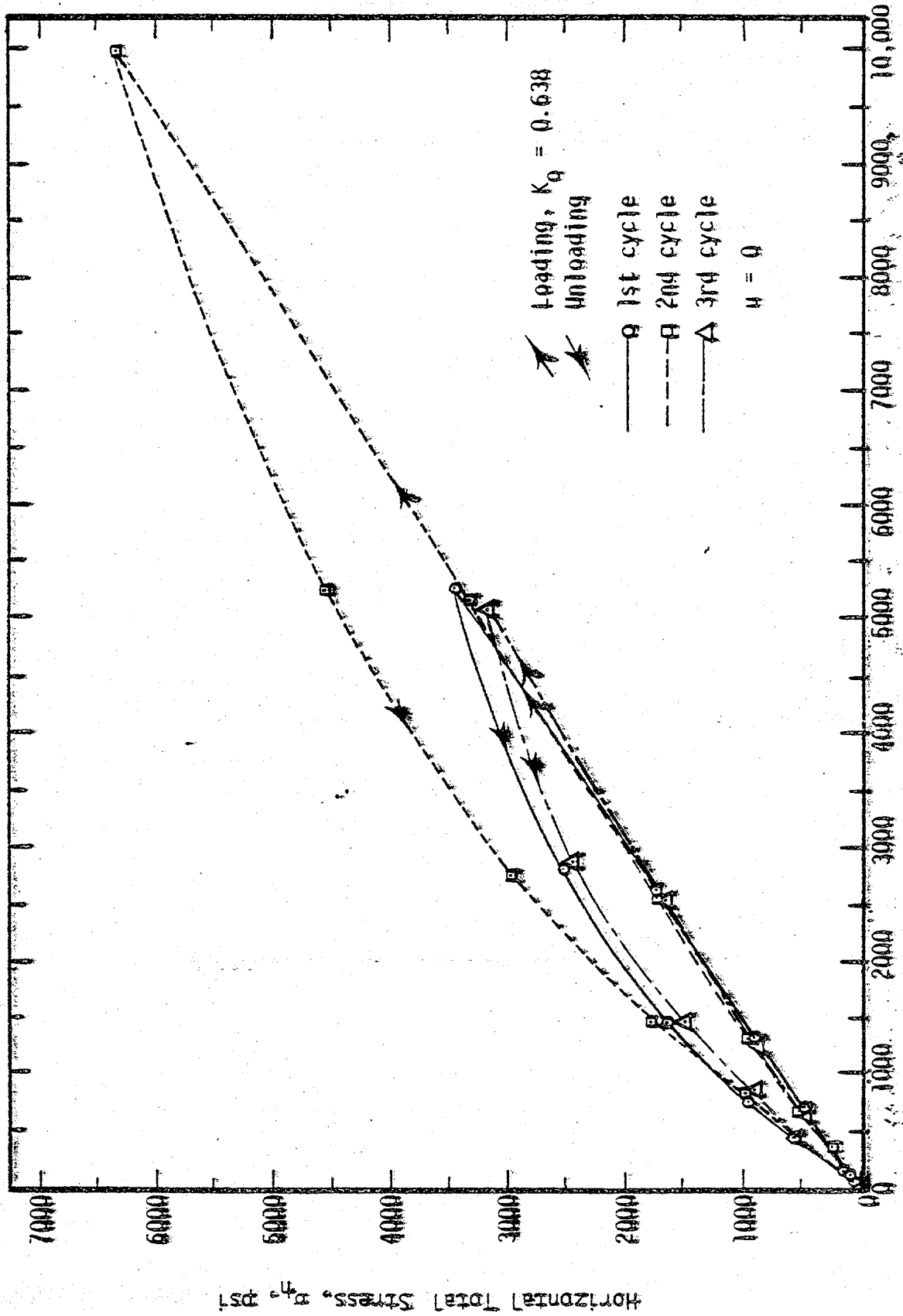


Fig. 23 - Stresses Measured After Consolidation of Sample K-3, Three Loading Cycles

Table 6 - Experimental K_0 Values for Loading

Sample No.	K_0 for Loading	Correlation Coefficient
K-1	.478	.99994
K-2	.616	.99882
K-3	.638	.99968
K-4	.641	.99958
K-5	.647	.99921
KS-1	.609	.99809
KS-2	.570	.99936
KS-3	.505	.99738
KS-4	.491	.99777
S-1	.533	.99470
S-2	.527	.99645
I	.553	.99893
B	.713	.99741
OS-1	.505	.99935
OS-2	.596	.99982
OS-3	.560	.99302
MC-I-U	.545	.99837
MC-I-R	.545	.99984
MC-II-U	.489	.99896

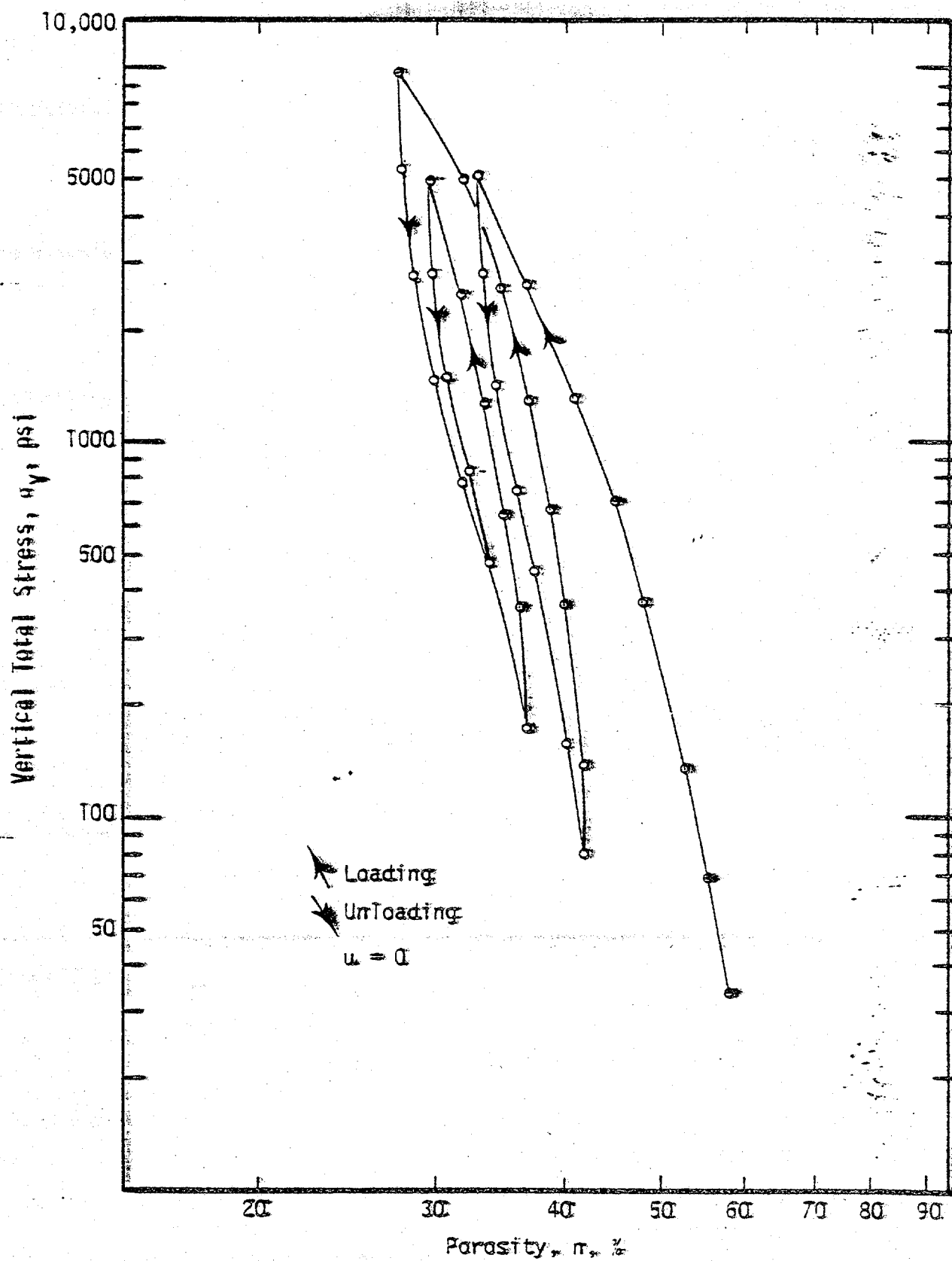


Fig. 25 - Compressibility of Sample K-3

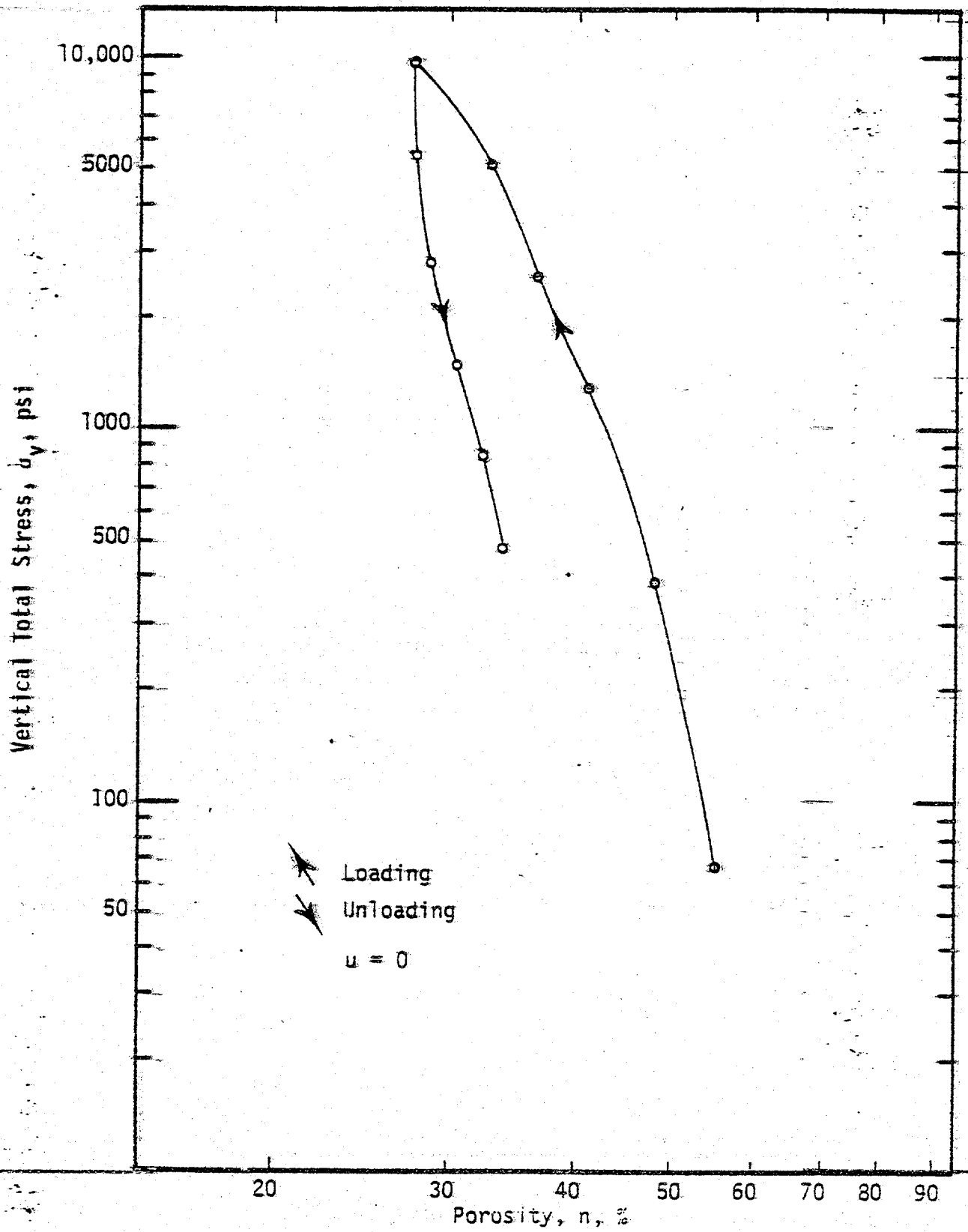


Fig. 24 - Compressibility of Sample K-4

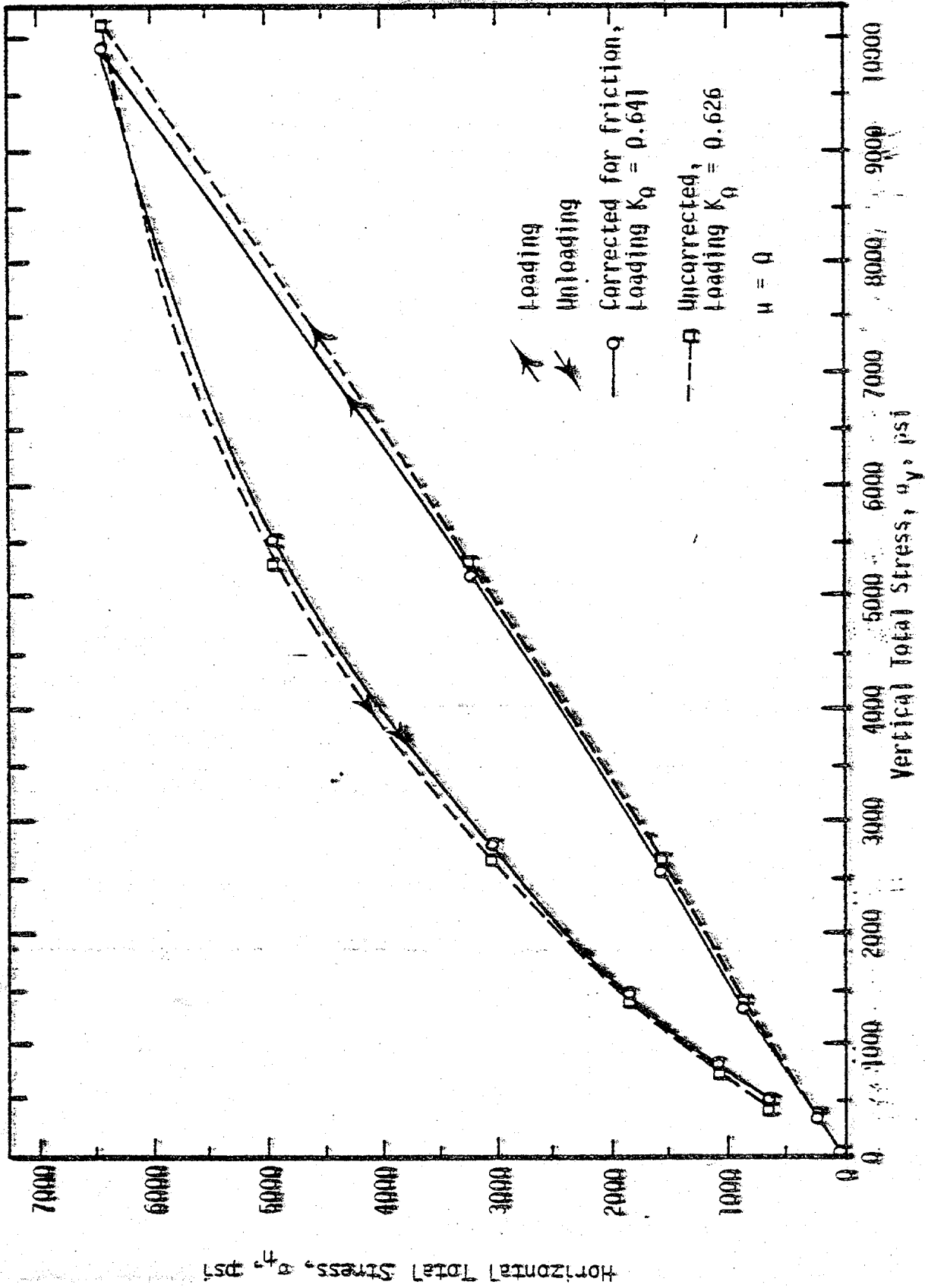


Fig. 26 - Correction of Vertical Effective Stress for Measured Friction, Sample K-4

Effects of Friction

Large volume changes of the sample during a test cause frictional stresses to develop along the rigid boundaries of the soil chamber. This friction occurs along the sidewalls as well as across the porous stones recessed into the top and bottom pistons.

To account for the sidewall friction a measure of the sidewall frictional force is made for each loading increment and the overburden stress is then corrected. For this correction twenty-five percent of the measured sidewall friction force is subtracted from the applied overburden load for loading increments and added to the applied overburden load for unloading increments. This calculation is described in more detail in Appendix III. Fig. 26 is a plot of horizontal total stress versus vertical total stress for kaolinite sample K-4 showing the corrected and uncorrected values of overburden stress. Only a slight difference can be observed between the two curves. However the K_0 values for loading are 0.641 and 0.626 for the corrected and uncorrected data, respectively, indicating that a significant difference does exist.

Because of the roughness of the porous stones on the top and bottom of the sample, the magnitude and significance of the friction across these surfaces is expected to be greater than that of the friction along the sidewall. An indication of this end friction is given by the development of conical sections of inhomogeneity in the ends of certain samples. These cones, known as slip cones, develop in uniaxial compression tests when the frictional stresses across the loading platens are high (41). A similar stress distribution is believed to exist in

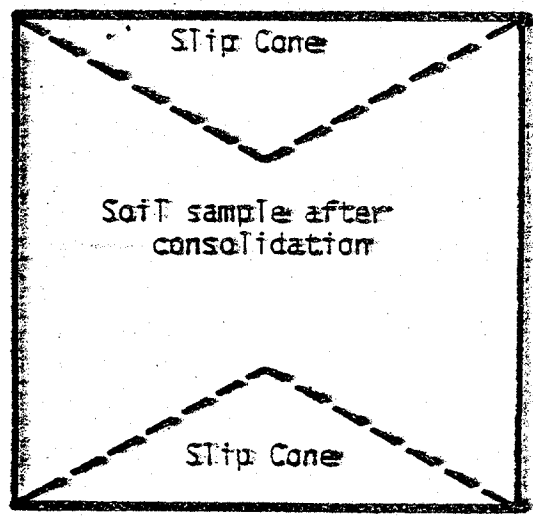
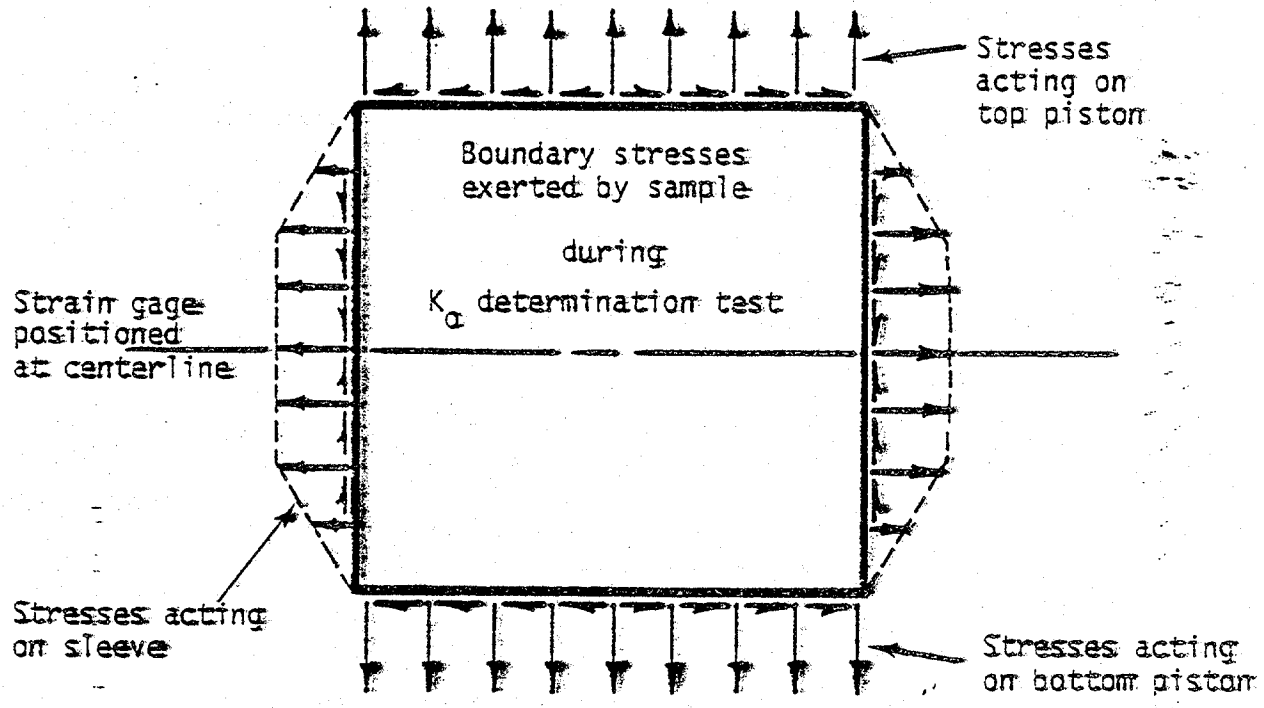


Fig. 27 - Slip Cones Expected Due to Frictional Stresses Across Top and Bottom Boundaries

the K_0 determination tests as illustrated in Fig. 27. Slip cones were observed upon removal of Ottawa sand sample OS-3 from the consolidometer as shown in Fig. 28. Similar observations were also made in clay samples.

For short samples the end friction may cause a reduction of horizontal stress measured at the centerline of the sample as illustrated in Fig. 29. A series of K_0 determination tests were performed on kaolinite samples with different initial sample heights to see what sample height is required to reduce the effects of end friction on the horizontal stress measurement. The results, plotted in Fig. 30, indicate that K_0 increases with the initial sample height and then begins to level off to a constant value of around 0.64 for initial sample heights greater than about one inch. This demonstrates that in order to avoid end friction effects, initial sample dimensions corresponding to a height-to-diameter ratio of at least 0.4 should be used.

After correcting for sidewall friction the range in values of K_0 for kaolinite samples with initial sample heights greater than one inch was from 0.638 to 0.647. Bishop (6) measured values of K_0 in low pressure triaxial tests in which the effects of boundary friction were virtually nonexistent. He found K_0 for kaolinite to range from 0.64 to 0.70. The equivalence of these results with those reported above demonstrates that accurate values of K_0 can be obtained in an apparatus with rigid confining boundaries as long as corrections are made for sidewall friction and the initial height-to-diameter ratio is greater than 0.4.

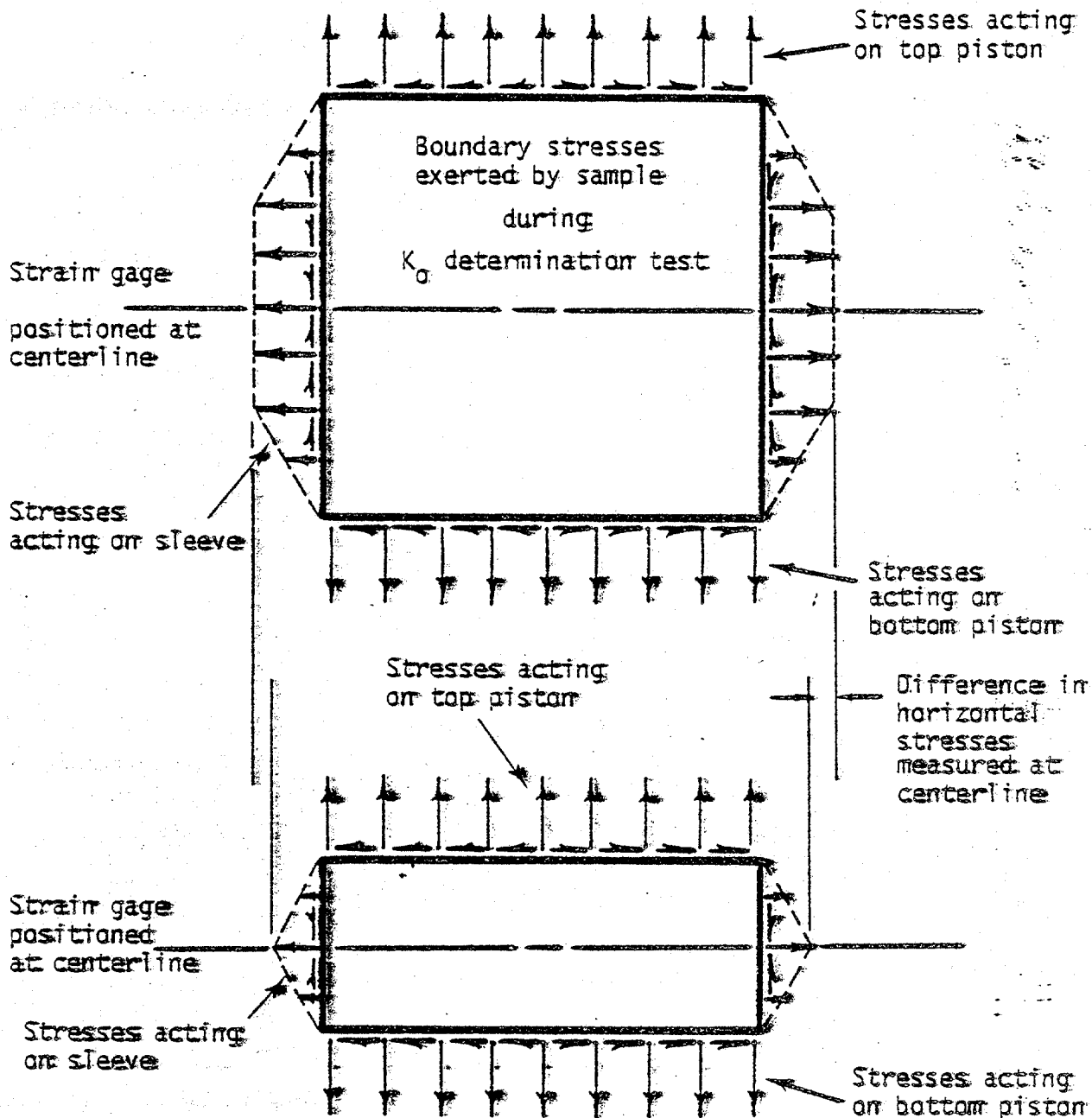


Fig. 29 - Comparison of Boundary Stresses Exerted by Tall and Short Samples.



Fig. 28 - Slip Cones Observed in Ottawa
Sand Sample OS-3

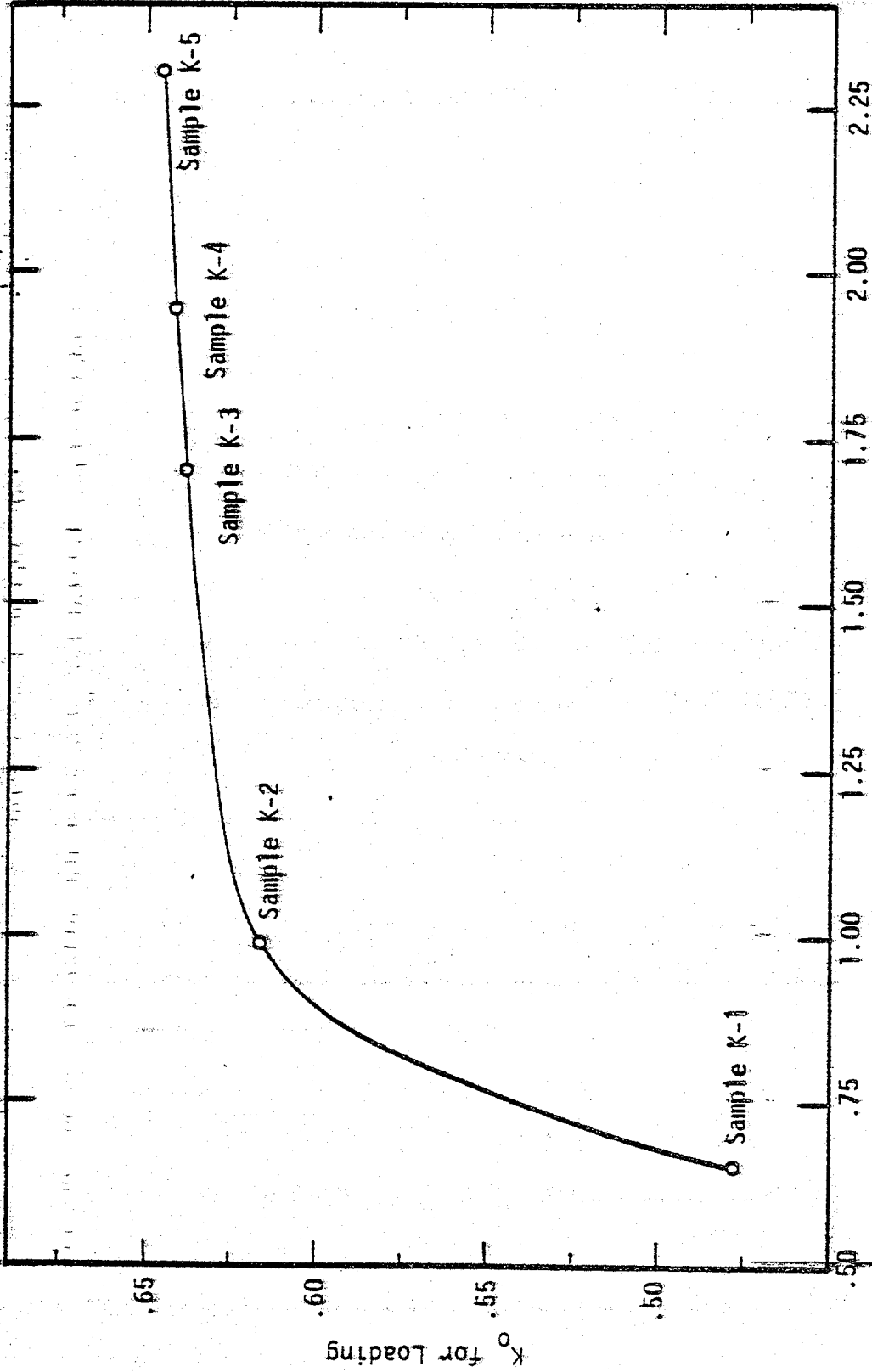
Relationships Involving K_0

In attempting to find a relationship between K_0 and some material parameter, a plot of K_0 versus plasticity index was made for the samples tested as shown in Fig. 31. It can readily be seen that no reasonable relationship between these two parameters can be deduced which reinforces the findings of Bishop (6).

Anderson et al. (5) inferred that K_0 might be a function of the percent shale in the material. Percent shale is similar to the percent of fine material (i.e. material passing a #200 sieve) in a soil. To examine this possibility several samples containing different percentages by weight of fine material were tested. The results are shown in a plot of K_0 versus percent fines in Fig. 32. Although the correlation is not good, the line drawn through the data shows a tendency for K_0 to increase with the percent fines.

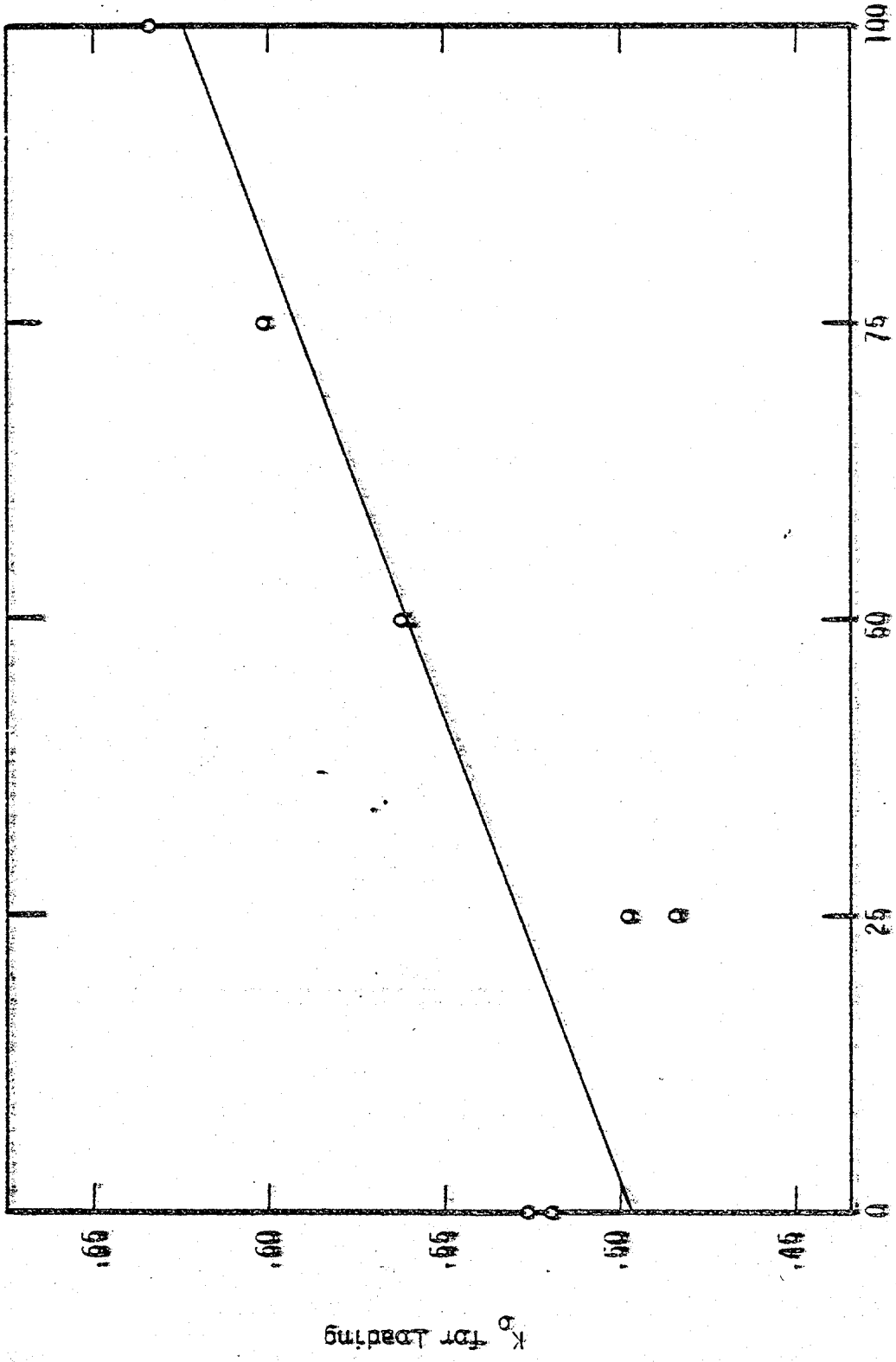
It is also desirable to describe some function involving the K_0 data for unloading and reloading. To do this a relationship between K_0 and the OCR was analyzed as previous investigators have done. Schmidt (48) made log-log plots of K_0 versus OCR for several sets of data and showed a linear tendency of the data. When these plots were made for the data obtained from this research, considerable curvature was observed, as illustrated in the plot for kaolinite sample K-4 in Fig. 33. This curvature seems to reinforce a statement by Schmidt (48) that a straight line fit may show considerable deviation at high levels of the OCR. This same general curving trend was observed for all samples subjected to any unloading increments.

Fig. 34 is another log-log plot of K_0 versus OCR for illite



Initial Sample Height, in.

Fig. 30 - Observed Relationship Between K_0 and Initial Sample Height for Kaolinite Samples



Material Passing No. 200 Sieve, %

Fig. 32 - Effects of Percent Fines on K_0 for Kaolinite-Sand Mixtures

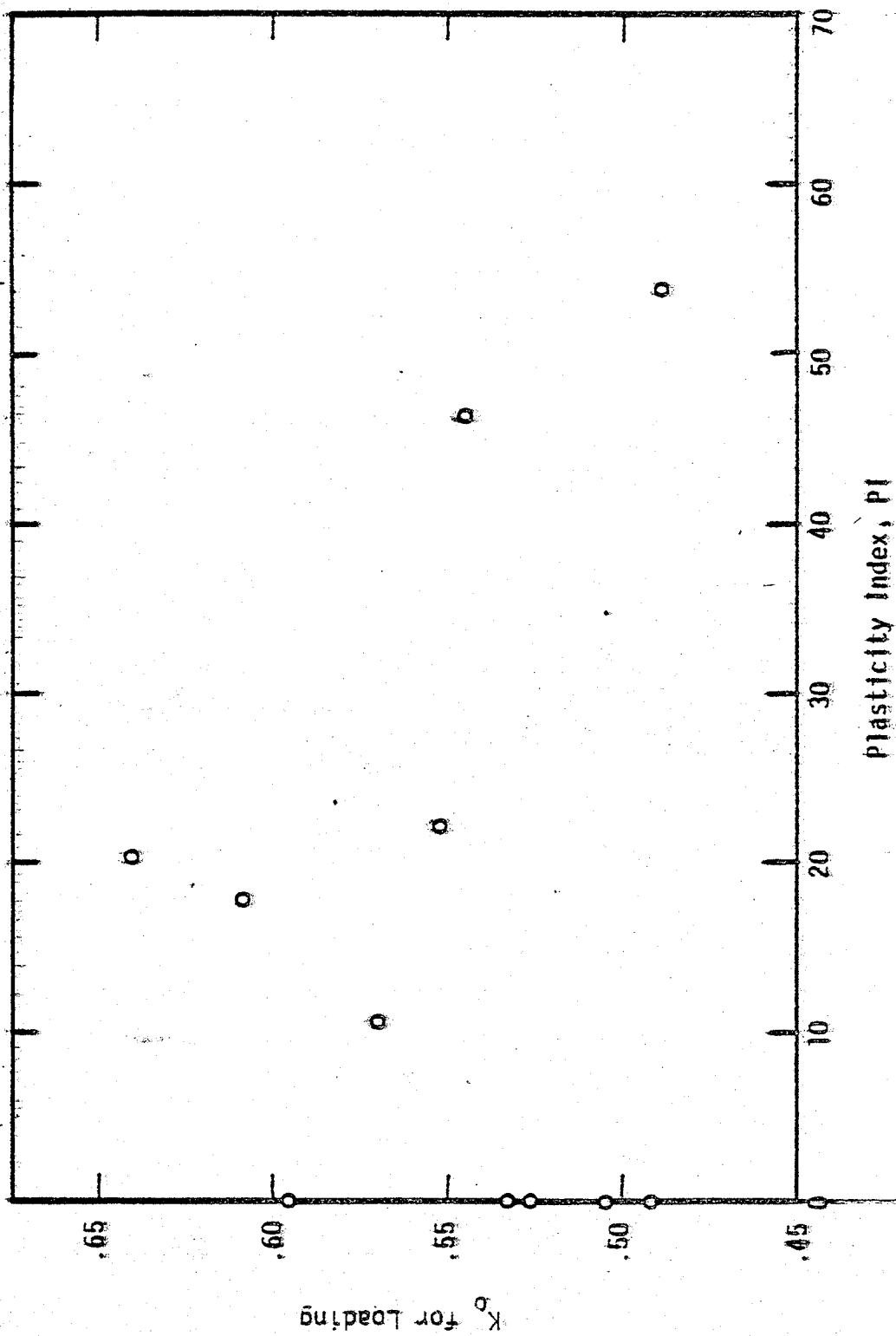


Fig. 31 - Experimental Results Showing No Relationship Between K_0 and PI

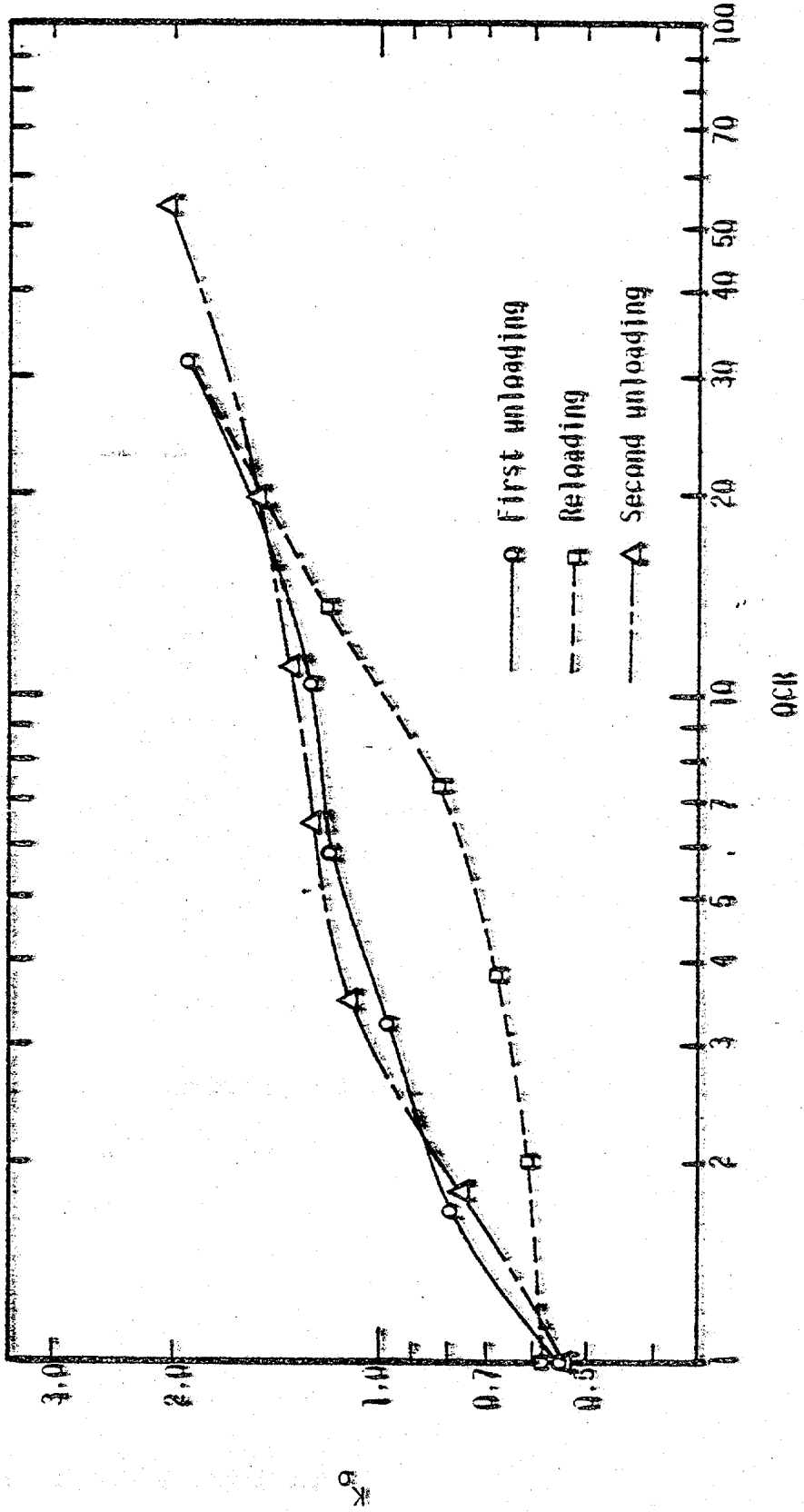


Fig. 34 - Relationship Between K_p and OCR for Sample 1

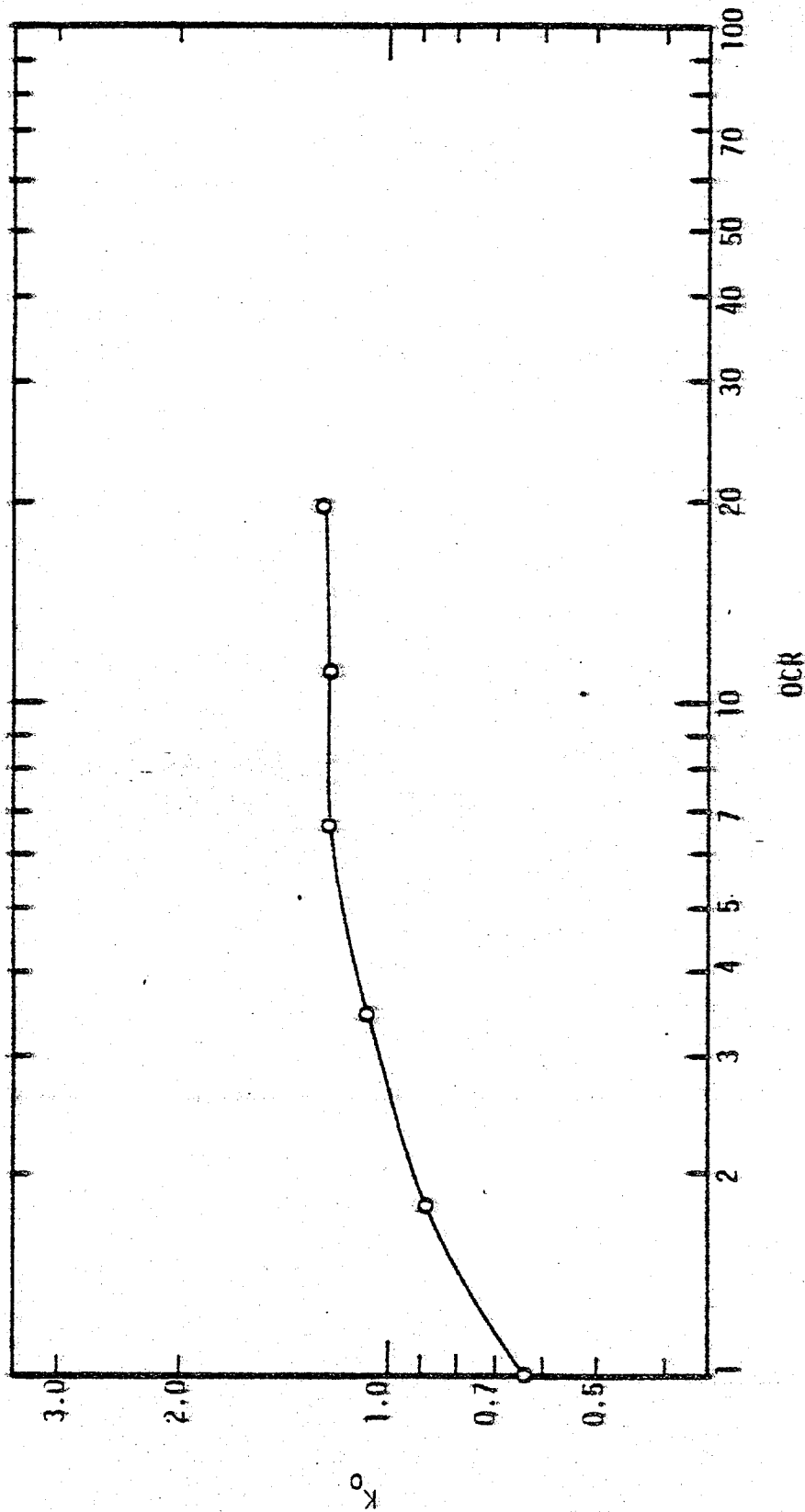


Fig. 33 - Relationship Between K_0 and OCR for Sample K-4

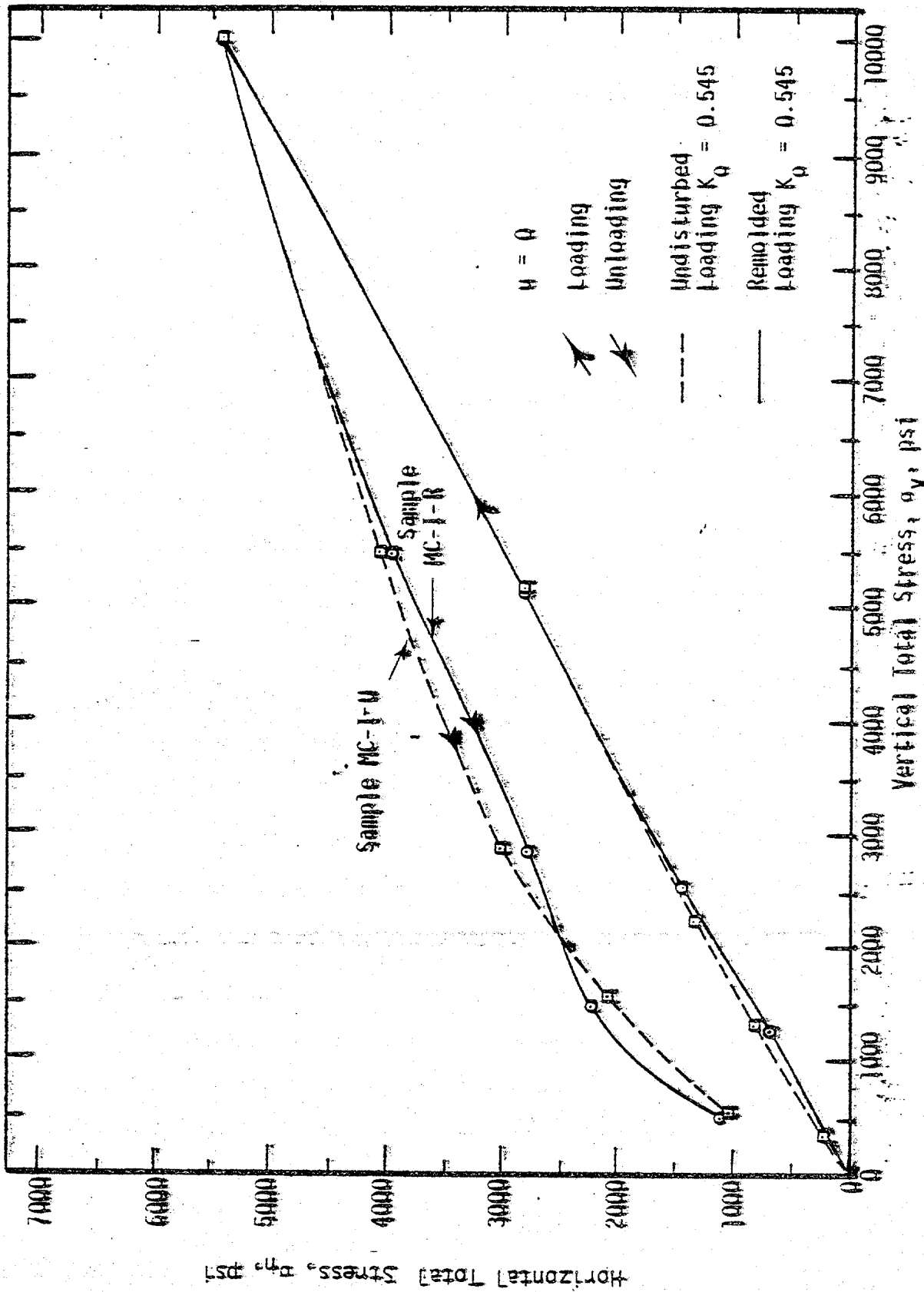
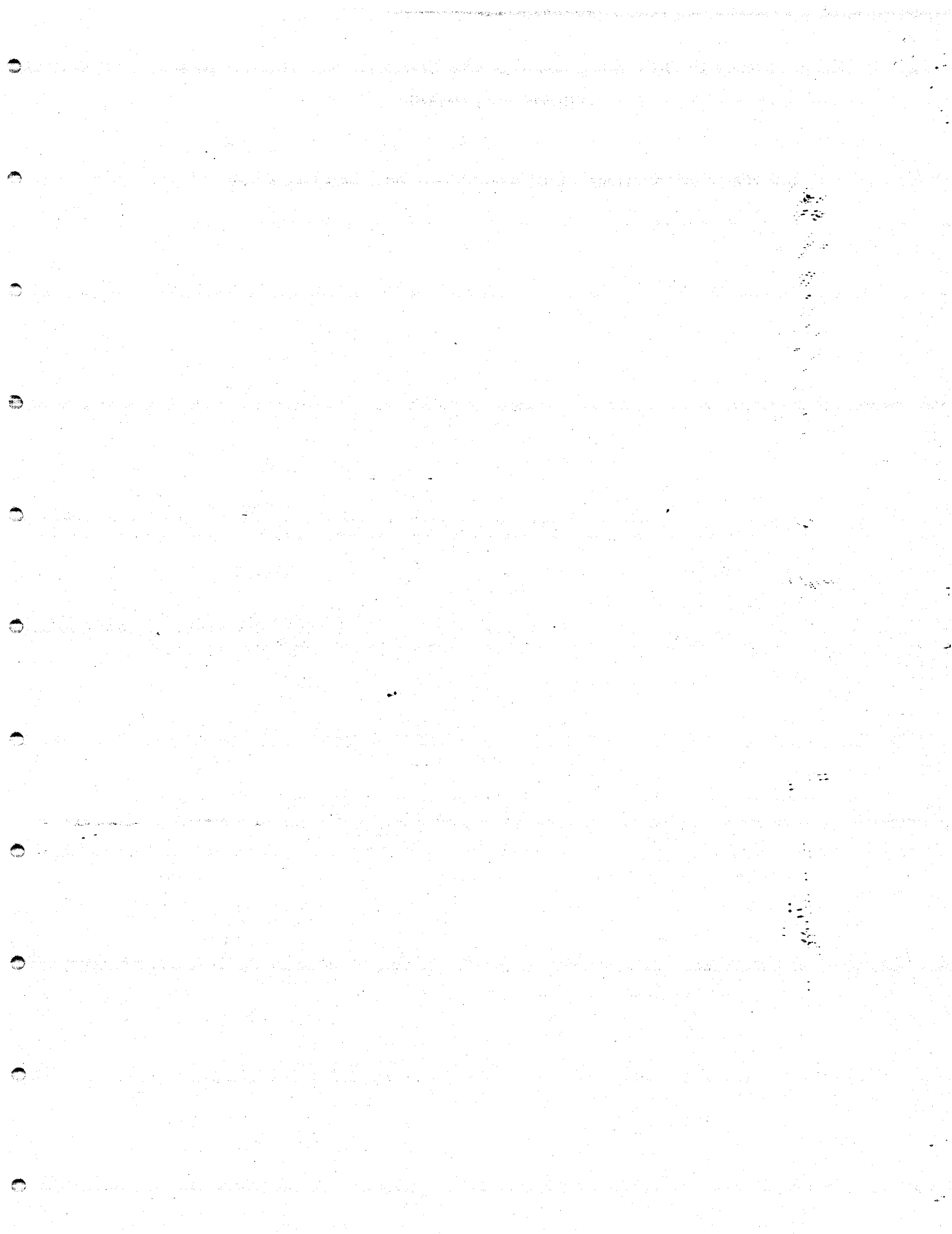


Fig. 35 - Stresses Measured After Consolidation of Undisturbed and Remolded Marine Clay

sample I. This test included two continuous cycles of loading and unloading. In this figure the same curvature for initial loading is observed as before; however, for the reloading increments the curvature is in the opposite direction. For the second cycle of unloading the path follows very closely along that of the first unloading cycle. This tendency is observed in other tests consisting of more than one loading and unloading cycle. Regardless of the number of loading and unloading cycles, the same general cyclic path is followed. The hysteresis shown in these plots indicates that the straight line approximation proposed by Schmidt (48) may be considerably in error even at low levels of the OCR especially for reloading. In fact, in order to accurately predict K_0 for overconsolidated soils, in addition to the OCR, it must be known whether the soil is being unloaded or reloaded.

It is also interesting to compare the behavior of K_0 for an undisturbed sample and a remolded sample. This was done by running two separate K_0 determination tests on a natural marine sediment from the Angola Basin off the West Coast of Africa. For the first test a sample (MC-I-U) was trimmed directly from a sample core. Although some degree of disturbance is experienced during the sampling and trimming procedure, the sample is still in a relatively undisturbed state. After the test was completed this sample was removed and completely remolded to a slurry state and then used for the sample (MC-I-R) in the second test. These two tests show K_0 behavior for a particular soil in a relatively undisturbed state and a completely remolded state. The plot of horizontal total stress versus vertical total stress for both of these tests are shown in Fig. 35. It is



easily seen that the results are almost identical for both tests. In fact the loading values of K_0 are identically equal to 0.545 for both tests indicating that disturbance of the material has no effect on the behavior of K_0 .

Results from the Measurement of A_w

It was desired to determine the value of A_w as used in the matrix stress concept. To do this two tests were run in which total horizontal stresses were measured with various levels of induced pore pressure for each loading increment as discussed in Ch. VI. The first test was performed on Ottawa sand (sample OS-3) and the second on a natural clay (sample MC-II-U) from the Angola Basin off the West Coast of Africa. Fig. 36 illustrates how the total horizontal stress increased linearly with the pore pressure for the final loading increment of the Ottawa sand sample. A comparison of this line with that predicted by the effective stress concept shows large deviation. These same trends were exhibited for every loading increment of both the clay and the sand samples. The results of these two tests are tabulated in Appendix V.

This deviation implies that the consideration of the areas on which the pore pressure acts is of significant importance. According to the matrix stress concept

$$\frac{\Delta\sigma_{\pi}}{\Delta u} = A_w \dots \dots \dots (57)$$

as pointed out in Ch. III. This ratio is also equal to the slope of the line defined by the data as indicated in Fig. 36 and is

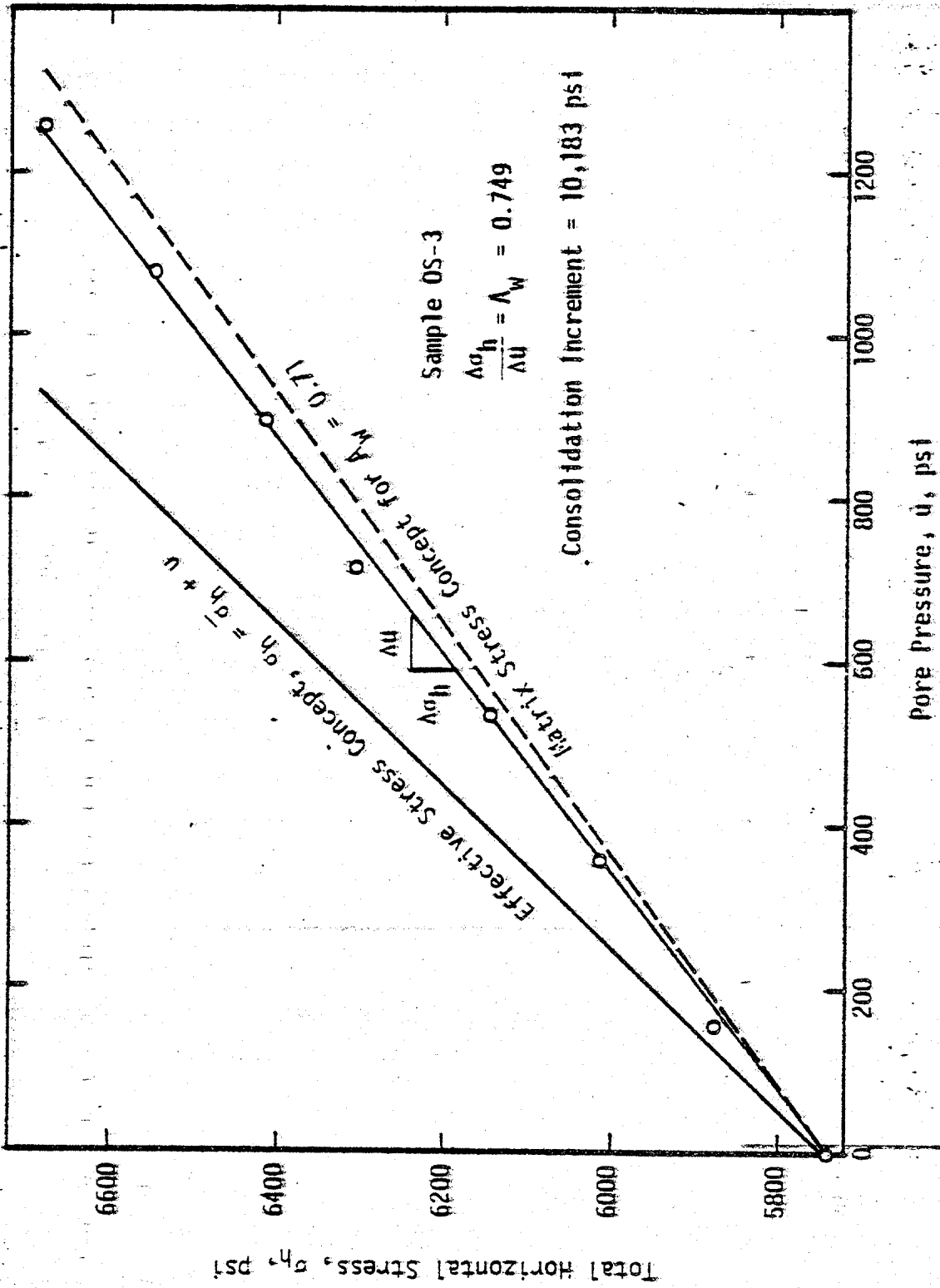


Fig. 36 Typical Results of Total Horizontal Stress Measurement Test with Pore Pressures Induced

0.749 for that loading increment. This means that the pore pressure acts on only 74.9% of the circumferential area around the sample. The remaining area consists of contact areas between soil grains and the confining sleeve. The water areas, A_w , for each increment are plotted versus porosity for both samples in Fig. 37. Surprisingly no relationship is evident between the water area and porosity for either soil.

These two tests plainly demonstrate the importance of the area involved in describing stresses within a two phase medium. Furthermore, it shows that the effective stress concept can be very seriously in error in predicting total stresses where pore pressures may be quite high.

Due to a lack of knowledge concerning the exact magnitudes of the areas involved in a porous medium an approximation is necessary. From the data of both tests it can be seen that the average water area ratio is 0.77. Therefore, as opposed to the effective stress concept, a more accurate approximation of total stress might be obtained by using the matrix stress concept with $A_w = 0.77$ as follows:

$$\sigma = \sigma' + 0.77 u \dots \dots \dots (58)$$

This assumes that A_w is constant in all directions. A comparison of this approximation with the data in Fig. 36 (p. 105) shows much less deviation than the effective stress concept.

Application of Laboratory Derived K_0 Values to Drilling Operations

In order to aid in continuous predictions of the hydrofracture pressure, it is desirable to predict predrilled stresses during drilling.

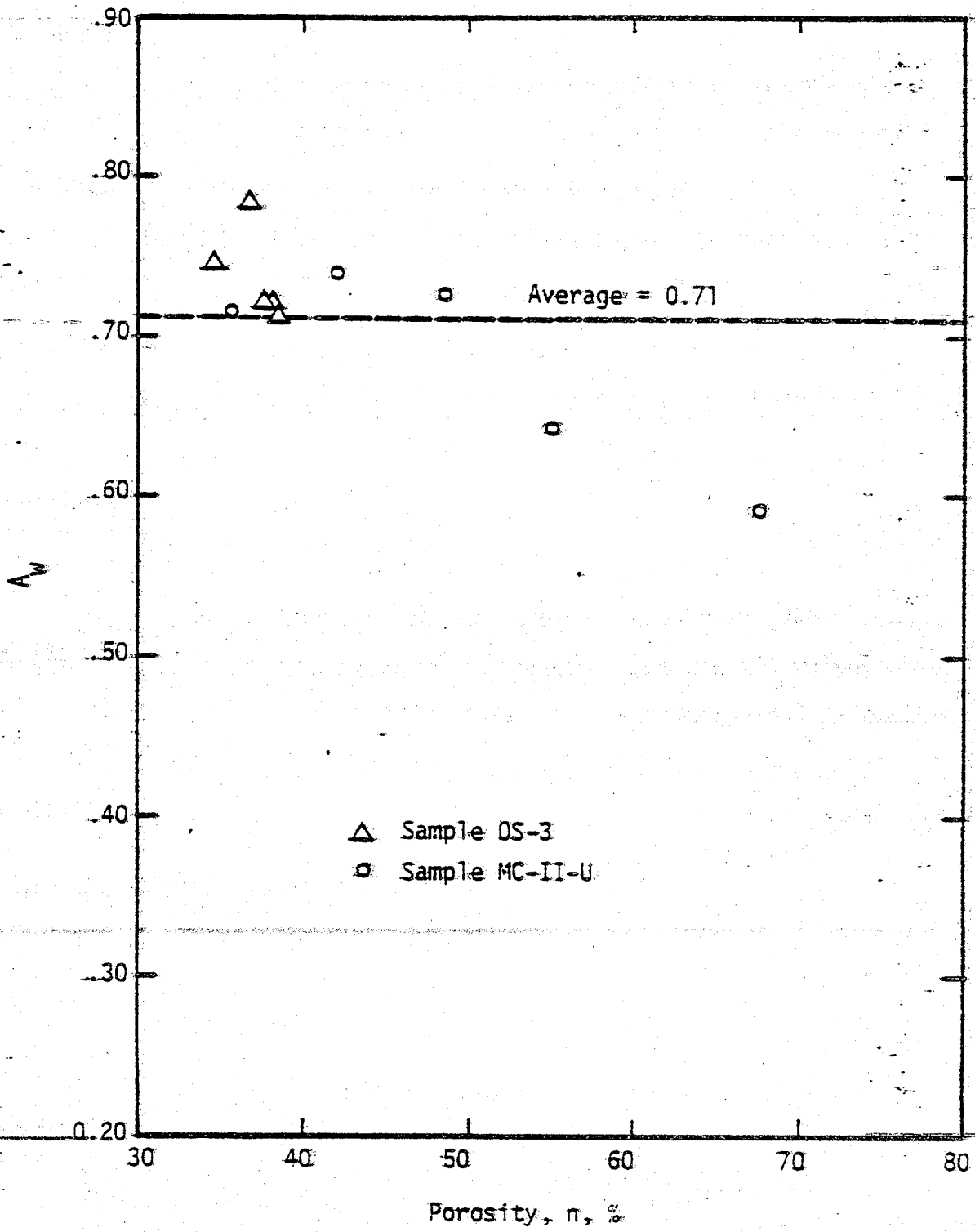


Fig. 37 - Variation of Water Area with Porosity as Measured for Two Soils

One way in which this could be done is by using a laboratory derived value of K_0 for the material being encountered. The material type contained in the formation can be determined from cuttings coming out of the hole.

Certain limitations exist, however, when using laboratory derived K_0 values to estimate in situ stresses at great depth. To do this the geostatic condition must be assumed. This condition is met only in the cases shown in Fig. 2 (p. 11).

Since no unique relationships involving K_0 and material parameters have been found, as pointed out in this thesis, K_0 values must be previously catalogued in the laboratory for the specific material contained in the formation. The overburden stress is easily determined, as previously discussed. However the OCR is almost impossible to predict. Furthermore, there is no way to determine whether the formation is being unloaded or reloaded which, in itself, has a great influence on K_0 .

Because of the uncertainty concerning the stress history, all one could do would be to assume the formation to be normally consolidated and use the constant loading value of K_0 for that particular material. Since this loading value is the minimum value of K_0 , the calculated horizontal stress would be a minimum which would thereby yield a minimum hydrofracture pressure prediction. This minimum value is of greatest concern during drilling in order to prevent unintentional hydrofracture.

In the case of intentional hydrofracture, such as in stimulation efforts, the maximum value of K_0 , yielding the maximum predicted hydrofracture pressure, might be desired as an aid in designing fracture

treatments. This maximum value could also be approximated from data generated in the laboratory for unloading cycles of K_0 measurements.

CHAPTER VIII

CONCLUSIONS AND RECOMMENDATIONS

Six modes of failure around a borehole are possible during drilling, depending upon the relative magnitudes and directions of the principal stresses. These six failure modes are described in Table 1 (p. 33). Three of these modes describe cases of hydrofracture and the other three describe cases of sloughing failure. Using equilibrium and the Mohr-Coulomb failure criterion, equations describing borehole pressures necessary for incipient failure for each of these six modes are formulated as listed in Table 3 (p. 41). The formulation is for a homogeneous, isotropic material under geostatic conditions, and the borehole fluid is assumed to be nonpenetrating. Predicted hydrofracture pressure profiles using these equations show good correlation to an average of actual hydrofracture gradients measured in the field.

It is shown that accurate predictions of K_{σ} are essential to hydrofracture pressure predictions during drilling. To analyze K_{σ} and lateral stress behavior of several materials under conditions which may exist up to 10,000 feet below the earth's surface, a high pressure laboratory consolidation system was developed simulating the process of progressive burial and massive erosion of sediments. This was done in an attempt to find ways of estimating predicted stress states during uninterrupted drilling operations so

as to enable continuous prediction of hydrofracture pressure.

Based on the results obtained it is concluded that:

1. Accurate laboratory determinations of K_0 can be made in a rigid wall apparatus if corrections are made for boundary friction.

2. K_0 is dependent upon material type and stress history.

3. K_0 is constant for loading up to magnitudes of vertical stress of 10,000 psi. K_0 increases upon unloading due to locked-in stresses. It decreases for reloading until it reaches the loading value of K_0 .

4. K_0 does not appear to be uniquely related to porosity or the plasticity index. K_0 only vaguely appears to be related to ϕ and percent fines.

5. K_0 for overconsolidated soils depends not only upon the OCR but also on whether the soil is being unloaded or reloaded.

6. K_0 behaves exactly the same for undisturbed and remolded soils.

7. The average area of water, A_w , for the measurements made was 0.71. Therefore the matrix stress concept, written as,

$$\sigma = \sigma' + 0.71 u$$

should give a more accurate approximation of total stresses than the effective stress concept, especially where the pore pressure is high.

8. In using Tab derived K_0 values for predicted horizontal stress predictions, it must be assumed that the formation is normally consolidated and no tectonic stresses exist. This approach yields the minimum hydrofracture pressure expected.

9. By using K_0 values, free-field horizontal stresses can only be predicted during drilling if laboratory derived K_0 values have been previously catalogued for the particular material contained in a given formation.

Additional research of this type is needed to catalogue K_0 values for various materials encountered during drilling. It would be interesting to incorporate within the experimental system a way of controlling temperature so that the thermal gradient could be simulated. This would enable an analysis of the effects of temperature on K_0 . Additional research is needed in determining grain-to-grain contact areas in porous media so that more accurate and realistic estimations of total stresses can be made using the matrix stress concept.

APPENDIX I

REFERENCES

REFERENCES

1. Abdelhamid, M. S., and Krizek, R. J., "At-Rest Lateral Earth Pressure of a Consolidating Clay," Journal of the Geotechnical Engineering Division, ASCE, Vol. 102, No. GT7, Proc. Paper 12240, July 1976, pp. 721-738.
2. Akagi, T., "Effect of Desiccation and Ring Friction on the Apparent Preconsolidation Load of Clay," thesis presented to the University of Illinois, at Urbana, Ill., in 1960, in partial fulfillment of the requirements for the degree of Master of Science.
3. Athaus, V. E., "A New Model for Fracture Gradient," Journal of Canadian Petroleum Technology, Vol. 16, No. 2, April 1977, pp. 98-108.
4. Anderson, E. M., The Dynamics of Faulting and Dyke Formation with Application to Britain, Oliver and Boyd, London, England, 1951.
5. Anderson, R. A., Ingram, D. S., and Zanier, A. M., "Determining Fracture Pressure Gradients from Well Logs," Journal of Petroleum Technology, Vol. 25, No. 11, November 1973, pp. 1259-1267.
6. Bishop, A. W., "Test Requirements for Measuring the Coefficient of Earth Pressure at Rest," presented at the September 1958 Conference on Earth Pressure Problems, held at Brussels, Belgium.
7. Bishop, A. W., "The Principle of Effective Stress," Publication No. 32 of the Norwegian Geotechnical Institute, 1960.
8. Bishop, A. W., and Henkel, D. J., The Measurement of Soil Properties in the Triaxial Test, 2nd ed., Edward Arnold Publishers Ltd., London, England, 1962.
9. Bjerrum, L., et al., "Hydraulic Fracturing in Field Permeability Testing," Geotechnique, Vol. 22, No. 2, June 1972, pp. 319-332.
10. Brooker, E. W., and Ireland, H. O., "Earth Pressures at Rest Related to Stress History," Canadian Geotechnical Journal, Vol. 2, No. 1, February 1965, pp. 1-15.
11. Cebertowicz, R., and Wedzinski, W., "Relation Entre Les Tensions Internes Horizontales Et Verticales Du Sol," presented at the September 1958 Conference on Earth Pressure Problems, held at Brussels, Belgium.
12. Clark, J. B., "A Hydraulic Process for Increasing the Productivity of Wells," Petroleum Transactions of AIME, Vol. 186, 1949, pp. 1-8.

13. Davisson, M. T., "Static and Dynamic Behavior of a Playa Silt in One-Dimensional Compression," Report No. AFWL-RTD-TDR-63-3078, Soil Mechanics and Foundation Division, Department of Civil Engineering, University of Illinois, at Urbana, Ill., 1963.
14. Eaton, B. A., "Fracture Gradient Prediction and Its Application in Oilfield Operations," Journal of Petroleum Technology, Vol. 21, No. 10, October 1969, pp. 1353-1360.
15. Eaton, B. A., "How to Drill Offshore with Maximum Control," World Oil, Vol. 171, No. 5, October 1970, pp. 73-77.
16. Fraser, C. D., and Pettitt, B. E., "Results of a Field Test to Determine the Type and Orientation of a Hydraulically Induced Formation Fracture," Journal of Petroleum Technology, Vol. 14, No. 5, May 1962, pp. 463-466.
17. Geertsma, J., "Problems of Rock Mechanics in Petroleum Production Engineering," Proceedings of the First International Symposium on Rock Mechanics, held at Lisbon, Portugal, 1966, pp. 585.
18. Gold, T., and Soter, S., "The Deep-Earth-Gas Hypothesis," Scientific American, Vol. 242, No. 6, June 1980, pp. 154-161.
19. Gretener, P. E., "Can the State of Stress be Determined from Hydraulic Fracturing Data?," Journal of Geophysical Research, Vol. 70, No. 24, December 1965, pp. 6205-6212.
20. Haimson, B., and Fairhurst, C., "Initiation and Extension of Hydraulic Fractures in Rocks," Society of Petroleum Engineers Journal, Vol. 7, No. 3, September 1967, pp. 310-318.
21. Haimson, B., "Hydraulic Fracturing in Porous and Nonporous Rock and Its Potential for Determining In Situ Stresses at Great Depth," thesis presented to the University of Minnesota, in 1968, in partial fulfillment of the requirements for the degree of Doctor of Philosophy.
22. Hendron, A. J., "The Behavior of Sand in One-Dimensional Compression," thesis presented to the University of Illinois, at Urbana, Ill., in 1963, in partial fulfillment of the requirements for the degree of Doctor of Philosophy.
23. Howard, G. C., and Fast, C. R., Hydraulic Fracturing, Monograph Vol. 2, Society of Petroleum Engineers of AIME, Dallas, Texas, 1970.
24. Hubbert, M. K., and Willis, D. G., "Mechanics of Hydraulic Fracturing," Petroleum Transactions of AIME, Vol. 210, 1957, pp. 153-168.

25. Huck, P. J., et al., "Determination of the In Situ State of Stress in Soil Masses," Report No. FHWA-RD-74-68, Federal Highway Administration Offices of Research and Development, Washington, D.C., September 1974.
26. Jakubov, A. A., and Ati-zade, A. A., "Mud Volcanoes of the Azerbaijan, SSR," published by the Academy of Sciences of the Azerbaijan SSR, no date.
27. Jaky, J., "Pressure in Silos," Proceedings of the Second International Conference on Soil Mechanics and Foundation Engineering, held at Rotterdam, Netherlands, 1948, pp. 103-107.
28. Jumikis, A. R., Rock Mechanics, 1st ed., Trans Tech Publications, Rockport, Maryland, 1979, pp. 221-237.
29. Kehrte, R. O., "The Determination of Tectonic Stresses Through Analysis of Hydraulic Well Fracturing," Journal of Geophysical Research, Vol. 69, No. 2, January 1964, pp. 259-273.
30. Kirkpatrick, W. M., Discussion of "Determination of Lateral Pressures Associated with Consolidation of Granular Soils," Highway Research Record, No. 284, 1969, pp. 23-25.
31. Lambe, T. W., and Whitman, R. V., Soil Mechanics, John Wiley and Sons, Inc., New York, N. Y., 1969.
32. LeTiavsky, S., "Uplift Pressure In and Beneath Dams," Transactions of the American Society of Civil Engineers, Vol. 112, Paper No. 2304, 1947, pp. 443-487.
33. MacPherson, L. A., and Berry, L. N., "Prediction of Fracture Gradients from Log Derived Elastic Moduli," Log Analyst, Vol. 3, No. 5, September 1972, pp. 12-19.
34. Matthews, W. R., and Kelly, J., "How to Predict Formation Pressure and Fracture Gradient," Oil and Gas Journal, Vol. 65, No. 8, February 1967, pp. 92-106.
35. Miller, J. W., "The Thermal Conductivity of Sediments as a Function of Porosity," thesis presented to Texas A&M University, in 1979, in partial fulfillment of the requirements for the degree of Master of Science.
36. Moore, C. A., "Effect of Mica on K_0 Compressibility of Two Soils," Journal of the Soil Mechanics and Foundations Division, ASCE, Vol. 97, No. SM9, Proc. Paper 8401, September 1971, pp. 1275-1291.
37. Morgenstern, N., "A Relationship Between Hydraulic Fracture Pressures and Tectonic Stresses," Geofisica Pura e Applicata, Vol. 52, No. 2, May 1962, pp. 104-115.

38. Obrcian, V., "Determination of Lateral Pressures Associated with Consolidation of Granular Soils," Highway Research Record, No. 284, 1969, pp. 13-22.
39. Ode, H., "Mechanical Analysis of the Dike Pattern of the Spanish Peaks Area, Colorado," Bulletin of the Geological Society of America, Vol. 68, No. 5, May 1957, pp. 567-576.
40. Parker, T. J., and McDowell, A. N., "Model Studies of Salt-Dome Tectonics," Bulletin of the American Association of Petroleum Geologists, Vol. 39, No. 12, December 1955, pp. 2384-2470.
41. Polakowski, N. H., and Ripling, E. J., "Properties Under Compressive Loads," Strength and Structure of Engineering Materials, Prentice-Hall, Inc., Englewood Cliffs, N. J., 1966, pp. 295-316.
42. Powley, D., Senior Scientist, Amoco Research Labs., Tulsa, Oklahoma, personal communication, October 1979.
43. Randolph, P. L., "Massive Stimulation Effort May Double U. S. Gas Supply," World Oil, Vol. 179, No. 6, November 1974, pp. 81-84.
44. Riley, F. S., "Liquid-level Tiltmeter Measures Uplift Produced by Hydraulic Fracturing," United States Geological Survey Professional Paper No. 424-B, 1961, pp. 317-319.
45. Scheidegger, A. E., "On the Connection Between Tectonic Stresses and Well Fracturing Data," Geofisica Pura E Applicata, Vol. 46, No. 2, May 1960, pp. 66-76.
46. Scheidegger, A. E., "Stresses in the Earth's Crust as Determined from Hydraulic Fracturing Data," Geologie und Bauwesen, Vol. 27, No. 2, April 1962, pp. 45-53.
47. Scheidegger, A. E., The Physics of Flow Through Porous Media, 3rd ed., University of Toronto Press, Great Britain, 1974, pp. 24-25.
48. Schmidt, B., "Lateral Stresses in Uniaxial Strain," Bulletin of the Danish Geotechnical Institute, No. 23, 1967, pp. 4-13.
49. Sherif, M. A., and Strazer, R. J., "Soil Parameters for Design of Mt. Baker Ridge Tunnel in Seattle," Journal of the Soil Mechanics and Foundations Division, ASCE, Vol. 99, No. SMI, Proc. Paper 9511, January 1973, pp. 111-122.
50. Simonds, A. W., "Cement and Clay Grouting of Foundations: Present Status of Pressure Grouting Foundations," Journal of the Soil Mechanics and Foundations Divisions, ASCE, Vol. 84, No. SMI,

- Proc. Paper 1544, February 1958, pp. 1-11.
51. Singh, R., Henkel, D. J., and Sangrey, D. A., "Shear and K_0 Swelling of Overconsolidated Clay," Proceedings of the Eighth International Conference on Soil Mechanics and Foundation Engineering, held at Moscow, U.S.S.R., Vol. 1, No. 2, 1973, pp. 367-376.
 52. Skempton, A. W., "Effective Stress in Soils, Concrete and Rocks," taken from Pore Pressure and Suction in Soils, Butterworths, London, 1961.
 53. Taylor, D. B., and Smith, T. K., "Improving Fracture Gradients Estimates in Offshore Drilling," Oil and Gas Journal, Vol. 68, No. 15, April 1970, pp. 67-72.
 54. Terzaghi, K., "Simple Tests Determine Hydrostatic Uplift," Engineering News-Record, Vol. 116, No. 25, June 18, 1936, pp. 872-875.
 55. Terzaghi, K., Theoretical Soil Mechanics, John Wiley and Sons, Inc., New York, 1943, pp. 12.
 56. Thompson, L. J., "Overpressured Marine Sediments," Report for U.S.G.S. Grant No. T4-08-00T-G-444, U. S. Geological Survey, Texas A&M Research Foundation, College Station, Texas, July 1979.
 57. Timoshenko, S. P., and Goodier, J. N., Theory of Elasticity, 3rd ed., McGraw-Hill Book Company, New York, 1970.
 58. Torrey, P. D., "Progress in Squeeze Cementing Application and Technique," Oil Weekly, Vol. 98, No. 8, July 1940, pp. 68-84.
 59. Tschebotarioff, G. P., Soil Mechanics, Foundations, and Earth Structures, McGraw-Hill Book Company, Inc., New York, 1951.
 60. Wahi, J. S., et al., "The Dual Spacing Formation Density Log," Well Logging, 1971 ed., SPE Reprint Series No. 1, Society of Petroleum Engineers of AIME, Dallas, Texas, 1971, pp. 209-214.
 61. Westergaard, H. M., "Plastic State of Stress Around a Deep Well," Journal of the Boston Society of Civil Engineers, Vol. 27, No. 1, January 1940, pp. 387-391.

APPENDIX II

NOTATION

The following symbols are used in this thesis:

A = coefficient in Ch. IV dependent on boundary conditions

A_s = grain-to-grain contact area

A_t = total area of any surface through soil

A_w = area on which pore pressure acts

a = radius of borehole

B = coefficient in Ch. IV dependent on boundary conditions

b = radius of plastic zone surrounding the borehole

C_b = rock bulk compressibility

C_r = rock matrix compressibility

c = cohesion

D = coefficient in Ch. IV dependent on boundary conditions

F = total measured frictional force

h = sample height

K_σ = lateral earth-pressure coefficient at rest

$K_{\sigma_{nc}}$ = K_σ for normal consolidation used by Schmidt (48)

$K_{\sigma_{rb}}$ = K_σ for rebound used by Schmidt (48)

K_p = passive lateral earth pressure coefficient

k_f = matrix stress coefficient used by Mathews and Kelly (34)

LL = Liquid Limit

n = porosity

OCR = overconsolidation ratio

P_f = borehole pressure necessary to initiate a fracture

P_p = borehole pressure necessary to propagate a fracture

P_w = borehole pressure

PI = plasticity index

PL = plastic limit

PND = pressure nullification device

p = portion of borehole pressure transmitted to the soil matrix

p_f = limiting value of p associated with failure around a borehole

p_n = nullification pressure during experimentation

Q = applied overburden force

Q' = average overburden load throughout sample

r = radial coordinate from the vertical axis of the borehole

u = pore pressure

x = factor in Schmidts equation (48) depending on soil type

z = depth, vertical coordinate

β = coefficient in the Mohr-Coulomb failure criterion

β_1 and β_2 = compressibility factors used by Bjerrum, et al. (9)

γ_t = total unit weight of material

Δ = change, e.g., $\Delta\sigma$

ϵ_c = circumferential strain detected by electrical strain gage

θ = polar coordinate around borehole

λ = coefficient in the Mohr-Coulomb failure criterion

ν = Poisson's ratio

σ = total stress

$\bar{\sigma}$ = effective stress

σ' = matrix stress

σ_h = total horizontal stress

$\bar{\sigma}_h$ = effective horizontal stress

σ_h' = matrix horizontal stress

$\bar{\sigma}_{hf}$ = effective horizontal stress at failure

- σ_r = total radial stress
 $\bar{\sigma}_r$ = effective radial stress
 σ_r' = matrix radial stress
 σ_{re}' = matrix radial stress in the elastic zone
 σ_{rp}' = matrix radial stress in the plastic zone
 σ_s = stress acting across grain-to-grain contacts in a porous medium (intergranular stress)
 σ_t = tensile strength of the formation
 σ_v = total vertical stress (overburden stress)
 $\bar{\sigma}_v$ = effective vertical stress
 $\bar{\sigma}_{vf}$ = effective vertical stress at failure
 σ_θ = total tangential stress
 $\bar{\sigma}_\theta$ = effective tangential stress
 σ_θ' = matrix tangential stress
 $\sigma_{\theta e}'$ = matrix tangential stress in the elastic zone
 $\sigma_{\theta p}'$ = matrix tangential stress in the plastic zone
 σ_z' = matrix vertical stress
 σ_{11} = major total principal stress
 $\bar{\sigma}_{11}$ = major effective principal stress
 σ_{11}' = major matrix principal stress
 σ_{22} = intermediate total principal stress
 $\bar{\sigma}_{22}$ = intermediate effective principal stress
 σ_{22}' = intermediate matrix principal stress
 σ_{33} = minor total principal stress
 $\bar{\sigma}_{33}$ = minor effective principal stress
 σ_{33}' = minor matrix principal stress

τ_{re} = total shear stress

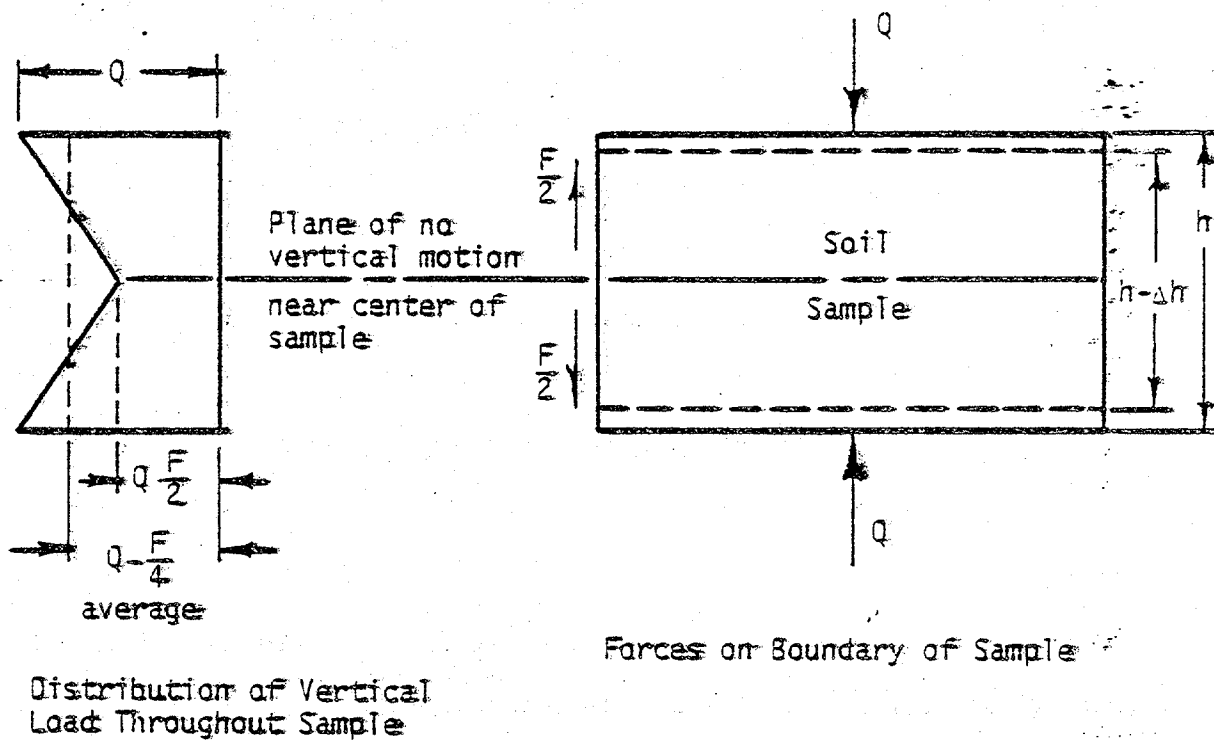
ϕ = angle of internal friction

APPENDIX III

CALCULATIONS CORRECTING FOR SIDEWALL FRICTION

In a floating ring consolidometer the sidewall frictional stresses act in opposite directions for the upper and lower halves. Akagi (2) showed that it is reasonable to assume that the magnitude of this frictional stress is constant throughout the height of the sample. Using this approach Figs. 38 and 39 illustrate a simplified idea of the effects of friction on a sample during consolidation and rebound respectively in a floating ring consolidometer.

Due to the frictional stresses along the sidewall the overburden load decreases linearly from both ends towards the center of the sample for consolidation. Similarly it increases for rebounding. It can be seen then that the average overburden load for consolidation is the applied overburden force less one-fourth of the measured frictional force, and for rebounding it is the applied overburden force plus one-fourth of the measured frictional force. By dividing these corrected overburden forces by the cross-sectional area of the sample, the overburden stress corrected for sidewall friction is obtained.



$$Q' = Q - \frac{F}{4}$$

where: Q' = Average overburden load throughout sample

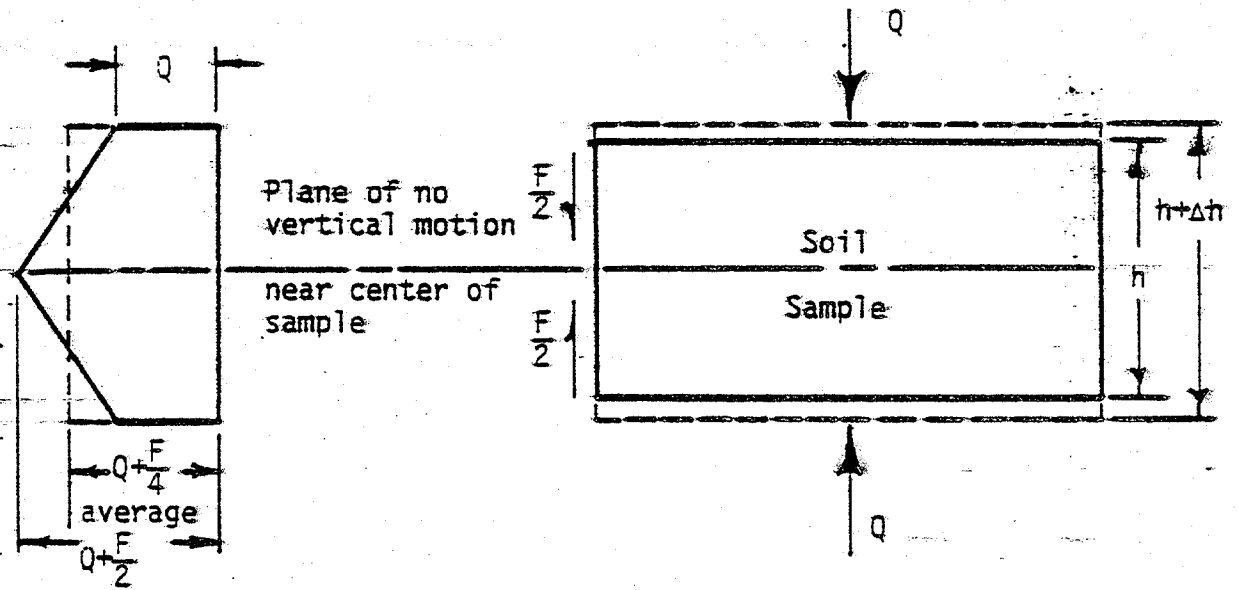
Q = Applied overburden force

F = Total measured frictional force

h = Overall sample height due to consolidation

Above assumes a constant frictional stress acts along the sides of the sample.

Fig. 38 - Approximation of Vertical Load Throughout a Consolidation Sample in a Floating Ring Consolidometer



Distribution of
Vertical Load
Throughout Sample

Forces on Boundary of Sample

$$Q' = q + \frac{F}{4}$$

where: Q' = Average overburden load throughout sample

F = Total measured frictional force

h = Overall sample height

Δh = Change in sample height due to rebound

Above assumes a constant frictional stress acts along the sides of the sample.

Fig. 39 - Approximation of Vertical Load Throughout a Rebounding Sample in a Floating Ring Consolidometer

APPENDIX IV

TABLES OF RESULTS FOR K_{α} MEASUREMENT TESTS

TABLE 7 - Experimental Results for Sample No. K-1

σ_v applied, psi	σ_v corrected for friction, psi	σ_h measured, psi	K_o	$\eta\%$
0	0	0		74.0
407	387	174	.45	47.4
1385	1325	608	.46	40.6
10183	10051	4808	.48	24.4
1385 *	1552	972	.63	28.9
407 *	449	261	.58	34.1

* unloading

TABLE 8 - Experimental Results for Sample No. K-2

σ_v applied, psi	σ_v corrected for friction, psi	σ_h measured, psi	K_o	n%
0	0	0		73.2
407	392	234	.60	46.5
1385	1298	742	.57	39.2
5295	5199	3070	.59	31.2
10183	10069	6279	.62	26.0
5295 *	5373	4006	.75	26.4
1385 *	1534	1468	.96	29.1
407 *	503	484	.96	33.1

* unloading

TABLE 9 - Experimental Results for Sample No. K-3

σ_v applied, psi	σ_v corrected for friction, psi	σ_h measured, psi	K_D	n%
0	0	0		74.2
36	35	21	.61	57.0
72	70	44	.63	54.6
143	139	96	.69	51.7
407	389	254	.65	47.1
733	710	486	.68	43.9
1385	1343	899	.67	40.4
2688	2628	1704	.65	36.3
5295	5253	3419	.66	32.4
2688 *	2802	2501	.89	32.4
1385 *	1481	1635	1.10	33.7
733 *	775	945	1.22	35.4
407 *	471	561	1.19	37.1
143 *	158	127	.80	40.0
72 *	80	61	.77	41.5
143 **	134	70	.52	41.5
407 **	380	222	.58	39.7
733 **	681	544	.80	38.3
1385 ***	1307	948	.73	36.4
2688 **	2592	1705	.66	34.1
5295 **	5146	3310	.64	31.5

TABLE 9 (Continued)

σ_v applied, psi	σ_v corrected for friction, psi	σ_h measured, psi	K_0	n%
10183 **	9998	6321	.63	27.1
5295 *	5444	4541	.83	27.1
2688 *	2784	2979	1.07	28.2
1385 *	1481	1771	1.20	29.8
733 *	811	990	1.22	31.5
407 *	485	534	1.08	33.4
143 *	176	185	1.05	36.3
407 ***	365	292	.80	35.8
733 ***	669	479	.72	34.5
1385 ***	1271	860	.68	33.0
2688 ***	2539	1635	.64	31.2
5295 ***	5074	3160	.62	29.2
2688 *	2873	2403	.84	29.2
1385 *	1499	1489	.99	30.3
733 *	865	892	1.03	31.9
407 *	485	530	1.09	33.5

* unloading

*** reloading

TABLE 10 - Experimental Results for Sample No. K-4

σ_v applied, psi	σ_v corrected for friction, psi	σ_h measured, psi	K_0	$n\%$
0	0	0		75.1
72	69	28	.39	55.0
407	393	247	.63	47.2
1385	1303	868	.67	40.5
2688	2556	1667	.65	36.1
5295	5199	3240	.62	32.4
10183	9944	6412	.64	27.3
5295 *	5516	4906	.89	27.3
2688 *	2802	3034	1.08	28.3
1385 *	1499	1863	1.24	30.1
733 *	882	1079	1.22	31.9
407 *	503	637	1.27	33.6

* unloading

TABLE II - Experimental Results for Sample No. K-5

σ_v applied, psi	σ_v corrected for friction, psi	σ_h measured, psi	K_0	n%
0	0	0		74.5
407	383	253	.66	47.9
1385	1325	886	.67	41.3
5295	5181	3472	.67	33.1
10183	10069	6454	.64	28.3
5295 *	5462	4716	.86	28.7
1385 *	1517	1775	1.17	31.7
407 *	503	687	1.37	35.4

* unloading

TABLE 12 - Experimental Results for Sample No. KS-1

σ_v applied psi	σ_v corrected for friction, psi	σ_h measured, psi	K_0	$\pi\%$
0	0	0		57.5
407	378	240	.63	40.0
1385	1339	933	.70	33.0
2688	2610	1717	.66	29.5
5295	5217	3070	.59	25.6
10183	10087	6145	.61	20.9
5295 *	5427	4006	.74	21.0
2688 *	2837	2937	1.04	21.8
1385 *	1570	2134	1.36	22.9
407 *	556	696	1.25	26.0

* unloading

TABLE 13 - Experimental Results for Sample No. KS-2

σ_v applied, psi	σ_v corrected for friction, psi	σ_h measured, psi	K_o	n%
0	0	0		62.5
407	378	239	.63	34.7
1385	1307	848	.65	29.9
5295	5199	2937	.56	24.0
10183	10051	5727	.57	20.6
5295 *	5427	4123	.76	20.6
1385 *	1552	1940	1.25	22.0
407 *	539	894	1.66	23.7

* unloading

TABLE 14 - Experimental Results for Sample No. KS-3

σ_v applied, psi	σ_v corrected for friction, psi	σ_h measured, psi	K_o	$\pi\%$
0	0	0		49.5
407	374	184	.49	27.4
1385	1325	720	.54	24.1
2688	2556	1467	.57	21.4
5295	5128	2521	.49	18.1
10183	9998	5035	.51	14.8
5295 *	5480	3699	.68	14.9
2688 *	2855	2362	.83	15.3
1385 *	1552	1575	1.01	15.8
407 *	539	887	1.65	16.6

* unloading

TABLE 15 - Experimental Results for Sample No. KS-4

σ_v applied, psi	σ_v corrected for friction, psi	σ_h measured, psi	K_o	n%
0	0	0		49.9
407	370	158	.42	28.5
1385	1307	675	.52	24.8
2688	2592	1351	.52	22.0
5295	5181	2669	.52	18.8
10183	10034	4838	.48	15.5
5295 **	5480	3100	.57	15.8
2688 **	2873	2030	.71	16.3
1385 **	1552	1496	.96	16.6
407 **	574	835	1.45	17.3

** unloading

TABLE 16 - Experimental Results for Sample No. S-1

σ_v applied, psi	σ_v corrected for friction, psi	σ_h measured, psi	K_0	n%
0	0	0		38.2
407	383	202	.53	35.4
1385	1343	700	.52	34.4
2688	2610	1471	.56	33.2
5295	5163	2999	.58	30.5
10183	10034	5209	.52	25.9
5295 *	5480	4006	.73	26.0
2688 *	2826	2669	.94	26.3
1385 *	1523	1733	1.14	26.6
407 *	510	1142	2.24	27.2

* unloading

TABLE 17 - Experimental Results for Sample No. S-2

σ_v applied, psi	σ_v corrected for friction, psi	σ_H measured, psi	K_0	n%
0	0	0		38.6
407	392	192	.49	35.8
1385	1307	729	.56	34.1
2688	2592	1466	.57	32.4
5295	5146	2888	.56	29.3
10183	9998	5153	.52	24.2
5295 *	5498	3816	.69	24.4
2688 *	2873	2613	.91	24.8
1385 *	1534	1811	1.18	25.2
407 *	521	1009	1.94	25.9

* unloading

TABLE 18 - Experimental Results for Sample No. I

σ_v applied, psi	σ_v corrected for friction, psi	σ_{th} measured, psi	K_0	m%
0	0	0		64.0
36	33	28	.84	51.0
72	69	45	.65	47.5
143	138	90	.65	44.7
407	399	235	.59	40.7
733	720	420	.58	38.0
1385	1367	821	.60	35.6
2688	2556	1517	.59	32.7
5295	5038	2866	.57	30.5
2688 *	2909	2331	.80	30.5
1385 *	1606	1571	.98	31.5
733 *	865	1010	1.17	32.6
407 *	485	611	1.26	33.8
143 *	163	312	1.92	35.8
407 **	374	449	1.20	35.1
733 **	691	577	.83	34.1
1385 **	1325	914	.69	32.9
2688 **	2574	1592	.62	31.6
5295 **	5074	2979	.59	30.2
10183 **	9890	5395	.55	27.9
5295 *	5480	4244	.77	27.9

TABLE 18 (continued)

σ_v applied, psi	σ_v corrected for friction, psi	σ_h measured, psi	K_0	n%
2688 *	2837	3219	1.13	28.8
1385 *	1534	1931	1.26	29.8
733 *	900	1214	1.35	31.2
407 *	503	761	1.51	32.2
143 *	185	379	2.05	33.6

* unloading

** reloading

TABLE 19 - Experimental Results for Sample No. B

σ_v applied, psi	σ_v corrected for friction, psi	σ_h measured, psi	K_0	n%
0	0	0		82.2
407	383	286	.75	54.4
1385	1325	1047	.79	47.5
5295	5199	3472	.67	40.4
1385 *	1463	1322	.90	42.2
733 *	793	672	.85	43.5
407 *	467	457	.98	45.5
1385 **	1352	1148	.85	44.9
2688 **	2610	1942	.74	42.6
5295 **	5146	3605	.70	40.5
10183 **	10034	7257	.72	37.7
5295 *	5444	4851	.89	37.9
2688 *	2784	2846	1.02	39.7
1385 *	1463	1583	1.08	41.6
407 *	467	584	1.25	45.0

* unloading

** reloading

TABLE 20 - Experimental Results for Sample No. OS-1

σ_v applied, psi	σ_v corrected for friction, psi	σ_h measured, psi	K_0	n%
0	0	0		40.3
407	347	170	.49	36.5
733	655	313	.48	35.7
1385	1307	603	.46	35.4
2688	2628	1260	.48	34.4
5295	5235	2612	.50	31.8
2688 *	2766	1853	.67	31.9
1385 *	1481	1336	.90	31.9
733 *	811	939	1.16	32.0
407 *	503	665	1.32	32.4
733 **	566	588	1.04	32.2
1385 **	1182	819	.69	32.0
2688 **	2485	1257	.51	31.7
5295 **	5056	2422	.48	31.0
10183 **	9908	5053	.51	24.5
5295 *	5552	3260	.59	24.5
2688 *	2909	2331	.80	24.7
1385 *	1606	1705	1.06	25.1
733 *	954	1122	1.18	25.3
407 *	610	840	1.38	25.6

* unloading
** reloading

TABLE 21 - Experimental Results for Sample No. OS-2

σ_v applied, psi	σ_v corrected for friction, psi	σ_h measured, psi	K_0	n%
0	0	0		39.6
36	29	20	.70	39.3
72	60	40	.67	39.2
143	123	78	.63	39.0
407	356	207	.58	38.7
733	646	418	.65	38.5
1385	1289	725	.56	38.1
2688	2467	1456	.59	37.7
5295	5146	3115	.61	36.1
2688 *	2802	2531	.90	36.1
1385 *	1499	1746	1.16	36.3
733 **	823	1197	1.45	36.5
407 *	503	762	1.51	36.7
143 *	203	345	1.70	36.9
407 **	329	453	1.38	36.8
733 **	637	605	.95	36.6
1385 **	1236	960	.78	36.4
2688 **	2502	1536	.61	36.1
5295 **	5074	2847	.56	35.5
10183 **	9890	5879	.59	31.3
5295 *	5534	4409	.80	31.4

TABLE 21 (continued)

σ_v applied, psi	σ_v corrected for friction, psi	σ_H measured, psi	K_0	n%
2688 *	2909	3269	1.12	31.6
1385 *	1570	2312	1.47	31.9
733 *	900	1713	1.90	32.2
407 *	556	1224	2.20	32.4
143 *	292	786	2.69	32.4

* unloading

** reloading

TABLE 22 - Experimental Results for Sample No. OS-3

σ_v applied, psi	σ_v corrected for friction, psi	σ_h measured, psi	K_0	$n\%$
0	0	0		39.2
407	356	182	.51	38.5
1385	1289	645	.50	38.1
2688	2539	1274	.50	37.6
5295	5110	2584	.51	36.6
10183	9926	5744	.58	34.5

TABLE 23 - Experimental Results for Sample No. MC-I-U

σ_v applied, psi	σ_v corrected for friction, psi	σ_h measured, psi	K_0	n%
0	0	0		51.4
407	370	203	.55	42.7
1385	1307	842	.64	37.1
2688	2248	1325	.59	33.8
5295	5181	2803	.54	28.8
10183	10016	5427	.54	23.8
5295 *	5498	4090	.74	23.8
2688 *	2873	3020	1.05	24.4
1385 *	1570	2084	1.33	25.4
407 *	556	1025	1.84	27.3

* unloading

TABLE 24 - Experimental Results for Sample No. MC-I-R

σ_v applied, psi	σ_v corrected for friction, psi	σ_h measured, psi	K_0	$n\%$
0	0	0		71.9
407	365	201	.55	42.7
1385	1289	656	.51	35.7
2688	2592	1438	.55	31.6
5295	5128	2803	.55	27.8
10183	9980	5433	.54	23.5
5295 *	5498	3962	.72	23.6
2688 *	2855	2759	.97	24.2
1385 *	1534	2224	1.45	25.2
407 *	539	1129	2.09	27.9

* unloading

TABLE 25 - Experimental Results for Sample No. MC-II-U

σ_v applied, psi	σ_v corrected for friction, psi	σ_h measured, psi	K_0	n%
0	0	0		74.2
407	365	107	.29	67.6
1385	1307	620	.47	55.0
2688	2592	1264	.49	48.5
5295	5163	2440	.47	42.0
10183	9998	4942	.49	35.6

APPENDIX V

RESULTS FROM TOTAL HORIZONTAL STRESS MEASUREMENTS
WITH PORE PRESSURES INDUCED

TABLE 26 - Horizontal Stress Measurements with Pore Pressures Induced for Sample No. OS-3

σ_v Applied, psi	n , %	u Induced, psi	σ_h Measured, psi	A_w	Correlation Coefficient
407	38.5	0	182	0.713	0.98751
		45	199		
		90	242		
		134	273		
		179	304		
1385	38.1	0	645	0.723	0.99928
		90	701		
		179	770		
		269	840		
		359	900		
2688	37.6	0	1274	0.723	0.99893
		179	1385		
		359	1525		
		538	1657		
		717	1786		
5295	36.6	0	2584	0.784	0.99974
		179	2718		
		359	2861		
		538	3003		
		717	3137		
		896	3288		

TABLE 26 - (Continued)

σ_v Applied, psi	n, %	μ Induced, psi	σ_h Measured, psi	A_w	Correlation Coefficient
10,183	34.5	0	5744	0.749	0.99917
		179	5875		
		359	6011		
		538	6145		
		717	6306		
		896	6412		
		1075	6546		
		1255	6680		

TABLE 27 - Horizontal Stress Measurements with Pore Pressures Induced for Sample No. MC-II-U

σ_v Applied, psi	n , %	u Induced, psi	σ_h Measured, psi	A_w	Correlation Coefficient
407	67.6	0	107	0.591	0.96233
		90	136		
		134	171		
		179	203		
		224	238		
1385	55.0	0	620	0.644	0.99995
		179	734		
		359	851		
		538	964		
		717	1083		
2688	48.5	0	1264	0.728	0.99963
		359	1509		
		717	1760		
		1075	2029		
		1434	2299		
		1792	2562		

TABLE 27 - (Continued)

σ_v Applied, psi	n , %	u Induced, psi	σ_h Measured, psi	A_w	Correlation Coefficient
5295	42.0	0	2440	0.740	0.99821
		359	2659		
		717	2921		
		1075	3240		
		1434	3538		
		1792	3787		
		2151	4024		
		2509	4273		
2878	4520				
10,183	35.6	0	4942	0.716	0.99947
		359	5206		
		717	5473		
		1075	5704		
		1434	5960		
		1792	6239		

VITA

Michael Joseph Callanan, son of Mr. and Mrs. M. J. Callanan, was born on December 3, 1956 in Houston, Texas. Upon graduation from Ross Sterling High School in Houston, he entered Texas A&M University in September 1975 where he earned a Bachelor of Science degree in Civil Engineering in August 1978. Strong interests in the Geotechnical Engineering field kept him at Texas A&M University to pursue an advanced degree.

Mr. Callanan's permanent address is 7136 Evans, Houston, Texas, 77061.

The typist for this thesis was Mrs. Joy Taylor.